Applications of Melt Inclusions to Problems in Igneous Petrogenesis

Matthew J. Severs

Dissertation submitted to the faculty of the Virginia Polytechnic Institute and State University in partial fulfillment of the requirements for the degree of

DOCTOR OF PHILOSOPHY
in
GEOSCIENCES

Committee:
Robert J. Bodnar
James Beard
J. Donald Rimstidt
James A. Spotila
Robert J. Tracy

June 22, 2007
Blacksburg, Virginia

Keywords: Melt Inclusion, Raman Spectroscopy, Volatiles, LA-ICP-MS, Partition Coefficient, Trace Element, Campi Flegrei

Applications of Melt Inclusions to Problems in Igneous Petrogenesis

by

Matthew J. Severs

ABSTRACT

Understanding the different igneous processes that magmas undergo is important for a variety of reasons including potential hazards associated with volcanoes in populated regions, magmatic hydrothermal ore deposition, and tectonic processes. One method of obtaining geochemical data that can help constrain petrogenetic processes is through the study of melt and fluid inclusions. The research presented here examines melt inclusions through experimental, analytical and field studies to better understand igneous petrogenesis.

One potential problem associated with melt inclusions is water-loss during laboratory heating. A Raman spectroscopic technique was developed to determine water contents of silicate glasses, and this technique was applied to monitor water loss from natural melt inclusions that were heated for varying lengths of time. The results suggest that water loss is insignificant when heated for less than 12 hours but significant water loss can occur with longer duration heating.

The distribution of trace elements between silicate melts and phenocrysts growing from that melt can constrain igneous processes such as fractional crystallization, assimilation, and partial melting. Partition coefficients were determined for syngenetic clinopyroxene, orthopyroxene, and plagioclase in equilibrium with a dacitic melt using the Melt Inclusion-Mineral (MIM) technique. Melt inclusion chemistry is the same regardless of mineral host phase, suggesting that the melt inclusions have not been subjected to re-equilibration processes or boundary layer development. Partition coefficients from this study are similar but typically lower than published values.

Three closely-spaced monogenetic eruptive units from the active Campi Flegrei volcanic system (Italy) with similar eruptive styles were examined to better understand the evolution of the magmatic system. Results suggest fractional crystallization as the dominant process taking place over time but that magma mixing was significant for one of the eruptions. Trace element geochemical data suggest a mixed magma source of within-plate and volcanic arc components, and still retain a T-MORB signature from the subducting slab.

Acknowledgements

First, I would like to thank my advisor, Bob Bodnar, for his incredible teaching of geology and geochemistry, for giving me such good advice about all aspects of academic life, and for suggesting the projects that I have undertaken. I would like to thank my wife, Wendy Hope Hirschelman Severs for being there for me every day, good or bad, for the past few years to cheer me up and motivate me to accomplish my goals. Our Siberian Huskies, Una and Mikah, have also helped keep me light-hearted with their wonderful and mischievous behavior. My parents, Alan and Angie Severs, and my sister, Erin Severs, helped encourage me through all of my activities, both educational and non-educational, and for their love for me. I would also like to thank my parents-in-law, Mike and Lynne Hirschelman for their understanding and love. Over the course of the past five years I have made many friends in Blacksburg, many of whom were in the Department of Geosciences as well, and they have been there for me if I wanted to talk about research or teaching, or if I just wanted someone to go for a run, play soccer or basketball. The Fluids Research Group, both past and present, are such as wonderful group of colleagues who help make all aspects of teaching and research more entertaining. I would like to thank all of the staff, both administrative and technical, for helping with all of the paperwork involved in graduate school and for making sure that all of our instruments were working smoothly. I would also like to thank my undergraduate professors at Colby College for opening my eyes to the wonders of geology. Many thanks go to my committee of Bob Bodnar, Bob Tracy, Don Rimstidt, Jim Spotila, and Jim Beard for stimulating my thought processes about research and teaching and providing me with the opportunity to make my own educational path. This will serve me well as I move on to the next phase in my career as a Visiting Assistant Professor at the College of Wooster.

For the research projects, I would like to thank Charlie Mandeville for providing the glass samples used to calibrate the Raman microprobe, Beth Glusica for assistance conducting some of the analyses, and especially Jay Thomas for discussions about the project and providing the Bishop Tuff samples. I would like to thank Clayton Loehn for assistance conducting electron microprobe analyses and Scott Mutchler for help carrying out laser ablation analyses. Many thanks go to Paola Frattini for showing me the Procida volcanic area and helping me conduct the fieldwork, Annamaria Lima for assistance in the field and in the laboratory, and especially Benedetto De Vivo for giving me the opportunity to come to Italy to be a part of his ongoing project on Italian volcanism.

Table of Contents

List of Tables

List of Figures

Chapter 1: Introduction

A detailed knowledge of the geochemistry of igneous rocks is necessary to understand the processes that affected the magma from its infancy to its end-product as a crystallized body of volcanic or plutonic material. The ability to recognize fractional crystallization, magma mixing, assimilation, or other processes provides significant information concerning the evolution of the magma chamber from which they were erupted. This need for information applies to active and potentially hazardous volcanoes in populated areas or for volcanic systems associated with ore deposition, both of which frequently involved volatile-rich magmas. One way to indirectly monitor the conditions and processes that operated in a magma chamber is through the study of melt inclusions. Melt inclusions trap small amounts of the unaltered and non-degassed silicate melt from which phenocrysts grow. Analyses of melt inclusions can provide important geochemical information on the melt and help to better understand igneous petrogenesis.

Chapter 2 addresses a much debated question in melt inclusion research related to whether or not melt inclusions lose water during laboratory heating. In order to measure the water content of individual melt inclusions, melt inclusions were analyzed using UV Raman spectroscopy. The results indicate that heating melt inclusions for 12 hours or less does not induce measureable water loss. This work was a collaborative effort involving several researchers. Tristan Azbej assisted in the collection of Raman analyses and with sample preparation. Charlie Mandeville provided the glass standards used for Raman calibration, and Jay Thomas initiated the analysis of melt inclusions using Raman spectroscopy and provided the Bishop Tuff samples. Results of this study were published in *Chemical Geology* in March, 2007.

Chapter 3 describes the behavior of trace elements in dacitic magmas and the use of the Melt Inclusion-Mineral (MIM) technique to measure partition coefficients between clinopyroxene, orthopyroxene, plagioclase, and silicate melt. Partition coefficients calculated in this study are similar to the published literature values except the partition coefficients from this study are typically lower than those in the literature.

Chapter 4 describes a field based study in the active Campi Flegrei volcanic system, Naples, Italy. This study is part of an ongoing project conducted by Benedetto De

Vivo, Annamaria Lima, and Robert Bodnar. This study examined the volcanic rocks at Procida Island to constrain the petrogenesis of different monogenetic eruptive units. Evidence from the melt inclusion compositions suggest that fractional crystallization of olivine, clinopyroxene, and sanidine is the dominant process for these magmas, but that for one of the eruptions there is evidence of magma mixing as well.

Chapter 2: Experimental Determination of H_2O Loss from Melt Inclusions During Laboratory Heating: Evidence from Raman Spectroscopy

Matthew J. Severs, Tristan Azbej, and Robert J. Bodnar
Fluids Research Laboratory, Department of Geosciences, Virginia Polytechnic Institute and State University, Blacksburg VA 24061, USA

Jay B. Thomas
Department of Earth and Environmental Sciences, Renssalaer Polytechnic Institute, Troy NY 12180, USA

Charles W. Mandeville
Department of Earth and Planetary Sciences, American Museum of Natural History, New York NY 10024, USA

Published March 5, 2007 in *Chemical Geology* v. 237, 358-371.

Abstract

Experiments have been conducted to quantify H_2O loss from melt inclusions during laboratory heating using Raman spectroscopy. Quartz-hosted melt inclusions from the early-erupted plinian stage of the Bishop Tuff were heated to 800°C and 1 kbar for 4 to 1512 hours (63 days). Previous studies had shown that unheated melt inclusions from this unit of the Bishop Tuff contain 4.8-6.5 wt % H_2O. Many Bishop Tuff melt inclusions fluoresce under visible (514 nm) Raman excitation. To minimize fluorescence interference, a method was developed to analyses silicate glasses and melt inclusions using an UV (244 nm) excitation source. The Raman microprobe was calibrated using silicate glass standards with known H_2O contents, and the results indicate that the UV excitation data produce a calibration line with a different slope compared to that produced using visible excitation. The inclusions show insignificant H_2O loss when heated for less than 12 hours, while approximately 75% of the original H_2O was lost after 1512 hours. The rate of H_2O loss decreases after a few hundred hours, suggesting either a change in H_2O speciation or in the mechanism of H_2O loss. Our results suggest that most silicic melt inclusions maintain their original H_2O concentration if they are not heated for more than about 12 hours during laboratory studies.

Keywords: Melt inclusions, UV Raman, water, microthermometry, Bishop Tuff

1. Introduction

Volatile components play an important role in eruptive behavior of volcanic systems (Sparks et al., 1994) and formation of magmatic-hydrothermal ore deposits (Burnham, 1979; 1997; Bodnar, 1995). Water is usually the most abundant volatile in silicic magmas (McMillan, 1994), and influences the location of the liquidus and solidus as well as the viscosity and density of the melt (Lange, 1994). As such, a complete understanding of the evolution of a magmatic system requires information on the H_2O content of the melt during crystallization. Melt inclusions provide the best samples for determining pre-eruptive volatile contents in silicate melts (i.e., Lowenstern, 1995; Student and Bodnar, 1996; 2004).

The use of melt inclusions to study magmatic processes is based on the assumption that the inclusions represent the melt present at the time of trapping, and that nothing has been added to or lost from the inclusion since trapping (Roedder, 1984: Bodnar, 2003a; Bodnar & Student, 2006). However, several authors have suggested that H_2O may diffuse out of melt inclusions if the sample is maintained at elevated temperatures for extended periods of time during homogenization experiments in the lab (Qin et al., 1992; Massare et al., 1998; Massare et al., 2002), similar to observations associated with aqueous inclusions (Vityk et al., 2000; Bodnar, 2003b). Other workers have documented the reequilibration of melt inclusions in olivine by loss of iron during prolonged heating in the laboratory (Danyushevsky et al., 2000). In this study, the loss of H_2O from melt inclusions during laboratory heating was investigated using quartz-hosted melt inclusions from the early-erupted plinian phase of the Bishop Tuff. Inclusions with "known" H_2O contents were maintained at 800°C and 1 kbar for varying lengths of time, and the H_2O content of the inclusions after heating was determined by Raman spectroscopy. To minimize analytical problems associated with fluorescence, the inclusions were analyzed using UV excitation (244 nm), and the results were compared to analyses using visible (514 nm) excitation.

2. Raman spectra of hydrous glass

Raman spectroscopy has recently been applied to determine H_2O contents of glasses and melt inclusions (Thomas, 2000; Thomas et al., 2002; Chabiron et al., 2004; Zajacz et al., 2005; Thomas et al., 2006; Di Muro et al., 2006). Raman spectroscopy is non-destructive, requires minimal sample preparation, and can be used to analyze both exposed and unexposed inclusions as small as 5 μm. The intensity of the Raman peak is directly proportional to H_2O concentration and is independent of the composition of the glass (Thomas, 2000). The Raman spectrum of silicate glass shows two major bands in the low-wavenumber region, at approximately 490 cm^{-1} and 1050 cm^{-1} when analyzed with visible (488 nm or 514 nm) excitation (Fig. 1A). The broad band at 490 cm^{-1} is attributed to symmetric stretching of the oxygen bond in the tetrahedra-oxygen-tedrahedra (T-O-T) structure (Matson et al., 1983; Sharma et al., 1997). In completely polymerized alkali-feldspar melts (i.e., containing no non-bridging oxygens) the broad band at 1050 cm^{-1} represents an asymmetric stretching vibration in the T-O-T links that produces a doublet with distinct bands at 1020 cm^{-1} and 1105 cm^{-1} (McMillan et al., 1982; McMillan et al., 1992; Mysen, 1997; Sharma et al., 1997; Mysen, 1999). A decrease in the degree of polymerization, or the addition of Fe, results in the appearance of new Raman bands which represent stretching modes between the different structural species present (McMillan et al., 1982; Wang et al., 1993; Mysen, 1997; 1999; Sharma et al., 1997). The 586 cm^{-1} band is attributed to defects (Seifert et al., 1981; McMillan and Wolf, 1995) while the 776 cm^{-1} band has been assigned to T-O-T bending vibrations (Chabiron et al., 2004).

Thomas (2000), Thomas et al. (2002) and Chabiron et al. (2004) derived linear correlations between the total H_2O content of feldspar glasses and the ratio relating the integrated sum of the H_2O-OH band at around 3550 cm^{-1} and the integral area of the asymmetric T-O band at about 490 cm^{-1}. Integrated ratios are used rather than peak intensities because this method eliminates short time fluctuations and the need for multiple calibrations due to long-term instability of the laser (Thomas, 2000). Thomas (2002a) expanded the compositional range to include basaltic, andesitic, and phonolitic compositions. Zajacz et al. (2005) used a slightly different method and related the H_2O

content to the ratio of the 3550 cm^{-1} peak area and the area under the broad T-O and T-O-T vibrational bands between 850 cm^{-1} and 1250 cm^{-1}.

All of the above mentioned studies used a visible wavelength laser (either 514 nm or 488 nm) as the excitation source. While these are the most commonly available laser sources for Raman analysis, visible excitation wavelengths limit the applicability of the Raman technique to determine H_2O contents of glasses and melt inclusions because many samples fluoresce when excited at these wavelengths (Fig. 2). Some samples only fluoresce after heating in the laboratory (R. Thomas, pers. comm.) while others such as the Macusani glass fluoresce naturally. Fluorescence following heating is thought to be the result of changes in the oxidation state of trace elements present in the melt (Thomas, 2000). The fluorescence intensity generally increases with increasing distance from the Rayleigh line (i.e., at higher wavenumbers) and precludes an accurate determination of peak areas, especially the H_2O peak located near 3550 cm^{-1}. The fluorescence is likely caused by trace elements in the glass or by defects in the crystal lattice (Chabiron et al., 2004). To minimize fluorescence interference in the present study, the relationship between H_2O content and Raman signal was determined using a 224 nm (ultraviolet) laser. This new calibration relationship was then used to monitor H_2O loss from melt inclusions during laboratory heating.

Spectra generated with UV excitation are similar to those obtained with visible (green) excitation, with a few significant exceptions (Fig. 1B). The 490 cm^{-1} band becomes broader and less distinct, compared to the sharp, narrow band produced using visible excitation wavelengths. The broadening suggests that UV excitation results in stronger T-O-T bending signals at 586 cm^{-1} and 776 cm^{-1} that interfere with the 490 cm^{-1} signal. Similar differences between UV-excitation spectra and those generated by visible wavelength lasers have been noted for biological samples (Smith and Dent, 2005).

3. Calibration of the Raman spectra

3.1 Calibration standards and instrumentation

Many unheated melt inclusions in the Bishop Tuff fluoresce under visible wavelength excitation (Fig. 2). As such, the first step in this study to examine H_2O loss from the melt inclusions during laboratory heating was to calibrate the Raman microprobe using UV (244 nm) excitation to minimize fluorescence interference.

Synthetic glasses containing between 0.95 and 9.5 wt% H_2O were used for the calibration. Twelve of the standards have compositions in the $(Na,K)AlSi_3O_8$ system and were prepared to determine the solubility of H_2O in alkali feldspar melts at 900°C and 5 kbars (Voigt et al., 1981). Four additional samples with andesitic composition were also used (Mandeville et al., 2002). The H_2O contents of these latter samples were confirmed through Karl-Fisher titration and FTIR analysis.

Raman spectra were collected on a JY Horiba Labram HR800UV confocal Raman microprobe equipped with a 2400 groove/mm grating, and an Olympus optical microscope and a 40X UV-specific objective. Raman scattering is detected with a Symphony liquid-nitrogen cooled CCD detector. A Lexel-85 244 nm UV laser excited the sample. Acquisition times of 60 seconds were used for glass standards containing >2 wt% H_2O, and acquisition time was increased to 180 seconds for samples containing less than 2 wt% to improve the signal-to-background ratios. Three accumulations were obtained for each analysis to identify and eliminate cosmic spikes. The lower wavenumber region (≈ 200 - 1750 cm^{-1}) was analyzed first, followed by the higher wavenumber region (≈ 1750 - 3900 cm^{-1}). The maximum intensity was obtained when the laser was focused approximately 10 μm below the surface of the sample. The confocal hole was set at 400 μm for the glass standard analysis.

For comparison, the standards were also analyzed using a JY Horiba Labram HR800 confocal Raman microprobe equipped with a 514.57 nm Laserphysics Reliant laser, an Olympus microscope with a 50X objective, and an Andor electronically cooled CCD detector. Acquisition times and number of accumulations were the same as for the ultraviolet excitation reported above.

3.2 Spectral treatment

Raman spectra obtained using visible and UV excitation were treated in three steps using Labspec and Origin 7.5 software, as suggested by Zajacz et al. (2005). The first step involved baseline removal, followed by a frequency-temperature correction and, finally, band integration (Fig. 4). Linear baseline corrections were applied to the 3550 cm^{-1} band and the broad 1050 cm^{-1} band. The 3550 cm^{-1} baseline extended from approximately 3900 to 1250 cm^{-1}, and the 1050 cm^{-1} baseline extended from approximately 1250 to 850 cm^{-1} (Fig. 3A). A third baseline correction was applied from 850 cm^{-1} to the lowest wavenumbers recorded (≈ 200 cm^{-1}). The high shoulder that appears on the 490 cm^{-1} band obtained with the visible excitation (Fig. 1A) and the less-well defined 490 cm^{-1} band obtained with the UV excitation result in a less precise baseline correction at lower wavenumbers compared to higher wavenumbers.

After the baseline correction to eliminate background noise, a frequency-temperature intensity correction was applied (McMillan and Wolf, 1995; Keresztury, 2002; Long, 2002; Zajacz et al., 2005), as given by the equation:

$$I_{corr}^{Stokes} = I_{obs}^{Stokes} \frac{\nu(1-e^{\frac{-h\nu}{kT}})}{\nu^* - \nu^4}$$

where ν* is the frequency of the incident laser light [either 7.31512 x 1019 Hz (244 nm) or 1.54097 x 1020 Hz (514 nm)], ν is the frequency of the Raman-scattered light, *h* is Planck's constant, *k* is the Boltzmann constant, and T is the temperature of the analysis in Kelvin. The correction accounts for the decreasing efficiency of Raman scattering with higher wavenumbers and eliminates the shoulder on the 490 cm^{-1} peak. This correction produces spectra that are less compositionally dependent (Zajacz et al., 2005). A separate frequency-temperature intensity correction was required for the visible and UV spectra because the magnitude of the correction is excitation wavelength-dependent.

Following the baseline and frequency-temperature corrections, the areas under the 1050 cm^{-1} and at 3550 cm^{-1} peaks were determined. The first peak was integrated from 835 to 1225 cm^{-1}, and the second peak was integrated from 2850 to 3750 cm^{-1} (Fig 3C). The peak area ratio was determined by dividing the total H_2O peak area at 3550 cm^{-1} by the T-O-T 1050 cm^{-1} peak area. Some caution must be used when using the T-O-T 1050 cm^{-1} peak area because this band can contain important hydroxyl components, such as B-

OH, Al-OH, and Si-OH (Holtz et al., 1996; Thomas, 2002b). However, for simple compositions (such as the Bishop Tuff melt inclusions; Dunbar and Hervig, 1992; Anderson et al, 2000) and low total H_2O concentrations, ignoring these contributions introduces minimal errors. The T-O 490 cm^{-1} peak was not used for the UV calibration because the goal was to compare the calibration results for visible and UV, and the 490 cm^{-1} peak becomes broader and less distinct and more difficult to quantify when UV excitation is used. For each set of calibration data, the 3550 cm^{-1}/1050 cm^{-1} peak area ratio was related to the H_2O content (Fig. 4).

Analytical precision was tested by conducting repeated analyses of the same spot on the glass standard containing 4.93 wt% H_2O. The same spot (±10 μm) was also analyzed daily for 3 days to examine variations over time. The calculated standard deviation is ±0.1 wt% H_2O using visible excitation, and ±0.2 wt% H_2O with UV excitation. The slightly higher standard deviation using UV excitation is due to the slightly higher overall background in the UV spectra compared to those obtained with 514 nm excitation.

The calibration results for both the UV and visible excitation are shown in Figure 4. The analytical data were fit to straight lines, with both lines constrained to pass through the origin because spectra of a sample with no H_2O do not show a 3550 cm^{-1} peak. The two calibration lines show different slopes as is expected owing to differences in the UV and visible spectra shown in Figures 1A and 1B. The results confirm the observations of Thomas (2000), Thomas et al. (2002), Chabiron et al. (2004), and Zajacz et al. (2005) that indicate a systematic relationship between H_2O contents of silicate glasses and Raman intensities. However, the specific relationship between H_2O content and Raman intensity varies from one instrument to the next, as has been shown previously by Pasteris et al. (1988) for aqueous inclusions. The UV calibration results show more scatter compared to those obtained with the visible laser, owing to the slightly higher background for the UV spectra. This higher background is believed to be instrument derived and not a result of fluorescence from to the inclusions. Most of the fluorescence interference associated with visible excitation wavelengths is eliminated in the UV spectra (Fig. 2).

4. Water loss from melt inclusions

4.1 Experimental and analytical techniques

In order to monitor H_2O loss from melt inclusions during laboratory heating, melt inclusions with a known initial H_2O content are required. One potential source is synthetic melt inclusions. Student and Bodnar (1999) trapped synthetic melt inclusions containing 5.5 wt% H_2O, but the inclusions were small, tabular (rather than equant like most natural melt inclusions) and difficult to synthesize. Additionally, the quartz host surrounding the synthetic inclusions contains a high density of dislocations, allowing H_2O to move more easily into (or out of) the inclusions compared to natural samples (Vityk et al, 2000).

In this study, natural melt inclusions from the Bishop Tuff in California, USA, were selected to monitor H_2O loss from inclusions during laboratory heating. The early-erupted plinian phase of the Bishop Tuff contains melt inclusions that show relatively little variation in H_2O content, with an average of about 5.5 wt% H_2O (Skirius et al., 1990; Dunbar and Hervig, 1992; Wallace et al., 1999; Anderson et al., 2000; Wallace et al., 2003).

Quartz phenocrysts were separated from the Bishop Tuff by crushing and flotation. Several hundred crystals were loaded into a ≈3 cm long platinum capsule, and the open end was crimped (but not welded). The capsules were placed into a TZM furnace at 800° C and pressurized to 1 kbar using argon gas. Individual run durations were 4 hours, 12 hours, 24 hours, 2 days, 3 days, 7 days, 28 days, 54 days, and 63 days. After each run, the crystals were removed from the capsules and examined to identify quartz crystals containing melt inclusions located in the interior of the crystals and not along visible fractures. Some crystals were polished to expose the inclusions at the surface while others were left unpolished. Inclusions in these latter samples were thus located beneath the crystal surface when analyzed. Five unexposed inclusions were analyzed to determine the H_2O content. They were then exposed at the surface by polishing and re-analyzed to determine if sample preparation affected the results.

During Raman analysis, the confocal hole was adjusted to include the entire melt inclusion while minimizing the amount of quartz host in the analytical volume. The acquisition time was adjusted to offset the decreased intensity obtained when using smaller confocal hole settings for smaller inclusions. Acquisition times were increased as the inclusion size decreased and resulted in acquisition times ranging from 180 to 360 seconds (3 × 60 sec to 3 × 120 sec). A beam diameter of 2 μm results in an excitation volume of 6.3 and 12.5 μm^3 for focal depths of 2 and 4 μm, respectively, based on different confocal hole settings used in this study.

4.2 Results

Fourteen unheated melt inclusions from the Bishop Tuff were analyzed using UV excitation and H_2O contents were calculated using the calibration results presented above. Water contents range from 4.8 – 6.1 wt% (average 5.3 wt%; Fig. 5) and are consistent with the range of 4.7 and 6.5 wt% previously reported by other workers (Skirius et al., 1990; Dunbar and Hervig, 1992; Wallace et al., 1999; Anderson et al., 2000; Wallace et al., 2003). No significant differences were observed for inclusions that were analyzed both before and after being exposed at the surface (Table 2).

Inclusions that were held at temperature for 12 hours or less showed no significant H_2O loss when compared to unheated inclusions (Fig. 5; Table 2). However, some H_2O loss is evident after 24 hours of heating and melt inclusions lost about 75% of their original H_2O after 63 days. The range in H_2O contents at each time interval is similar to the range in H_2O contents for the early plinian phase of the Bishop Tuff reported by other workers (Fig. 5).

Water lost to the surrounding crystal should result in the creation of a "vacuum" bubble or expansion of a pre-existing bubble in order to accommodate the volume lost by H_2O leaving the inclusion (A. Anderson, pers. comm.). The volume change associated with H_2O loss can be calculated using mass balance constraints the partial molar volumes of H_2O and the melt. The molecular weight of H_2O is 18.0 g/mol, the molecular weight of the melt was assumed to be 186.374 g/mol for a typical granitic composition, the melt density was assumed to be 2.23 g/cm^3 and the partial molar volume of H_2O in the melt

was assumed to be 17.0 cm^3/mol (Student and Bodnar, 1996; Lange, 1994). We assumed 100 g of melt inside the inclusion for simplicity. The volume is defined as:

$$V_{MI} = M_{MI} / \rho_{melt}. \quad (1)$$

This results in an inclusion volume of 44.84 cm^3. A MI with 5 wt % H_2O contains 5 g H_2O and 95 g melt. The number of moles of H_2O is equal to:

$$Moles_{H2O} = X \text{ g } H_2O \times 1 \text{ mol } H_2O / 18.02 \text{ g } H_2O. \quad (2)$$

$$Moles_{H2O} = 5 \text{ g } H_2O \times 1 \text{ mol } H_2O / 18.02 \text{ g } H_2O = 0.2778 \text{ moles } H_2O$$

The number of moles of melt in the inclusion is:

$$Moles_{melt} = Y \text{ g melt} \times 1 \text{ mol} / 186.374 \text{ g/mol}. \quad (3)$$

$$Moles_{melt} = 95 \text{ g melt} \times 1 \text{ mol} / 186.374 \text{ g/mol} = 0.5097 \text{ moles melt}$$

The total number of moles in the inclusion is the sum of (2) and (3), or 0.7875 moles. The total molar volume of the inclusion is:

$$V_{molar} = V_{Total} / Moles_{total} \quad (4)$$

and using the values for the total number of moles and the total volume listed above results in a total molar volume of 56.94 cm^3/mol. This value can then be used to calculate the partial molar volume of melt in the inclusion according to:

$$V_{molar} = (moles_{melt}) \times (\overline{V}_{melt}) + (moles_{H2O}) \times (\overline{V}_{H2O}). \quad (5)$$

$$56.94 \text{ cm}^3/\text{mol} = (0.5097 \text{ moles}) \times (\overline{V}_{melt}) + (0.2778 \text{ moles}) \times (17.0 \text{ cm}^3/\text{mol})$$

results in a partial molar volume of the melt of 102.45 cm^3/mol.

If we assume the same inclusion (now containing 96 g) has lost 4 g of H_2O and only has 1 g H_2O left, substituting 1 g H_2O into equation (2) results in 0.0556 moles H_2O, and substituting 95 g melt into equation (3) results in 0.5097 moles melt for a total number of moles of 0.5653 in the inclusion. Inserting these two values into equation (5) and assuming the same partial molar volumes for the melt and for the H_2O, results in a total molar volume of 53.16 cm^3/mol. Inserting this value into equation (4) along with the total number of moles (0.5653) results in a total volume for the inclusion of 30.04 cm^3, which is 67.0% of the original volume (44.84 cm^3).

A decrease in the H_2O content from 5 wt% to 1 wt% (which approximately mimics the H_2O loss from the Bishop Tuff melt inclusions after 54 days of heating, Fig. 5) should result in a volumetric change of approximately 33.0%. For a 30 μm diameter spherical melt inclusion this represents a volume of 4665 μm^3. If the entire volume

decrease is accommodated by a spherical bubble, the bubble will have a diameter of 20.73 μm which is approximately 69% of the diameter of the inclusion.

To test this hypothesis, photomicrographs of melt inclusions from three different heating experiments (48 hours, 168 hours, and 1296 hours) were examined using image analysis software to measure the area percentage of the inclusion occupied by the vapor bubble as a proxy for the volume percentage. Each inclusions was photographed at either 50X or 100X magnification and a 100 μm scale bar was used to calibrate the software. The inclusion area was determined by outlining the inclusion using a polygonal selection tool with a measure option. The area of the bubble was estimated by using an ellipse tool combined with the measure option. The proportion of the inclusion occupied by the bubble was then calculated.

The observed results do not match the 33.0% volume loss predicted by the calculation. The proportion of the MI occupied by the bubble for the 54 day experiment (which best matches the values used in the calculation) show a range in bubble ratios from 0.2% to 9.3%, with an average of 2.8%. The results for shorter experiments (48 hours and 7 days) show a smaller range in bubble ratios with the 48 hour samples showing negligible bubble formation. The results indicate that bubbles are larger for inclusions held at elevated temperature for longer time periods. However, they do not approach the size (bubble proportion) predicted by the calculation above.

One possible explanation for the large range in bubble size is that the calculation does not account for the initial presence of a bubble of some size. The wide range of observed bubble sizes could also indicate that less than 4 g of H_2O was lost. The range of H_2O contents for 54 day experiments ranges from about 0.9 to 2.5 wt%. However, the difference between the calculated bubble size and the observed sizes remains unexplained.

The most important driving force for H_2O loss is a H_2O activity (or fugacity) gradient between the inclusion and surrounding quartz host. After a few hundred hours of heating, the rate of H_2O loss appears to decrease (Fig. 5). The decreasing rate of H_2O loss suggests a change in either the speciation or the mechanism of H_2O loss from the inclusion with time. For low H_2O content rhyolitic melts, H_2O is present mostly as OH, whereas molecular H_2O becomes more important at higher H_2O contents (Tomozawa,

1985; Chekhmir et al., 1989; Stolper, 1989; Silver et al., 1990; Zhang et al., 1991). For the observed H_2O contents in Bishop Tuff melt inclusions, H_2O should be present mostly as molecular H_2O. NMR and IR spectroscopy suggest that OH groups in the melt are structurally bonded to Si or Al (i.e. Wu, 1980; Schmidt et al., 2001). These observations suggest that the initial loss of H_2O from the inclusions involves molecular H_2O.

The loss of molecular H_2O can be attributed to one of two mechanisms. The first mechanism involves the dissociation of molecular H_2O according to the reaction

$$H_2O + Fe^{2+} \rightarrow \frac{1}{2} H_2 + OH^- + Fe^{3+}$$

The charge balance would most likely be offset by oxidation of Fe in the melt but could be accomplished by oxidation of other metals in the melt. Hydrogen diffuses rapidly through quartz and into and out of inclusions at temperatures higher than 400-500° C (Mavrogenes and Bodnar, 1994), while OH^- is expected to diffuse more slowly due to its larger molecular size. Massare et al. (2002) explained the formation of iron oxides in melt inclusions during heating to be the result of an increase in the oxidation state of the melt as a result of this process.

A second interpretation of the initial H_2O loss is that molecular H_2O itself diffuses out of inclusions along either preexisting or strain-induced dislocations in the host quartz. As H_2O diffuses out of the inclusion along dislocations, hydrolytic weakening and plastic deformation occur which facilitates the formation and growth of additional dislocations (Kronenberg et al., 1986; Gerretsen et al., 1989; Cordier et al., 1994). This behavior has been documented for H_2O loss from aqueous fluid inclusions during reequilibration (Bakker and Jansen, 1990; Vityk et al., 2000).

In quartz molecular H_2O diffuses more rapidly than hydroxyl groups (Farver and Yund, 1991), suggesting that the decrease in the rate of H_2O loss from the melt inclusions after a few hundred hours of heating represents a change from a molecular-H_2O dominated mechanism to one in which OH^- is the dominant species. Additionally, charged species typically have slower diffusion rates compared to uncharged species, regardless of size (Fortier and Giletti, 1989; Yund and Snow, 1989; Farver and Yund, 1991). The different rates of H_2O loss from the Bishop Tuff melt inclusions can thus be attributed to the loss of molecular H_2O initially and then the subsequent loss of OH^- groups that diffuse more slowly.

Another possible explanation is that molecular H_2O is lost along microcracks that form at the quartz α-β transition at 573° C (at 1 atm pressure, with the temperature of the phase transition increasing ≈25°C per kbar) as has been shown for fluid inclusions (Bodnar et al., 1989). The fracturing that occurs around inclusions when quartz passes through the α-β transition is a result of the large pressure differential between the inclusion and the surrounding medium. Thus, fracturing is reduced if the external pressure is at or above the pressure in the inclusion. By heating the Bishop Tuff melt inclusions at 1 kbar, the pressure differential, and thus the likelihood of fracturing and H_2O loss, is less than would be expected if the samples were heated at 1 atm. Finally, hydrogen could be lost as HF or other similar species, but this is unlikely for the Bishop Tuff inclusions based on the low concentration of F in the MI (Dunbar and Hervig, 1992; Anderson et al., 2000).

5. Conclusions

Laser Raman spectroscopy provides a simple, nondestructive technique to determine H_2O contents of silicate glasses, including melt inclusions as small as 5-10 μm. In this study, we have documented the use of ultraviolet (244 nm) excitation to minimize fluorescence. Results indicate that UV Raman excitation produces data of similar quality to that obtained using visible Raman excitation, but results in a different calibration curve. The UV-Raman technique can be used to determine H_2O contents of fluorescent glasses and melt inclusions that cannot be analyzed using visible wavelength Raman spectroscopy.

While this manuscript was in review, Thomas et al. (2006), and Di Muro et al. (2006) both published results describing a technique for determining H_2O contents of melt inclusions based on comparison of peak ratios for the unknown and a single standard of known H_2O content. The H_2O peak area ratio (3100-3750 cm^{-1}) for the standard and unknown equals the ratio of the H_2O content of the standard and unknown. Several unheated melt inclusions that had been analyzed previously in this study using the technique described in section 3 above were reanalyzed using UV Raman to confirm the applicability of the newer method. The results shown in Figure 7 indicate a good 1:1

correlation between these two techniques suggesting that the single-standard technique can also be applied when using a UV excitation source.

The UV-Raman technique was used to monitor H_2O loss from melt inclusions in the Bishop Tuff that were held at 800°C and 1 kbar for periods of time ranging from 4 hours to 63 days. Our results suggest that significant H_2O is not lost during heating experiments of 12 hours or less. However, as much as 75% of the H_2O in melt inclusions was lost when held at temperature for several hundred hours. The rate of H_2O loss decreases with time, consistent with a mechanism that involves loss of molecular H_2O initially, followed by OH^- as the H_2O content of the inclusion decreases.

Acknowledgements

The authors would like to thank Charles Farley for technical assistance with the Raman microprobe. Beth Glusica assisted with Raman analyses. Jake Lowenstern provided useful suggestions on melt inclusion techniques, Larry Anovitz clarified our understanding of the behavior of H_2O in silicate glasses, and Don Rimstidt for refining our interpretation of the diffusion mechanism. Special thanks to Fred Anderson, who introduced us to the Bishop Tuff and helped us to better understand the process of H_2O loss from melt inclusions. We are indebted to Rainer Thomas and Jean Dubessy for their constructive reviews that significantly improved this manuscript. Partial funding for this project was provided by NSF grants EAR-0337094 and EAR-0322119 to RJB.

References:

Anderson, A.T., Jr., Davis, A.M., Lu, F., 2000. Evolution of Bishop Tuff rhyolitic magma based on melt and magnetite inclusions and zoned phenocrysts. Journal of Petrology 41, 449-473.

Bakker, R.J., Jansen, J.B.H., 1990. Preferential water leakage from fluid inclusions by means of mobile dislocations. Nature 345, 58-60.

Bodnar, R.J., 1995. Fluid inclusion evidence for a magmatic source for metals in porphyry copper deposits. In: Thompson, J. F. H. (Ed.), Mineralogical Association of Canada Short Course Volume 23, Magmas, Fluids and Ore Deposits, 139-152.

Bodnar, R.J., 2003a. Introduction to fluid inclusions. In: Samson, I., Anderson, A., & Marshall, D. (Eds.), Fluid Inclusions: Analysis and Interpretation. Mineral. Assoc. Canada, Short Course 32, 1-8.

Bodnar, R.J., 2003b. Reequilibration of fluid inclusions. In: Samson, I., Anderson, A., & Marshall, D. (Eds.), Fluid Inclusions: Analysis and Interpretation. Mineral. Assoc. Canada, Short Course 32, 213-230.

Bodnar, R.J., Student, J.J., 2006. Melt inclusions in plutonic rocks: Petrography and microthermometry. In: Webster, J.D. (Ed.), Melt Inclusions in Plutonic Rocks. Mineral. Assoc. Canada, Short Course 36, 1-26.

Bodnar, R.J., Binns, P.R., Hall, D.L., 1989. Synthetic fluid inclusions – VI. Quantitative evaluation of the decrepitation behavior of fluid inclusions in quartz at one atmosphere confining pressure. Journal of Metamorphic Geology 7, 229-242.

Burnham, C.W., 1979. Magmas and hydrothermal fluids. In: Barnes, H.L. (Ed.), Geochemistry of Hydrothermal Ore Deposits 1st Ed., pp. 71-136. John Wiley & Sons Ltd., New York.

Burnham, C.W., 1997. Magmas and hydrothermal fluids. In: Barnes, H.L. (Ed.), Geochemistry of Hydrothermal Ore Deposits 3rd Ed., pp. 63-123. John Wiley & Sons Ltd., New York.

Chabiron, A., Pironon, J., Massare, D., 2004. Characterization of water in synthetic rhyolitic glasses and natural melt inclusions by Raman spectroscopy. Contributions to Mineralogy and Petrology 146, 485-492.

Chekhmir, A.S., Epel'Baum, M.B., Simakin, A.G., 1989. Transport of water in magmatic melts. Geochemistry International 10, 125-127.

Cordier, P., Doukhan, J-C., Ramboz, C., 1994. Influence of dislocations on water leakage from fluid inclusions in quartz: A quantitative reappraisal. European Journal of Mineralogy 6, 745-752.

Danyushevsky, L.V., Della-Pasqua, F.N., Sokolov, S., 2000. Re-equilibration of melt inclusions trapped by magnesian olivine phenocrysts from subduction-related magmas: petrologic implications. Contributions to Mineralogy and Petrology 138, 68-83.

Di Muro, A., Villemant, B., Montagnac, G., Scaillet, B., Reynard, B., 2006, Quantification of water content and speciation in natural silicic glasses (phonolite, dacite, rhyolite) by confocal microRaman spectroscopy. Geochimica et Cosmochimica Acta 70, 2,868-2,884.

Dunbar, N.W., Hervig, R.L., 1992. Petrogenesis and volatile stratigraphy of the Bishop Tuff: Evidence from melt inclusion analysis. Journal of Geophysics Research 97, 15,129-15,150.

Farver, J.R., Yund, R.A., 1991. Oxygen diffusion in quartz: Dependence of temperature and water fugacity. Chemical Geology 90, 55-70.

Fortier, S.M., Giletti, B.J., 1989. An empirical model for predicting diffusion coefficients in silicate minerals. Science 245, 1481-1484.

Gerretsen, J., Paterson, M.S., McLaren, A.C., 1989. The uptake and solubility of water in quartz at elevated pressures and temperature. Physics and Chemistry of Minerals 16, 334-342.

Holtz, F., Beny, J-M., Mysen, B.O., Pichavant, M. 1996. High-temperature Raman spectroscopy of silicate and aluminosilicate hydrous glasses: Implications for water speciation. Chemical Geology 128, 25-39.

Keresztury, G., 2002. Raman-spectroscopy: Theory. In: Chalmers, J.M., Griffiths, P.R. (Eds.), Handbook of Vibrational Spectroscopy 1, p. 71-87. John Wiley & Sons Ltd., Chichester, England.

Kronenberg, A.K., Kirby, S.H., Aines, R.D., Rossman, G.R., 1986. Solubility and diffusional uptake of hydrogen in quartz: Implications for hydrolytic weakening. Journal of Geophysics Research 91, 12723-12744.

Lange, R.A., 1994. The effect of H_2O, CO_2, and F on the density and viscosity of silicate melts. In: Carroll, M.R., & Holloway, J.R. (Eds.), Reviews in Mineralogy 30, pp. 331-369. Mineralogical Society of America, Washington, DC.

Long, D.A., 2002. The Raman effect: A unified treatment of the theory of Raman scattering by molecules. John Wiley & Sons Ltd., Chichester, England.

Lowenstern, J.B., 1995. Applications of silicate melt inclusions to the study of magmatic volatiles. In: Thompson, J. F. H. (Ed.), Magmas, Fluids, and Ore Deposits, Short Course 23, p. 71-101. Mineralogical Association of Canada, Victoria.

Mandeville C.W., Webster, J.D., Rutherford, M.J., Taylor, B.E., Timbal, A., Faure, K., 2002. Determination of extinction coefficients for infrared absorption bands of H_2O in andesitic glasses. American Mineralogist 87, 813-821.

Massare, D., Metrich, N., Clocchiatti, R., 2002. High-temperature experiments on silicate melt inclusions in olivine at 1 atm: inferences on temperature of homogenization and H_2O concentrations. Chemical Geology 183, 87-98.

Massare, D., Metrich, N., Thellier, B., Clocchiatti, R., 1998. Evidence of H_2O loss in melt inclusions after a series of heating stage experiments. Terra Abstracts 10, 39.

Matson, D.W., Sharma, S.K., Philpotts, J.A., 1983. The structure of high-silica alkali-silicate glasses – A Raman-spectroscopic investigation. Journal of Non-Crystaline Solids 58, 323-352.

Mavrogenes, J.A., Bodnar, R.J., 1994. Hydrogen movement into and out of fluid inclusions in quartz: Experimental evidence and geologic implications. Geochimica et Cosmochimica Acta 58, 141-148.

McMillan, P.F., 1994. Water solubility and speciation models. In: Carroll, M.R., & Holloway, J.R. (Eds.), Reviews in Mineralogy 30, pp. 131-156. Mineralogical Society of America, Washington, DC.

McMillan, P.F., Piriou, B., Navrotsky, A., 1982. A Raman-spectroscopic study of glasses alongs the joins silica-calcium aluminate, silica-sodium aluminate, and silica-potassium aluminate. Geochimica et Cosmochimica Acta 46, 2021-2037.

McMillan, P.F., Wolf, G.H., 1995. Vibrational spectroscopy of silicate liquids. In: Stebbins, J., McMillan, P.F., & Dingwell, D.B. (Eds.), Reviews in Mineralogy 32, p. 247-315. Mineralogical Society of America, Washington, DC.

McMillan, P.F., Wolf, G.H., Poe, B.T., 1992. Vibrational spectroscopy of silicate liquids and glasses. Chemical Geology 96, 351-366.

Mysen, B.O., 1997. Aluminosilicate melts: Structure, composition and temperature. Contributions to Mineralogy and Petrology 127, 104-118.

Mysen, B.O., 1999. Structure and properties of magmatic liquids: From haplobasalt to haploandesite. Geochimica et Cosmochimica Acta 63, 104-118.

Pasteris, J.D., Wopenka, B., Seitz, J.C., 1988. Practical aspects of quantitative laser Raman microprobe spectroscopy for the study of fluid inclusions. Geochimica et Cosmochimica Acta 52, 979-988.

Qin, Z., Lu, F., Anderson, A.T., Jr., 1992. Diffusive reequilibration of melt and fluid inclusions. American Mineralogist 77, 565-576.

Roedder, E., 1984. Fluid Inclusions. Reviews in Mineralogy 12. Mineralogical Society of America, Washington, D.C.

Schmidt, B.C., Behrens, H., Riemer, T., Kappes, R., Dupree, R., 2001. Quantitative determination of water speciation in aluminosilicate glasses: A comparative NMR and IR spectroscopic study. Chemical Geology 174, 195-208.

Seifert, F.A., Mysen, B.O., Virgo, D., 1981. Structural similarity of glasses and melts relevant to petrological processes. Geochimica et Cosmochimica Acta 45, 1879-1884.

Sharma, S.K., Cooney, T.F., Wang, Z.F., vanderLaan, S., 1997. Raman band assignments of silicate and germinate glasses using high-pressure and high-temperature spectral data. Journal of Raman Spectroscopy 28, 697-709.

Silver, L.A., Ihinger, P.D., Stolper, E.M., 1990. The influence of bulk composition on the speciation of water in silicate glasses. Contributions to Mineralogy and Petrology 104, 142-162.

Skirius, C.M., Peterson, J.W., Anderson, A.T., Jr., 1990. Homogenizing rhyolitic glass inclusions from the Bishop Tuff. American Mineralogist 75, 1381-1398.

Smith, E., and Dent, G., 2005. Modern Raman spectroscopy: A practical approach. John Wiley & Sons, Ltd. Chichester, England.

Sparks, R.S.J., Barclay, J., Jaupart, C., Mader, H.M., Phillips, J.C., 1994. Physical aspects of magmatic degassing I. Experimental and theoretical constraints on vesiculation. In: Carroll, M.R., & Holloway, J.R. (Eds.),Reviews in Mineralogy 30, pp. 413-445. Mineralogical Society of America, Washington, DC.

Stolper, E.M., 1989. Temperature dependence of the speciation of water in rhyolitic melts and glasses. American Mineralogist 74, 1247-1257.

Student, J.J., Bodnar, R.J., 1996. Melt inclusion microthermometry: Petrologic constraints from the H_2O-saturated haplogranite system. Petrology 4, 291-306.

Student, J.J., Bodnar, R.J., 1999. Synthetic fluid inclusions XIV: Coexisting silicate melt and fluid inclusions in the haplogranite-H_2O-NaCl-KCl system. Journal of Petrology 40, 1509-1525.

Student, J.J., Bodnar, R.J., 2004. Silicate melt inclusions in porphyry copper deposits: Identification and homogenization behavior. Canadian Mineralogist, 42,1563-1600.

Thomas, J.B., Bodnar, R.J., Farley, C., 2002. A further test of the Raman technique for determining water contents of silicate glasses. In: Kontak, D.J., & Anderson, A.J. (Eds.), 8th Biennial Pan-American Conference on the Research on Fluid Inclusions, Program with Abstracts, Nova Scotia Department of Natural Resources, p. 105.

Thomas, R., 2000. Determination of water contents of granite melt inclusions by confocal laser Raman microprobe spectroscopy. American Mineralogist 85, 868-872.

Thomas, R., 2002a. Determination of water contents in melt inclusions by laser Raman spectroscopy. In: De Vivo, B., & Bodnar, R.J. (Eds.), Proceedings from the Workshop – Short Course on volcanic systems, geochemical and geophysical monitoring – Melt inclusions: methods, applications and problems. Sept. 26-30 in Napoli, Italy, pp. 211-216.

Thomas, R., 2002b. Determination of the H_3BO_3 concentration in fluid and melt inclusions in granite pegmatites by laser Raman microprobe spectroscopy. American Mineralogist 87, 56-68.

Thomas, R., Kamenetsky, V.S., Davidson, P., 2006. Laser Raman spectroscopic measurements of water in unexposed glass inclusions. American Mineralogist 91, 467-470.

Tomozawa, M., 1985. Concentration dependence of the diffusion coefficient of water in SiO_2 glass. Journal of American Ceramics Society 68, C251-C252.

Vityk M.O., Bodnar R.J., Doukhan, J-C., 2000. Synthetic fluid inclusions: XV. TEM investigation of plastic flow associated with re-equilibration of synthetic fluid inclusions in natural quartz. Contributions to Mineralogy and Petrology 139, 285 297.

Voigt D.E., Bodnar R.J., Blencoe J.G., 1981. Water solubility in melts of alkali feldspar composition at 5 kbar and 950°C. EOS, 62, 428.

Wallace, P.J., Anderson, A.T., Jr., Davis, A.M., 1999. Gradients in H_2O, CO_2, and exsolved gas in a large-volume silicic magma system: Interpreting the record preserved in melt inclusions from the Bishop Tuff. Journal of Geophysical Reviews 104, 20097-20122.

Wallace, P.J., Dufek, J., Anderson, A.T., Jr., Zhang, Y., 2003. Cooling rates of Plinian fall and pyroclastic-flow deposits in the Bishop Tuff: Inferences from water speciation in quartz-hosted glass inclusions. Bulletin of Volcanology 65, 105-123.

Wang, Z.F., Cooney, T.F., Sharma, S.K., 1993. High-temperature structural investigation of $(Na_2O)_{0.5}(Fe_2O_3)_{0.3}SiO_2$ and $Na_2O(FeO)_3SiO_2$ melts and glasses. Contributions to Mineralogy and Petrology 115, 112-122.

Wu, C.K., 1980. Nature of incorporated water in hydrated silicate glasses. Journal of the American Ceramic Society 63, 453-457.

Yund, R.A., Snow, E., 1989. Effects of hydrogen fugacity and confining pressure on the interdiffusion rate of NaSi-CaAl in plagioclase. Journal of Geophysical Research 94, 10662-10668.

Zajacz, Z., Halter, W., Malfait, W.J., Bachmann, O., Bodnar, R.J., Hirschmann, M.M., Mandeville, C.W., Morizet, Y., Müntener, O., Ulmer, P., Webster, J.D., 2005. A

composition-independent quantitative determination of the water content in silicate glasses and silicate melt inclusions by confocal Raman-spectroscopy. Contributions to Mineralogy and Petrology 150, 631-642.
Zhang, Y., Stolper, E.M., Wasserburg, G.J., 1991. Diffusion of water in rhyolitic glasses. Geochimica et Cosmochimica Acta 55, 441-456.

Tables

Table 1. Description of Glass Standards used for Raman Calibration

Sample #	Composition	H_2O wt%	Reference
022881 XII	$Na_{0.5}K_{0.5}AlSi_3O_8$	7.04	Voigt et al. (1981)
032481 VI	$Na_{0.25}K_{0.75}AlSi_3O_8$	6.72	Voigt et al. (1981)
032481 VII	$Na_{0.75}K_{0.25}AlSi_3O_8$	8.08	Voigt et al. (1981)
032481 VIII	$Na_{0.75}K_{0.25}AlSi_3O_8$	8.06	Voigt et al. (1981)
040281 I	$KAlSi_3O_8$	4.28	Voigt et al. (1981)
040281 II	$KAlSi_3O_8$	4.61	Voigt et al. (1981)
040281 III	$KAlSi_3O_8$	4.93	Voigt et al. (1981)
040281 IV	$KAlSi_3O_8$	5.51	Voigt et al. (1981)
040681 X	$NaAlSi_3O_8$	9.5	Voigt et al. (1981)
041581 II	$Na_{0.1}K_{0.9}AlSi_3O_8$	6.45	Voigt et al. (1981)
041581 XII	$Na_{0.1}K_{0.9}AlSi_3O_8$	5.5	Voigt et al. (1981)
Ab 1-0	$NaAlSi_3O_8$	0.98	Previously Unpublished
Ab 1-5	$NaAlSi_3O_8$	1.53	Previously Unpublished
Ab 1196 A	$NaAlSi_3O_8$	2.17	Previously Unpublished
Run 10	See Reference	5.78	Mandeville et al. (2002)
Run 58a	See Reference	5.68	Mandeville et al. (2002)
Run 68	See Reference	2.15	Mandeville et al. (2002)
Run 106	See Reference	1.31	Mandeville et al. (2002)

Table 2. Results of Raman analysis of melt inclusions in early-erupted Bishop Tuff quartz

Sample Name	**3550**	**850-1250**	**R**	**H_2O wt%**
0 A	337573.9	58170.7	5.803	5.0
0 A Polished	890570.0	154420.0	5.767	5.0
0 B	39016.4	6451.9	6.047	5.2
0 B Polished	579864.1	96567.0	6.005	5.2
0 C	76134.1	13303.8	5.723	4.9
0 C Polished	535982.1	93126.4	5.755	4.9
0 D	160291.8	25598.5	6.262	5.4
0 D Polished	961750.6	154387.1	6.229	5.4
0 E	163423.7	24595.0	6.645	5.7
0 E Polished	653694.9	97891.7	6.678	5.7
0 F	87203.7	14946.4	5.834	5.0
0 G	63905.5	11290.9	5.660	4.9
0 H	12456.0	2024.0	6.154	5.3
0 I	20581.8	2723.4	7.557	6.5
0 Average			6.151	5.3
4 A	10239.4	2009.7	5.095	4.4
4 B	58224.0	10655.5	5.464	4.7
4 C	10373.9	1406.5	7.376	6.3
4 D	4572.9	824.3	5.548	4.8
4 E	31936.4	6384.2	5.002	4.3
4 F	9616.5	1561.3	6.159	5.3
4 G	14888.8	1999.9	7.445	6.4
4 H	63867.3	12054.9	5.298	4.6
4 I	87751.2	15372.0	5.709	4.9
4 J	43988.9	8492.5	5.180	4.5
4 K	29820.7	5186.8	5.749	4.9
4 L	35960.0	6653.8	5.404	4.6
4 M	33646.2	6653.8	5.057	4.3
4 N	5811.4	1155.2	5.031	4.3
4 O	91122.6	14280.4	6.381	5.5
4 P	21110.6	3039.0	6.947	6.0
4 Q	11958.9	1776.7	6.731	5.8
4 R	57842.2	8829.3	6.551	5.6
4 S	13592.3	2257.2	6.022	5.2
4 T	11601.9	1854.5	6.256	5.4
4 U	1864.7	349.0	5.343	4.6
4 V	12951.9	2514.7	5.150	4.4
4 Average			5.859	5.0
12 A	43863.1	7432.6	5.901	5.1
12 B	9772.0	1914.4	5.104	4.4
12 C	174012.7	34677.3	5.018	4.3
12 D	6304.3	927.0	6.801	5.8
12 E	8922.4	1358.5	6.568	5.6
12 F	45032.2	8561.0	5.260	4.5

12 G	22588.3	4325.0	5.223	4.5
12 H	8940.8	1477.9	6.050	5.2
12 I	24582.1	4701.0	5.229	4.5
12 J	8236.0	1297.0	6.350	5.5
12 K	42233.0	6832.0	6.182	5.3
12 L	25212.3	4865.0	5.182	4.5
12 Average			5.739	4.9
24 A	237611.6	48126.5	4.937	4.2
24 B	22023.4	3370.8	6.534	5.6
24 C	37057.6	7600.1	4.876	4.2
24 D	408362.7	74612.3	5.473	4.7
24 E	78983.2	16945.3	4.661	4.0
24 F	24532.5	4953.0	4.953	4.3
24 G	46157.8	10118.0	4.562	3.9
24 H	6728.2	1389.3	4.843	4.2
24 I	10672.7	1902.0	5.611	4.8
24 J	80428.9	17596.7	4.571	3.9
24 K	16431.7	3184.1	5.161	4.4
24 L	127979.6	27474.9	4.658	4.0
24 Average			5.070	4.4
48 A	6084.0	1957.8	3.108	2.7
48 B	2631.7	717.9	3.666	3.2
48 C	4434.2	983.4	4.509	3.9
48 D	6124.4	1894.4	3.233	2.8
48 E	36217.2	11111.4	3.259	2.8
48 F	14861.5	4562.0	3.258	2.8
48 G	49478.3	14472.3	3.419	2.9
48 H	9661.8	1700.9	5.680	4.9
48 I	3882.6	583.7	6.652	5.7
48 J	6517.1	997.3	6.535	5.6
48 K	12760.4	3636.1	3.509	3.0
48 L	23937.5	7537.7	3.176	2.7
48 M	22467.1	4775.3	4.705	4.0
48 Average			4.208	3.6
168 A	36546.5	20787.1	1.758	1.5
168 B	7413.4	3678.0	2.016	1.7
168 C	58247.0	17997.3	3.236	2.8
168 D	80604.7	19941.2	4.042	3.5
168 E	22385.7	12115.6	1.848	1.6
168 F	19126.3	11005.2	1.738	1.5
168 G	91287.5	42199.1	2.163	1.9
168 H	35470.8	22458.4	1.579	1.4
168 I	84446.3	43043.7	1.962	1.7
168 J	9177.5	3954.0	2.321	2.0
168 K	34648.4	21476.0	1.613	1.4
168 L	102257.1	37266.5	2.744	2.4
168 M	106844.2	37985.7	2.813	2.4

168 N	120460.2	38026.6	3.168	2.7
168 O	35314.7	16734.6	2.110	1.8
168 P	64853.8	26305.7	2.465	2.1
168 Average			2.349	2.0
672 A	67898.3	36798.5	1.845	1.6
672 B	81094.8	28505.4	2.845	2.4
672 C	20433.2	10343.8	1.975	1.7
672 D	73823.3	40029.9	1.844	1.6
672 E	9718.7	13607.7	0.714	0.6
672 F	60957.4	33291.3	1.831	1.6
672 G	29028.8	7554.2	3.843	3.3
672 H	32248.8	8826.5	3.654	3.1
672 Average			2.319	2.0
1296 A	78401.7	51819.6	1.513	1.3
1296 B	50046.9	40717.7	1.229	1.1
1296 C	46741.5	39027.1	1.198	1.0
1296 D	66828.6	37251.1	1.794	1.5
1296 E	76669.1	45049.1	1.702	1.5
1296 F	44399.0	41153.5	1.079	0.9
1296 G	91173.2	34620.3	2.634	2.3
1296 H	25488.1	9376.1	2.718	2.3
1296 I	88910.0	40120.2	2.216	1.9
1296 J	25960.1	23510.6	1.104	0.9
1296 K	40669.5	28456.1	1.429	1.2
1296 L	2999.9	1608.2	1.865	1.6
1296 M	3340.2	3622.0	0.922	0.8
1296 N	5235.1	3622.0	1.445	1.2
1296 O	4760.8	1759.7	2.705	2.3
1296 Average			1.704	1.5
1512 A	82751.7	47084.8	1.758	1.5
1512 B	92449.4	54674.5	1.691	1.5
1512 C	125377.6	56781.9	2.208	1.9
1512 D	88275.4	51238.8	1.723	1.5
1512 E	66219.5	59381.3	1.115	1.0
1512 F	81017.0	52485.3	1.544	1.3
1512 G	93659.7	55075.3	1.701	1.5
1512 H	68647.9	54556.0	1.258	1.1
1512 I	14000.8	22561.0	0.621	0.5
1512 J	78598.6	58766.8	1.337	1.1
1512 K	54206.9	33533.0	1.617	1.4
1512 L	92358.3	50565.5	1.827	1.6
1512 M	79727.4	51198.4	1.557	1.3
1512 N	30213.7	23218.5	1.301	1.1
1512 O	68454.7	42631.8	1.606	1.4
1512 P	19593.0	23585.7	0.831	0.7
1512 Q	66442.6	49579.3	1.340	1.2
1512 R	67300.5	27443.3	2.452	2.1

1512 S	39650.6	14468.3	2.741	2.4
1512 T	47617.4	15526.7	3.067	2.6
1512 U	76762.0	42574.0	1.803	1.5
1512 Average			1.671	1.4

3550 = Area under the H_2O peak at approximately 3550 cm^{-1}

850-1250 = Area under the T-O-T peak between 850 and 1250 cm^{-1}

R = Area under the 3550 cm^{-1} peak divided by the area under the 850-1250 cm^{-1} peak

Figures

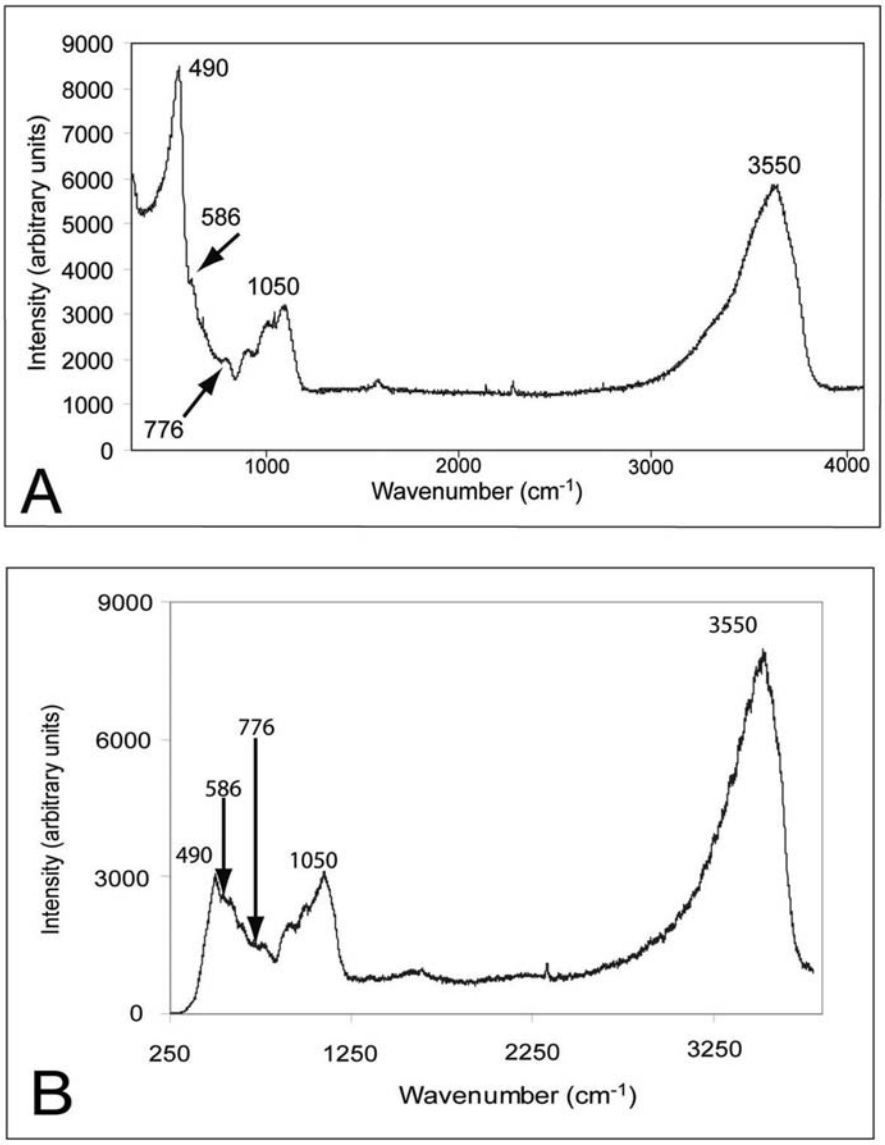

Fig. 1. A) Raman spectrum (after frequency–temperature correction) of alkali feldspar glass containing 4.93 wt.% H_2O produced using 514 nm (green) excitation. Labeled bands are the T–O–T symmetric stretching mode (490 cm^{-1}), glass defect peak (586 cm^{-1}), T–O–T bending mode (776 cm^{-1}) and a broad peak from 850–1250 cm^{-1} and centered at about 1050 cm^{-1} that represents T–O and T–O–T symmetric and assymetric stretching modes. The 3550 cm^{-1} band represents molecular water and hydroxyl groups in the glass. B) Raman spectrum (after frequency–temperature correction) of alkali feldspar glass standard containing 4.93 wt.% water analyzed with 244 nm (ultraviolet) excitation. Note the relative intensities of the 490 cm^{-1}, 586 cm^{-1}, and 776 cm^{-1} bands differ from those produced using visible excitation (Fig. 1a). The broad T–O–T band centered at 1050 cm^{-1} and the water band at 3550 cm^{-1} are similar to bands in the visible spectrum (A).

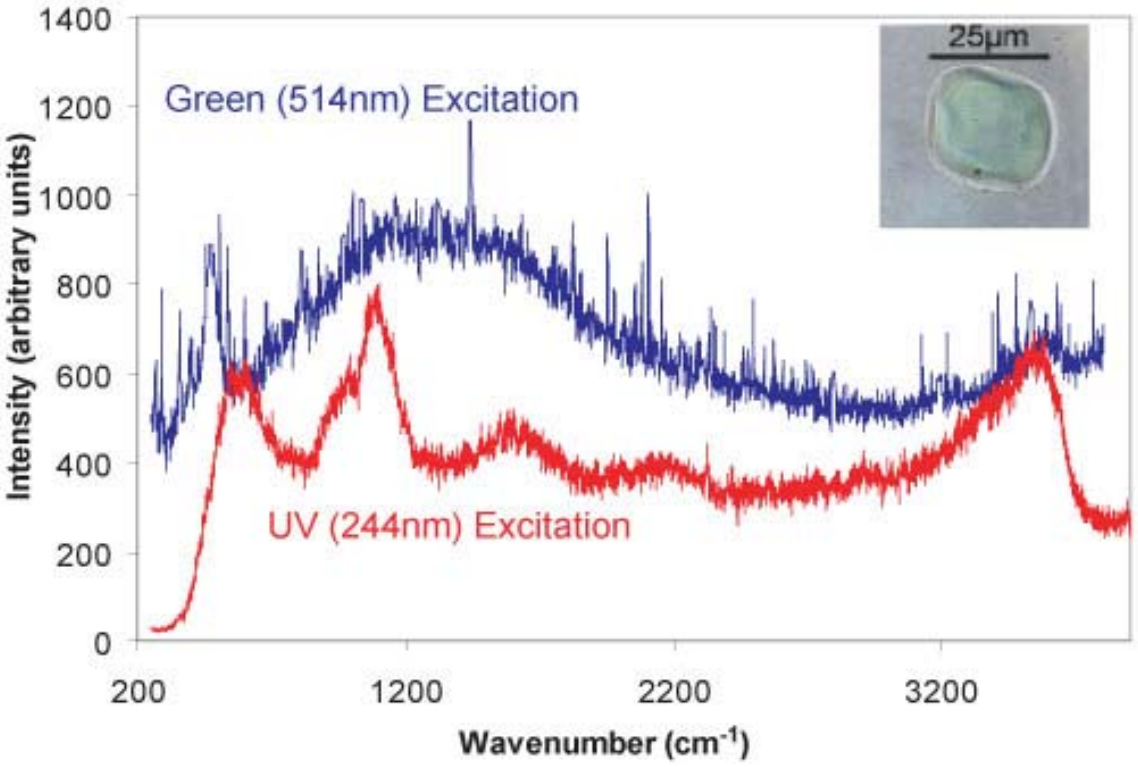

Fig. 2. Comparison of Raman spectra of a melt inclusion (inset) in quartz from the Bishop Tuff obtained using visible (514 nm) and ultraviolet (244 nm) excitation. The fluorescence intensity in the spectrum obtained with visible excitation masks several of the Raman bands and precludes an accurate determination of the peak areas.

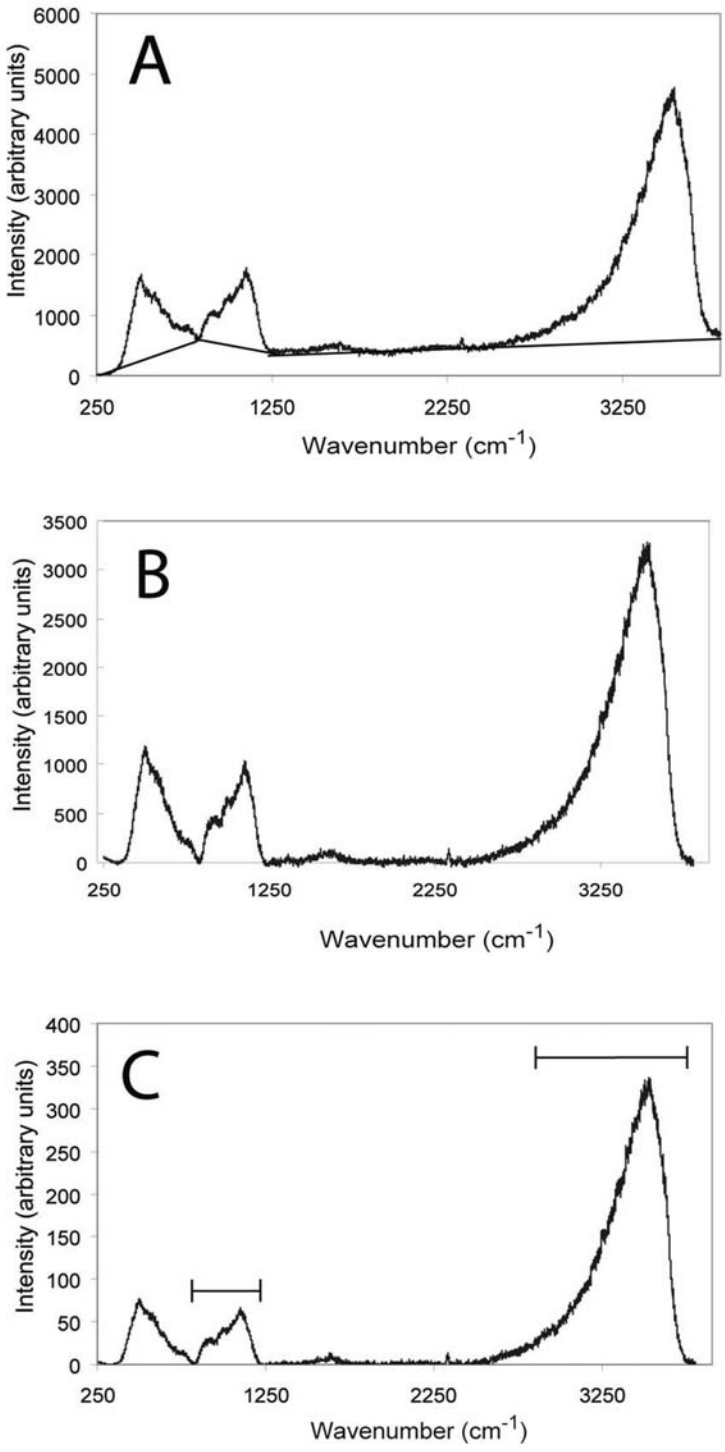

Fig. 3. Summary of the procedures used to treat Raman spectra obtained on hydrous glasses. A) The original spectrum showing the baseline correction. B) Spectrum after the baseline has been removed. C) The spectrum after the frequency–temperature correction was applied. The horizontal lines in (C) indicate the range of wavenumbers over which peak area integrations were performed.

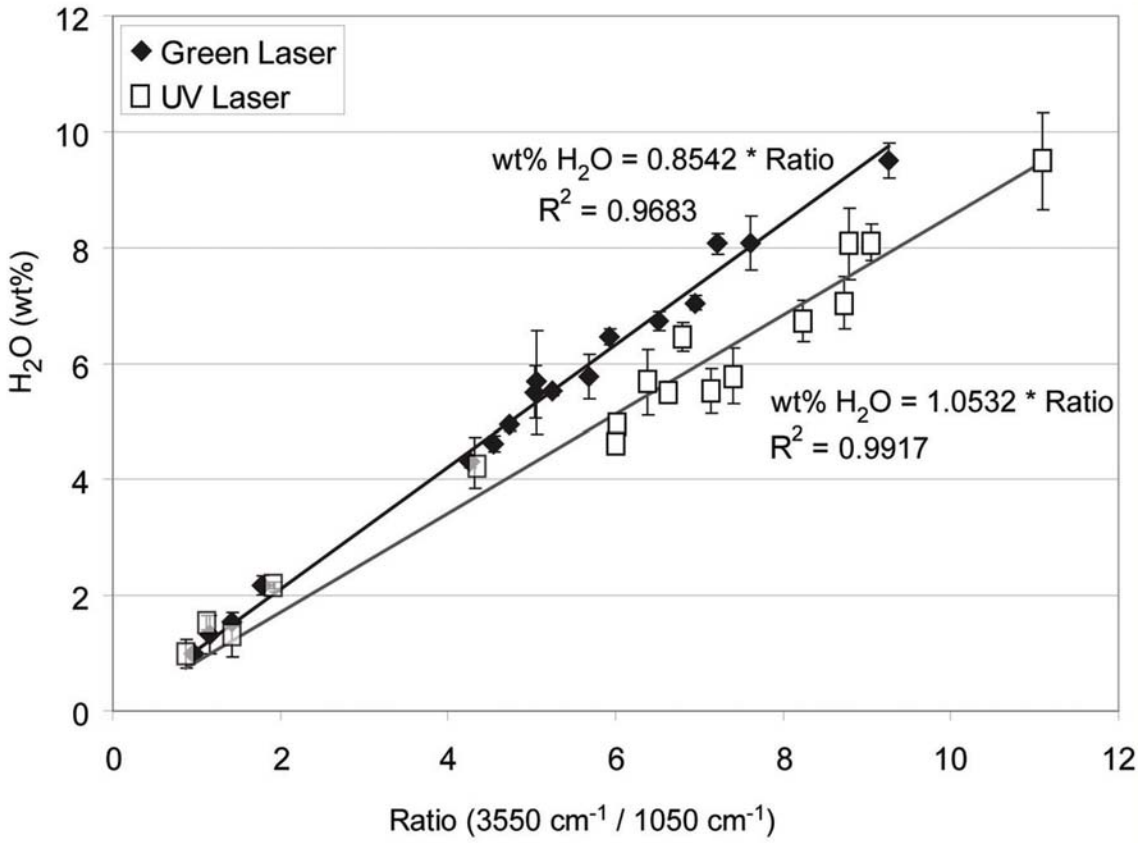

Fig. 4. Relationship between the amount of water in hydrous glass and the ratio between the water peak area at 3550 cm^{-1} and the T–O–T peak area band centered at 1050 cm^{-1}. Each data point represents the average of at least 10 analyses and includes 2σ error bars.

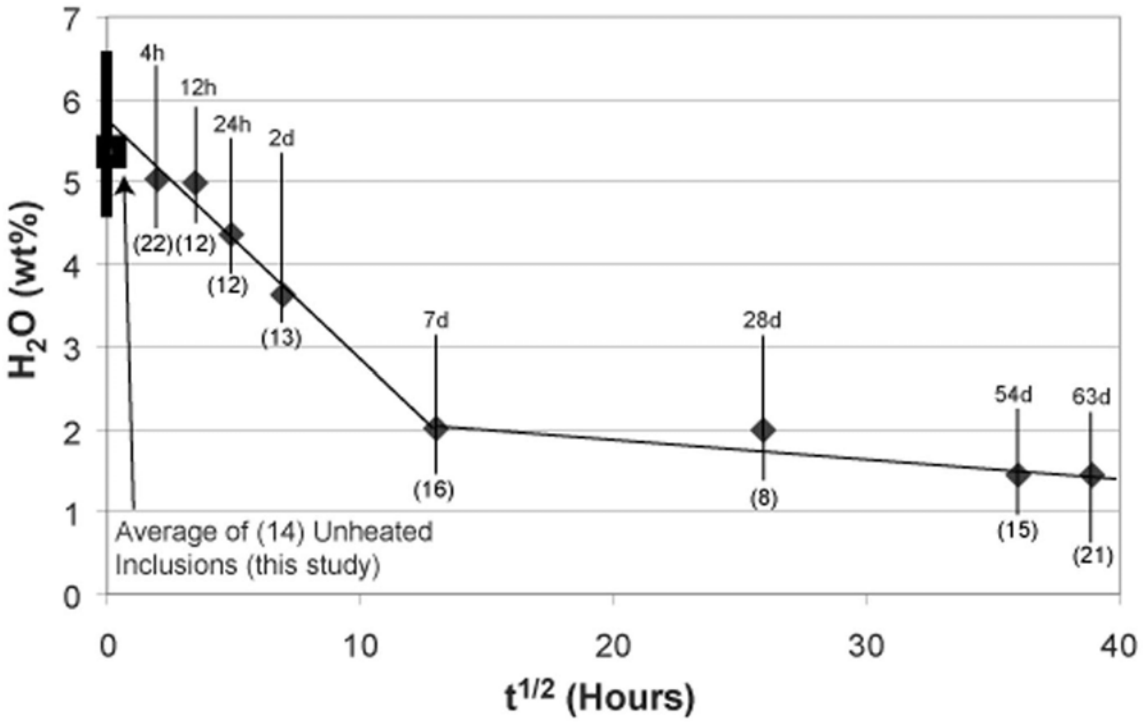

Fig. 5. Relationship between water content of melt inclusions in quartz from the Bishop Tuff and the amount of time held at 800 °C and 1 kbar. Each point represents the average of the measurements in each sample set. The thick line on the *y* axis is the range of water contents derived from previous studies. The vertical line through each data point represents the minimum and maximum values measured in that sample suite. The value in parentheses directly below the vertical line is the number of inclusions analyzed and the text above the line is the length of time in either hours (h) or days (d). The two lines drawn through all the samples represent the best fit linear equations to describe the different behaviors observed for the water loss.

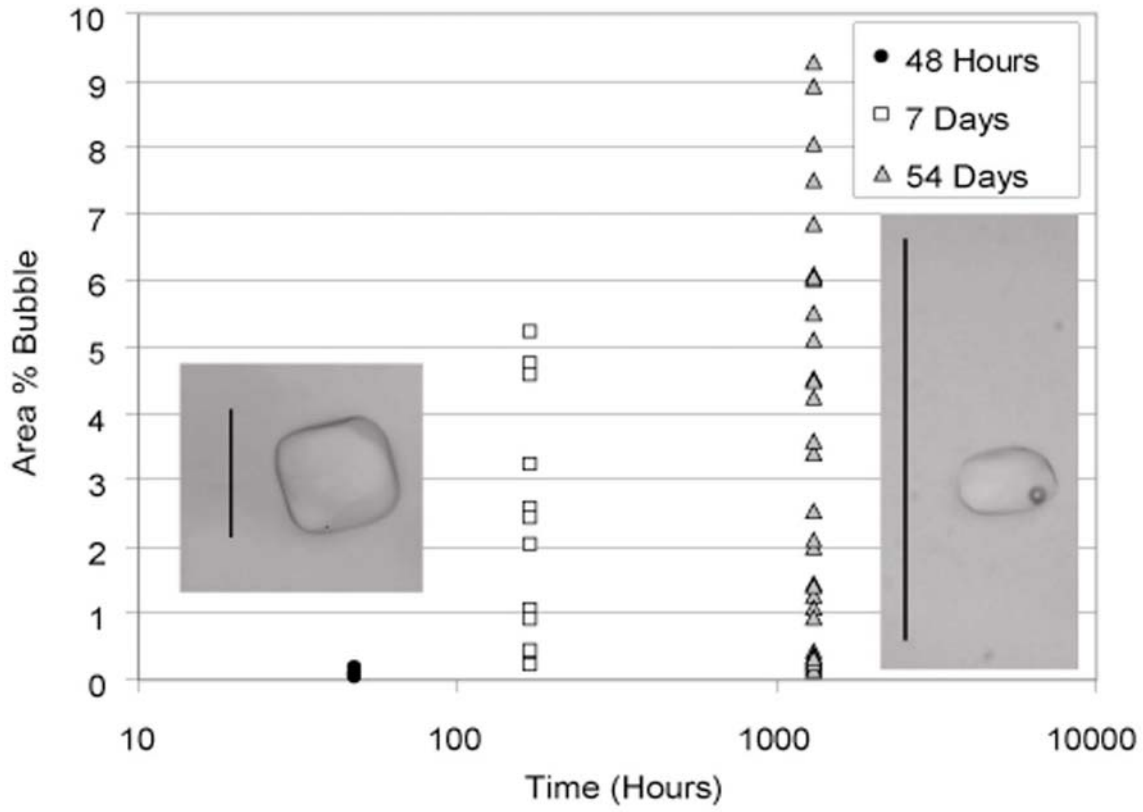

Fig. 6. Relationship between ratio of the bubble area to the total area of the melt inclusion and amount of time the inclusion was held at 800 °C and 1 kbar. The scale bar in the photomicrographs is 100 μm.

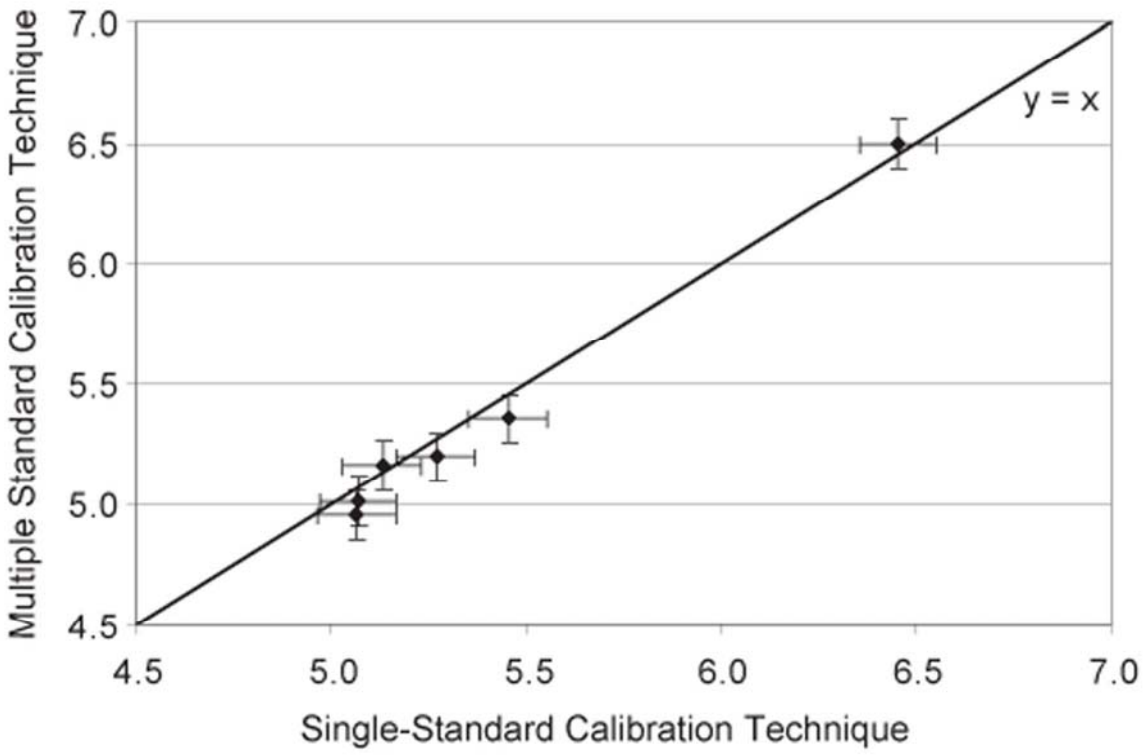

Fig. 7. Comparison between the single-standard technique used by Thomas et al. (2006) and Di Muro et al. (2006), and the multiple standard calibration technique used in Section 3 described above. A 1:1 line is plotted for comparison.

Publishing Agreement

Dear Mr Severs

We hereby grant you permission to reprint the material detailed below at no charge **in your thesis** subject to the following conditions:

1. If any part of the material to be used (for example, figures) has appeared in our publication with credit or acknowledgement to another source, permission must also be sought from that source. If such permission is not obtained then that material may not be included in your publication/copies.

2. Suitable acknowledgment to the source must be made, either as a footnote or in a reference list at the end of your publication, as follows:

   "This article was published in Publication title, Vol number, Author(s), Title of article, Page Nos, Copyright Elsevier (or appropriate Society name) (Year)."

3. Your thesis may be submitted to your institution in either print or electronic form.

4. Reproduction of this material is confined to the purpose for which permission is hereby given.

5. This permission is granted for non-exclusive world **English** rights only. For other languages please reapply separately for each one required. Permission excludes use in an electronic form other than submission. Should you have a specific electronic project in mind please reapply for permission.

6. This includes permission for UMI to supply single copies, on demand, of the complete thesis. Should your thesis be published commercially, please reapply for permission.

Yours sincerely

C. Truter

Clare Truter

Rights Manager

Chapter 3: Distribution of trace elements (REE, Sr, Ba, Y, Ti, Zr, Hf, Nb, Pb) between dacitic melt, plagioclase, orthopyroxene, and clinopyroxene: Evidence from silicate melt inclusions

Matthew J. Severs, Scott R. Mutchler, Robert J. Bodnar
Fluids Research Laboratory, Department of Geosciences, Virginia Polytechnic Institute and State University, Blacksburg VA 24061, USA

James Beard
Virginia Museum of Natural History, Martinsville, VA 24412, USA

Abstract

Partitioning behavior of Ti, Mn, Sr, Y, Zr, Nb, Ba, La, Nd, Sm, Eu, Gd, Dy, Ho, Yb, Hf, and Pb between silicate melt and clinopyroxene, orthopyroxene, and plagioclase has been determined using laser ablation-inductively coupled plasma-mass spectrometric (LA-ICP-MS) analysis of melt inclusions. Samples were selected from the 1988 eruption of White Island, New Zealand because petrographic evidence suggests that all three mineral phases are in equilibrium with the melt inclusions. All three phenocryst types are found as mineral inclusions within each of the other phases, and also often coexist with melt inclusions in growth-zone assemblages. Compositions of melt inclusions do not vary between the different host minerals, suggesting that boundary layer processes did not affect compositions of melt inclusions. Partition coefficients were calculated from the host and melt inclusion compositions and results were compared to literature values. Most partition coefficients overlap the wide range of values reported in the literature, but the White Island data are consistently at the lower end of published values. Results from the literature obtained using modern microanalytical techniques such as secondary ion mass spectrometry (SIMS) or proton induced x-ray emission (PIXE) also fall at the lower end of the published values. Rapid crystal growth-rates, crystal zonation, or the presence of accessory mineral inclusions in phenocrysts likely accounts for the wide range and generally higher partition coefficients reported in the literature. The data from this study were tested using the crystal lattice strain model (LSM) of Blundy & Wood (1994) and are consistent with that model for 3+ cations in clinopyroxene. The results of this study support previous studies that have documented that the melt inclusion-mineral (MIM) technique as a reliable method for determining partition coefficients, as long as the melt

inclusions have not experienced post-entrapment reequilibration.

1. Introduction

During the generation and crystallization of silicate melts, most elements are distributed unevenly between the melt phase and the crystallizing minerals. Partition coefficients describe the manner in which elements are distributed between different phases and are defined as:

$$K_d = C_{crystal} / C_{melt} \quad (1)$$

where K_d is the partition coefficient, $C_{crystal}$ is the concentration of an element in the crystal, and C_{melt} is the concentration of the same element in the silicate melt from which the mineral is precipitating. Reliable values for partition coefficients for a wide range of minerals and silicate melt compositions are necessary to understand and model igneous processes such as crystal fractionation, partial melting, and assimilation (e.g., GAST, 1968; PEARCE and CANN, 1973; ZIELINSKI and FREY, 1970). Trace elements including large-ion lithophile elements (LILE), high-field strength elements (HFSE) and rare earth elements (REE) that exhibit a wide variation in geochemical behavior and have a wide range of abundances in natural samples are especially useful to understand and constrain these igneous processes.

One method used to determine the distribution of trace elements between melt and minerals involves analysis of phenocrysts and the surrounding glassy matrix. Such studies include the pioneering work of Onuma et al. (1968), Schnetzler and Philpotts (1970), Hart and Brooks (1974), and continue to more recent studies by Irving and Frey (1984), Ewart and Griffin (1994), Thompson and Malpas (2000), and Norman et al. (2005). An alternative technique to determine the distribution of trace elements between melt and minerals involves experimental studies using either natural glasses (i.e., HART and DUNN, 1993), natural glasses doped with trace elements (i.e., ADAM and GREEN, 1994; ADAM et al., 1993), or simple synthetic compositions such as diopside-albite-anorthite-water doped with trace elements (i.e., SHIMIZU, 1974; ZIELINSKI and FREY, 1974). Both methods have been used to determine partition coefficients for a variety of magma compositions, producing a wide range of values for a given melt compositions

(i.e., basalt). This variability in turn results in a wide range of inferred melt compositions based on analyses of phenocrysts.

Recently, a new method referred to as the melt inclusion-mineral (MIM) technique has been introduced to determine partitioning behavior (LU et al., 1992; SOBOLEV et al., 1996; THOMAS et al., 2002). With this technique, the trace element compositions of melt inclusions and the immediately adjacent host crystal are analyzed and this information is used to calculate partition coefficients. It has only become possible to apply this technique in recent years as a result of the introduction of microanalytical techniques such as SIMS and LA-ICP-MS that offer spatial resolutions on the order of 10 μm and highly accurate analytical results. The MIM technique has the advantage that the crystals are natural and from melts with natural trace element abundances. Moreover, the melt in the inclusion can be assumed to represent a sample of the melt phase from which the immediately adjacent host crystal was precipitating. In this study the abundances of LILE, HFSE, and REE in plagioclase, clinopyroxene, orthopyroxene, and glassy melt inclusions were determined and the data used to calculate partition coefficients.

2. Geologic Background

Samples used in this study were collected from a recent (1988) eruption at White Island, New Zealand. White Island is an active andesitic-dacitic volcano located in the Bay of Plenty at the northern end of the Taupo Volcanic Zone (TVZ) on the North Island (COLE and NAIRN, 1975). Volcanoes located within the 250 km long TVZ range from basaltic to rhyolitic in composition. The North Island of New Zealand is part of the active boundary where the Pacific plate is being subducted beneath the Australian plate (ISACKS et al., 1968). White Island has been volcanically active for at least 10,000 years based on sediment analyses and hydrothermal activity (GIGGENBACH and GLASBY, 1977). Maori legends and European explorers have documented volcanic activity for at least several hundred years, and modern crater building eruptions occurred in 1933, 1947, 1965-1966, 1968, 1971, 1976-1982, and 1986-1992 (HOUGTON and NAIRN, 1991; WOOD and BROWNE, 1996). The most recent activity (1976-1982 and 1986-1992) is associated with

the emplacement of a large body of basaltic andesite magma at about 0.5 km depth, and the volcanic activity alternates between strombolian and phreatomagmatic eruptive styles (CLARK and COLE, 1989; HOUGTON and NAIRN, 1991; WOOD and BROWNE, 1996). Samples used in this study were collected by Dr. C. Peter Wood of the Institute of Geological and Nuclear Sciences, Wairakei, New Zealand and the samples from the 1988 eruption were used for this study.

3. Methodology

3.1 Mineral and melt inclusion petrography

Samples from the 1988 eruption at White Island consist of vesicular, porphyritic, gray andesite-dacite containing phenocrysts of plagioclase, clinopyroxene, and orthopyroxene in a glassy matrix that contains microlites of the same minerals and magnetite (RAPIEN et al., 2003). Crystals were separated from the surrounding matrix by crushing in a mortar. Phenocrysts are euhedral to subhedral and range from 0.01-1 mm in size. Phenocrysts are optically homogeneous but some evidence of chemical zoning is evidenced during microscopic examination of plagioclase crystals after etching in fluoboric acid (RAPIEN, 1998).

Phenocrysts contain both mineral and melt inclusions (Fig. 1). All three phenocryst phases can be found as inclusions in the other two phases (i.e. orthopyroxene inclusions in plagioclase and clinopyroxene phenocrysts, etc.). Mineral and melt inclusions display similar sizes and shapes and are often difficult to distinguish using optical microscopy. Both mineral and melt inclusions occur as isolated inclusions or in assemblages defining crystal growth zones. Figure 1 shows well-defined growth zones within an orthopyroxene phenocryst that contains both plagioclase and melt inclusions within the same growth zone. Coexisting mineral and melt inclusions in the same growth zone suggest contemporaneous crystallization of the host phase and the mineral inclusions at the time the melt was being trapped to form melt inclusions. This occurrences provides good evidence for equilibrium between the mineral phases and the silicate melt. Mineral and melt inclusions vary in size from <10 μm to >100 μm, however

most inclusions are typically 5-20 μm. Typically, isolated inclusions are larger than those in well-defined crystal growth assemblages. Melt inclusions are composed of homogeneous glass with or without a small bubble, but without any trapped or daughter minerals. Melt inclusion shape is rounded to elongate. The melt inclusions are assumed to be primary because they are trapped along crystal growth faces or between growth zones with no visible fractures. Samples from the 1988 eruption were selected for this study because they contain the most abundant and largest glassy melt inclusions.

3.2 Analytical techniques

Phenocrysts containing melt inclusions were mounted in epoxy, and the melt inclusions were brought closer to the surface of the crystal by continued grinding and polishing by hand on glass plates for better visual inspection. Melt inclusions located along fractures or near the edges of crystals were ignored as were those containing a shrinkage or vapor bubble. Some inclusions were exposed at the surface for compositional analysis while others remained beneath the crystal surface and were analyzed by first removing the overlying host by laser ablation, as described below. The major and minor element compositions (Si, Mg, Ca, Fe, Na, K, Mn, P, and Ti) of exposed melt inclusions were determined using an Cameca SX-50 electron microprobe (EPMA) at Virginia Tech. For melt inclusion analyses, an accelerating voltage of 15 kV was used with a beam current of 5 nA and beam diameter of <5 μm. These analytical conditions and analyzing Na and K first minimizes volatilization (STUDENT and BODNAR, 1999). Host (plagioclase, clinopyroxene, and orthopyroxene) analyses were conducted at an accelerating voltage of 15 kV, a beam current of 20 nA, and beam diameter of about 1 μm. Precision of major element data is approximately 2% relative, and minor element precision is approximately 5% relative based upon multiple previous analyses.

Major, minor, and trace element compositions of minerals and melt inclusions were determined by laser-ablation inductively-coupled plasma mass-spectrometry (LA-ICP-MS) using procedures similar to those outlined by Heinrich et al. (2003). All melt inclusions analyzed in this study were exposed at the surface either by hand or by ablating the host overlying the melt inclusion as described below prior to analysis

eliminating the need to make a host correction. The major and minor element composition of some crystals and melt inclusions were also determined by electron microprobe for comparison with the LA-ICP-MS data. Analyses were conducted at Virginia Tech using an Agilent 7500ce quadrupole ICPMS and a 193 nm GeoLas Pro excimer laser ablation system. NIST 610 glass was analyzed two times before and after each analytical session that included 15-20 inclusions and was used as the standard for data reduction and for drift correction. Analyses of the NIST glass were conducted using laser settings of 27 kV, 150 mJ, with a pulse rate of 15 Hz. Melt inclusion and host analyses were conducted at the same conditions except a pulse rate of 5 Hz was used to improve signal stability.

For each LA-ICP-MS analysis, background signal was collected for approximately 30 seconds before the laser was turned on to begin to ablate the melt inclusion or host. Analyses of the host phase were made by placing the laser spot completely in the host mineral and as close to the melt inclusion/host boundary as possible. For melt inclusions, the laser spot size was adjusted such that the entire spot was within the melt inclusion. The ablation process was continued until the ablation pit traversed from the melt inclusion into the underlying host crystal, at which point the laser was turned off and the signal was collected until intensities returned to background levels (Fig. 2). The initial portion of each melt inclusion analysis was not included in data reduction to avoid possible errors from contamination on the sample surface from airborne particles or previously ablated material deposited onto the surface.

Some inclusions were exposed at the surface by hand polishing while other melt inclusions remained covered by ≤100 μm of the host phase. Inclusions beneath the crystal surface were exposed using the laser ablation system with a laser pulse rate of 5 Hz, a laser spot size significantly larger than the melt inclusion (>45 μm). This technique was used to remove all host material between the surface and the inclusion so that the subsequent analysis will include only material from the melt inclusion and not from the host. To expose the melt inclusion, the laser was fired 5 or 10 times and the inclusion was then examined optically. If the inclusion was not exposed at the center of the laser crater, then another sequence of 5 to 10 laser pulses was applied and the inclusion re-examined. This process was repeated until the melt inclusion was exposed and clearly visible at the

center of the ablation crater. After the signal returned to background level, the melt inclusion was analyzed after adjusting the laser to the largest spot size that would fit within the inclusion. The analytical conditions for the host mineral and melt inclusions were the same, except that the minerals were analyzed for 20-30 seconds at each spot. Three or four analyses in the host mineral around the melt inclusion were conducted to test for homogeneity in the host mineral composition. Several areas were analyzed by both EPMA and LA-ICP-MS to test for consistency between the two techniques. The time-resolved signals were analyzed using AMS analytical software (MUTCHLER et al., 2007).

4. Results

4.1 Mineral compositions

Major element compositions of host crystals are shown in Figures 3a (pyroxene) and 3b (plagioclase), and listed in Table 1. Also shown on Figure 3a and 3b are the results from Rapien et al. (2003). Clinopyroxenes are augites with an average composition of $En_{47}Fs_{13}Wo_{40}$. Orthopyroxenes have an average composition of $En_{71}Fs_{27}Wo_{2}$. Plagioclase compositions are slightly more Ca-rich than the samples analyzed by Rapien et al. (2003) and have an average composition of $An_{80}Ab_{18}Or_{2}$.

Trace element data for the minerals is summarized in Figure 4. Plagioclase is enriched in LREE and has a strong positive Eu anomaly. Clinopyroxene has a concave–down REE pattern, with middle REE slightly enriched over both LREE and HREE. Orthopyroxene is relatively enriched in HREE (Fig. 4a). Plagioclase is enriched in LILE elements and depleted in HFSE with respect to both pyroxenes (Fig. 4b). These patterns for trace elements are typical for these minerals (i.e., BACON, 1990).

4.2 Melt compositions

Average melt inclusion compositions from the three different phenocrysts determined using EPMA and LA-ICP-MS are listed in Table 2. Melt inclusion

compositions from all three phenocrysts are identical within experimental error, confirming that all three mineral phases were co-precipitating from the same melt (RAPIEN, 1998; WARDELL et al., 2001). In terms of major element chemistry, the melt inclusions resemble typical calc-alkaline dacites (Fig. 5).

The most striking aspect of the trace element chemistry of the melt inclusions is their uniformity. Despite being hosted in minerals with a wide range in trace element chemistry (i.e. Fig. 4), the trace element compositions of the melt inclusions are, within analytical error, identical (Fig. 6). The melt inclusions are slightly enriched in LREE, have a small negative Eu anomaly, and have a flat chondrite-normalized pattern for HREE. High field-strength elements, especially Nb and Ti are relatively low, while Ba is elevated. Negative anomalies in Sr, Eu and (possibly) Pb probably reflect plagioclase fractionation. Otherwise, the trace element characteristics of the melt inclusions are typical of arc magmas (i.e., BACON, 1990).

4.3 Partition coefficients

Partition coefficients (K_d) were calculated from individual melt inclusion-host crystal pairs. Data for individual analysis are available as supplemental material online. The average partition coefficients for the three different White Island phenocryst-melt pairs, and partitioning data for pyroxene and plagioclase in andesite, dacite, and low-Si rhyolite from published literature are listed in Table 3 and summarized on Figure 7 (BACON and DRUITT, 1988; DUNN and SEN, 1994; EWART et al., 1973; EWART and GRIFFIN, 1994; FORSYTHE et al., 1994; FUJIMAKI et al., 1984; GREEN and PEARSON, 1983; LUHR and CARMICHAEL, 1980; NASH and CRECRAFT, 1985; OKAMOTO, 1979; PHILPOTTS and SCHNETZLER, 1970; SCHNETZLER and PHILPOTTS, 1970). For most trace elements, the White Island partition coefficient data coincides with lower range of literature K_d values (Fig. 7).

The relationship between partitioning behavior for trace elements and ionic radii (SHANNON, 1976) was determined following the method of Onuma et al. (1966) and results are plotted in Figures 8-10, for plagioclase, orthopyroxene, and clinopyroxene, respectively. The Onuma plots display the predicted parabolic shape for 2+ cations for all

three mineral phases and also display a parabolic shape for 3+ cations in clinopyroxene. Because of the limited size range of cations analyzed here, 3+ cations for orthopyroxene and plagioclase plot as half-parabolas. The apex of these parabolas has been predicted to lie at an ionic radii slightly larger than La for plagioclase (AIGNER-TORRES et al., 2007) and at approximately the ionic radius of Lu for orthopyroxene (NORMAN et al., 2005; SCHWANDT and MCKAY, 1998). This is consistent with the White Island K_d data for plagioclase and orthopyroxene. Additional information on the nature of trace element substitution can be found in Appendix 1. The data for the 3+ cation series for clinopyroxene were fitted using a parabolic regression model according to the model developed by Brice (1975) and modified by Blundy and Wood (1994) and Wood and Blundy (1997). The temperature used in the modified Brice equation (1373 K) is based upon the homogenization temperatures of White Island melt inclusions (RAPIEN et al., 2003) and the two-pyroxene geothermobarometer (LINDSLEY, 1983; RAPIEN et al., 2003).

5. Discussion

5.1 MIM technique

The three principal criticisms of the MIM technique for determining partition coefficients are: 1) the possibility of contamination by the host mineral; 2) post-entrapment crystallization and fractionation of the melt; 3) post-entrapment exchange of Fe and Mg in mafic minerals and; 4) the possibility that a substantial portion of the inclusion represents a disequilibrium boundary layer. Simply put, because White Island melt inclusions in pyroxene and plagioclase are effectively identical in composition, none of problems are evident in this study. For example, MgO in plagioclase-hosted inclusions is neither higher nor lower than in pyroxene-hosted inclusions. If pyroxene had contaminated the melt analyses, MgO in pyroxene MI should be higher than MgO in plagioclase MI, while if the inclusion had fractionated during pyroxene growth, MgO should be lower than in plagioclase. Similar arguments can be made for Sr and Al_2O_3 in plagioclase and for CaO in both plagioclase and clinopyroxene. Post-entrapment crystallization of the host on the walls of the melt inclusion appears to be primarily

restricted to inclusions that have either cooled slowly and are not glassy in nature (DANYUSHEVSKY et al., 2000; DANYUSHEVSKY et al., 2002; GAETANI and WATSON, 2000). Because the White Island MI were rapidly cooled during an explosive eruption and did not require any re-homogenization, crystallization of the mineral host on the inclusion walls is unlikely to be an issue. Diffusive exchange of Fe, Ti, and Si between melt inclusions and the host has been suggested based upon compositional differences between melt inclusions hosted in different phases from the same sample (DANYUSHEVSKY et al., 2002). However, this process does not seem to be significant for this study as the melt inclusion composition is the same regardless of the host phase.

The lack of correlation between MI chemistry and host mineralogy also presents strong arguments against the existence of an extensive boundary layer in the MI. Boundary layers may develop when the crystal growth rate is faster than the diffusion rates of cations in a melt (BACON, 1989). The result of boundary layer development will be that the area immediately surrounding the crystal will become enriched in incompatible elements that are unable to diffuse away from the crystal faster than the crystal growth rate, and that same area will become depleted in compatible elements that cannot diffuse to the growing crystal surface faster than they are being removed by crystal growth. The effect a boundary layer on partition coefficients is that incompatible elements would appear to be more incompatible than they actually are, while compatible elements will seem to be more compatible than they would be without the presence of a boundary layer. Proving whether boundary layer processes have affect melt inclusion compositions is difficult, if not impossible, if melt inclusions in only one host phase are examined. However, if two or more minerals are co-precipitating from the same melt, as is the case in this study, it is possible to determine if the melt inclusion compositions have been affected by boundary layer processes based on the analytical results. If boundary layers affected melt inclusion compositions the inclusion chemistry should vary based on the host phase such that concentrations of elements that are compatible in one mineral and incompatible in another mineral should be significantly different. For example, Sr is compatible in plagioclase and incompatible in pyroxenes. If melt inclusion compositions were affected by the development of a boundary layer, then plagioclase-hosted MI should be depleted in Sr compared to pyroxene-hosted MI. Analytical data for

Sr (and all other measured elements) show similar compositions in all host phases (Table 2; Fig. 6), suggesting that boundary layers did not affect the compositions of melt inclusions in this study. Boundary layer processes should have a greater effect on compositions of small inclusions compared to larger inclusions and several workers have suggested boundary layer effects only become important for inclusions smaller than 25 μm (ANDERSON, 1974; LOWENSTERN, 1995; LU et al., 1995). Melt inclusions used in this study were all larger than 15 μm, so most inclusions analyzed for this study should not show this effect.

5.2 Comparison of this study with published values

The partitioning data from this study are generally consistent with the compatibility trends previously determined for these three different mineral phases. All measured trace elements are incompatible in orthopyroxene. Sr is the only element that is compatible in plagioclase. The relatively high compatibility for Eu with respect to other REE in plagioclase reflects the partial reduction of Eu^{3+} to Eu^{2+}, with the divalent cation being nearly as compatible in plagioclase as Sr (AIGNER-TORRES et al., 2007). Many transition metal elements (Sc, V, Mn, and Y) are compatible, and the MREE, HREE, and Ti are only slightly incompatible in clinopyroxene. Most of the partition coefficients from this study are within the wide range of values reported in the literature but fall at the lower end of the range of the published values. The observation that partition coefficients determined in this study consistently lie at the lower end of the range in K_d reported in the literature may be explained in several ways.

Most of available partition coefficient data for intermediate to silicic rocks is based on chemical analysis of glass and mineral separates using bulk analytical techniques (BACON and DRUITT, 1988; EWART et al., 1973; FUJIMAKI et al., 1984; LUHR and CARMICHAEL, 1980; NASH and CRECRAFT, 1985; OKAMOTO, 1979; PHILPOTTS and SCHNETZLER, 1970; SCHNETZLER and PHILPOTTS, 1970).This method, which is no longer employed, faced many problems. First, complete separation of phenocrysts from the matrix is difficult at best. An additional limitation of the phenocryst/matrix technique is that only the outermost portion of the phenocryst can be assumed to be in equilibrium

with the surrounding melt phase, and if the crystal is zoned, an erroneous value for the partition coefficient will be obtained (ALBAREDE and BOTTINGA, 1972). Perhaps the most significant problem with the older phenocryst-matrix data is the likely presence of included accessory phases and glass within the phenocryst (MICHAEL, 1988; SISSON, 1991). Phases such as allanite, monazite, zircon, sphene, ilmenite, or alkali feldspar, when present as inclusions, will all tend to give false high values for the incompatible trace element content of the phenocryst phase. This results in erroneously high K_d values for incompatible elements. Additional information on the effect of mineral inclusions on the partition coefficient can be found in Appendix 1. Thomas et al. (2002) suggested this process to explain differences between K_d obtained in their study using the MIM technique and the published values. Modern analytical techniques with excellent spatial resolution allow inclusions to be avoided during analysis and eliminate this problem, but the majority of data in the literature for intermediate-felsic composition magmas is from earlier studies that did not have access to these modern microanalytical techniques.

Early experimental studies to investigate trace element partitioning used samples with trace element concentrations significantly higher than natural levels in facilitate analysis using EPMA. These unnaturally elevated trace element concentrations raise questions about the applicability of Henry's Law behavior to interpret the experimental results (DRAKE and HOLLOWAY, 1978). Today, the need to use unnaturally elevated trace element concentrations in experimental studies has been reduced owing to the availability of microanalytical techniques such as SIMS, LA-ICP-MS, PIXE, SXRF, and others that offer good spatial resolution and ppb to ppm detection limits, but questions remain concerning the results of doped studies (FORSYTHE et al., 1994). REE doping of experimental samples increases the partition coefficients of REE and Y by 30-100% than the partition coefficient derived from undoped samples (BINDEMAN and DAVIS, 2000). Another concern related to experimental studies is related to the duration of the experiments, which last from a few hours to a few weeks, and results in extremely rapid crystal growth rates. Several authors have shown that rapid growth rates can produce zoned crystals (BOTTINGA et al., 1966; KOUCHI et al., 1983; TSUCHIYAMA, 1985), and non-equilibrium distribution of trace elements between phases (ALBAREDE and BOTTINGA, 1972; HENDERSON and WILLIAMS, 1979; TSUCHIYAMA, 1985).

Recent phenocryst-matrix studies have utilized proton-induced x-ray emission (PIXE) (EWART and GRIFFIN, 1994) and secondary ion-mass spectrometry (SIMS) (DUNN and SEN, 1994) to measure partition coefficients. These techniques allow mineral or melt inclusions to be avoided during the host analysis, and can also allow compositional zonation within phenocrysts to be identified and the chemistry of those zones determined. However, these analyses cannot conclusively prove contemporaneity between phenocrysts and the immediately surrounding matrix glass. For this reason, use of the MIM technique with glassy melt inclusions represents an improvement in our ability to determine partitioning behavior.

Comparison of the results of this study (Table 4; Fig. 7) to the three most recent studies (DUNN and SEN, 1994; EWART and GRIFFIN, 1994; FORSYTHE et al., 1994) shows that there is good agreement on the partition coefficients between these four studies. For example, the partition coefficients for REE are nearly identical to the data from Dunn and Sen (1994). There is a slightly larger range for the LILE and HFSE than for REE because the data from those studies ranges from andesite to low-Si rhyolite (EWART and GRIFFIN, 1994). The partition coefficients of Forsythe et al. (1994) for HFSE in clinopyroxene are very close to those from this study and are also similar to the results of Ewart and Griffin (1994), suggesting that even though this study used doped experiments, the results followed Henry's Law behavior and reflects inherent differences in the substitution of HFSE compared to REE in the crystal lattice (BINDEMAN and DAVIS, 2000). All of this data suggest that the MIM technique produces similar results to those from either phenocryst-matrix or experimental studies.

Blundy and Wood (1994) and Wood and Blundy (1997) presented a model based on the modified Brice equation (BRICE, 1975) that describes how trace element substitution in minerals can be represented by a strain in the crystal lattice (Lattice Strain Model – LSM). The LSM relates the partition coefficient of and element i (D_i), with a radius r_i, to the partition coefficient of an element o (D_o) that has an ionic radius r_o equal to the ideal size of the crystallographic site of interest:

$$D_i = D_o \exp \frac{-4\pi E \left[\frac{r_o}{2}(r_i - r_o)^2 + \frac{1}{3}(r_i - r_o)^3\right]}{RT} \quad (2)$$

In Equation (2), E is the Young's Modulus of the site of interest, N_A is Avogadro's number, R is the gas constant, and T is temperature in K. The values of r_o, D_o, and E are obtained by fitting a parabolic equation to the experimentally measured homovalent cation series. Table 5 shows the results of the LSM model for 3+ cations in clinopyroxene. Other cation series and those for plagioclase and orthopyroxene were not modeled because of insufficient data, multiple oxidation states, or other complications. The values obtained by modeling the White Island partition coefficients are similar to literature values (Table 5).

6. Summary

The melt inclusion-mineral technique proposed by Thomas et al. (2002) has been applied to determine partition coefficients for Ti, Mn, Sr, Y, Zr, Nb, Ba, La, Nd, Sm, Eu, Gd, Dy, Ho, Yb, Hf, and Pb between clinopyroxene, orthopyroxene, plagioclase and dacitic melt using laser ablation-inductively coupled plasma-mass spectrometry. Samples from a recent eruption of White Island, New Zealand contain clinopyroxene, orthopyroxene, and plagioclase that were all co-precipitating from a melt of the same composition and trapped this melt as melt inclusions. Compositions of melt inclusions do not vary with host phase indicated that boundary layer and post-entrapment processes have not affected the melt inclusion compositions. All trace elements examined in this study are incompatible in plagioclase except Sr, and all measured trace elements are incompatible in orthopyroxene except for Mn. In clinopyroxene, Sc, V, Mn, Y, and the HREE are all compatible, and Ti and the MREE are only slightly incompatible. Results of this study are consistent with partition coefficients reported in the literature, but our values typically lie at the lower end of the range of published values. These differences are thought to be due to artificial-crystal growth rates that are too fast and unnaturally elevated trace element concentrations in the melt for experimental studies and either the presence of crystal zonation or mineral inclusions in natural phenocryst-matrix studies. The partitioning data for 3+ cations in clinopyroxene is consistent with the crystal lattice strain model derived by Blundy & Wood (1994).

Acknowledgements

The authors thank C. Loehn and R. Tracy for assistance with EPMA analyses of the samples, and S. Becker, C. Cannatelli, and A. Fall for critical comments on the manuscript. Funding was provided by the Cunningham Fellowship from Virginia Tech to MJS and NSF grants EAR-0337094 and EAR-0322119 to RJB.

References:

Adam J. and Green T. H. (1994) The effects of pressure and temperature on the partitioning of Ti, Sr, and REE between amphibole, clinopyroxene and basanitic melts. *Chemical Geology* **117**, 219-233.

Adam J., Green T. H., and Sie S. H. (1993) Proton microprobe determined partitioning of Rb, Sr, Ba, Y, Zr, Nb and Ta between experimentally produced amphiboles and silicate melts with variable F content. *Chemical Geology* **109**, 29-49.

Aigner-Torres M., Blundy J., Ulmer P., and Pettke T. (2007) Laser ablation ICPMS study of trace element partitioning between plagioclase and basaltic melts: An experimental approach. *Contributions to Mineralogy and Petrology* **153**, 647-667.

Albarede F. and Bottinga Y. (1972) Kinetic disequilibrium in trace element partitioning between phenocrysts and host lava. *Geochimica et Cosmochimica Acta* **36**, 141-156.

Anderson A. T. J. (1974) Evidence for a picritic, volatile-rich magma beneath Mt. Shasta, California. *Journal of Petrology* **15**, 243-267.

Bacon C. R. (1989) Crystallization of accessory phases in magma by local saturation adjacent to phenocrysts. *Geochimica et Cosmochimica Acta* **53**, 1055-1066.

Bacon C. R. (1990) Calc-alkaline, shoshonitic, and primitive tholeiitic lavas from monogenetic volcanoes near Crater Lake, Oregon. *Journal of Petrology* **31**(1), 135-166.

Bacon C. R. and Druitt T. H. (1988) Compositional evolution of the zoned calcalkaline magma chamber of Mount Mazama, Crater Lake, Oregon. *Contributions to Mineralogy and Petrology* **98**, 224-256.

Bindeman I. N. and Davis A. M. (2000) Trace element partitioning between plagioclase and melt: Investigation of dopant influence on partition behavior. *Geochimica et Cosmochimica Acta* **64**(16), 2863-2878.

Bottinga Y., Kudo A., and Weill D. (1966) Some observations on oscillatory zoning and crystallization of magmatic plagioclase. *American Mineralogist* **51**, 792-806.

Brice J. C. (1975) Some thermodynamic aspects of the growth of strained crystals. *Journal of Crystal Growth* **28**, 249-253.

Clark R. H. and Cole J. W. (1989) Volcanic monitoring and surveillance at White Island before the 1976-1982 eruption sequence. In *The 1976-1982 eruption sequence at White Island volcano (Whakaari), Bay of Plenty, New Zealand*, Vol. 103 (ed. B. F. Houghton and I. A. Nairn), pp. 9-11. New Zealand Geological Survey.

Cole J. W. and Nairn I. A. (1975) Part 22: New Zealand. In *Catalogue of the active volcanoes of the world including Solfatara fields* (ed. I. A. o. V. a. C. o. t. E. s. Interior).

Danyushevsky L. V., Della-Pasqua F. N., and Sokolov S. (2000) Re-equilibration of melt inclusions trapped by magnesian olivine phenocrysts from subduction-related magmas: Petrological implications. *Contributions to Mineralogy and Petrology* **138**, 68-83.

Danyushevsky L. V., McNeill A. W., and Sobolev A. V. (2002) Experimental and petrological studies of melt inclusions in phenocrysts from mantle-derived magams: an overview of techniques, advantages and complications. *Chemical Geology* **183**, 5-24.

Drake M. J. and Holloway J. R. (1978) "Henry's Law" behavior of Sm in a natural plagioclase/melt system: Importance of experimental procedure. *Geochimica et Cosmochimica Acta* **42**, 679-683.

Dunn T. and Sen C. (1994) Mineral/matrix partition coefficients for orthopyroxene, plagioclase, and olivine in basaltic to andesitic systems: A combined analytical and experimental study. *Geochimica et Cosmochimica Acta* **58**(2), 717-733.

Ewart A., Bryan W. B., and Gill J. B. (1973) Mineralogy and geochemistry of the younger volcanic islands of Tonga, S.W. Pacific. *Journal of Petrology* **14**(3), 429-465.

Ewart A. and Griffin W. L. (1994) Application of proton-microprobe data to trace-element partitioning in volcanic rocks. *Chemical Geology* **117**, 251-284.

Forsythe L. M., Nielsen R. L., and Fisk M. R. (1994) High-field strength element partitioning between pyroxene and basaltic to dacitic magmas. *Chemical Geology* **117**, 107-125.

Fujimaki H., Tatsumoto M., and Aoki K.-i. (1984) Partition coefficients of Hf, Zr, and REE between phenocrysts and groundmasses. *Journal of Geophysical Research* **89**, B662-672.

Gaetani G. A. and Watson E. B. (2000) Open system behavior of olivine-hosted melt inclusions. *Earth and Planetary Science Letters* **183**, 27-41.

Gast P. W. (1968) Trace element fractionation and origin of tholeiitic and alkaline magma types. *Geochimica et Cosmochimica Acta* **32**, 1057-1086.

Giggenbach W. F. and Glasby C. (1977) The influence of thermal activity on the trace metal distribution in marine sediments around White Island, New Zealand. *New Zealand Department of Science and Industry Research Bulletin* **218**, 121-126.

Green T. H. and Pearson N. J. (1983) Effect of pressure on rare earth element partition coefficients in common magmas. *Nature* **305**, 414-416.

Hart S. R. and Dunn T. (1993) Experimental cpx/melt partitioning of 24 trace elements. *Contributions to Mineralogy and Petrology* **113**, 1-8.

Henderson P. and Williams C. T. (1979) Variation in trace element partition (crystal/magma) as a function of crystal growth rate. *Physics and Chemistry of the Earth* **11**, 191-198.

Hougton B. F. and Nairn I. A. (1991) The 1976-1982 Strombolian and phreatomagmatic eruptions of White Island, New Zealand: Eruptive and depositional mechanisms at a "wet" volcano. *Bulletin of Volcanology* **54**, 25-49.

Isacks B., Oliver J., and Sykes L. R. (1968) Seismology and the new global tectonics. *Journal of Geophysical Research* **73**, 5585-5899.

Kouchi A., Sugawara Y., Kashima K., and Sinagawa I. (1983) Laboratory growth of sector zoned clinopyroxenes in the system $CaMgSi_2O_6$ - $CaTiAl_2O_6$. *Contributions to Mineralogy and Petrology* **83**, 177-184.

Lindsley D. H. (1983) Pyroxene thermometry. *American Mineralogist* **68**, 477-493.

Lowenstern J. B. (1995) Applications of silicate-melt inclusions to the study of magmatic volatiles. In *Magmas, Fluid and Ore Deposits*, Vol. 23 (ed. J. F. H. Thompson), pp. 71-99. Mineralogical Association of Canada.

Lu F., Anderson A. T., and Davis A. M. (1992) New and larger sanidine/melt partition coefficients for Ba and Sr as determined by ion microprobe analyses of melt

inclusions and their sanidine host crystals. *Geolocial Society of America Abstracts with Programs* **24**, A44.
Lu F., Anderson A. T., and Davis A. M. (1995) Diffusional gradients at the crystal/metl interface and their effect on the composition of melt inclusions. *Journal of Geology* **103**, 591-597.
Luhr J. F. and Carmichael I. S. E. (1980) The Colima Volcanic Complex, Mexico: I. Post-caldera andesites from Volcan Colima. *Contributions to Mineralogy and Petrology* **71**, 343-372.
Michael P. J. (1988) Partition coefficients for rare earth elements in mafic minerals of high silica rhyolites: The importance of accessory mineral inclusions. *Geochimica et Cosmochimica Acta* **52**, 275-282.
Mutchler S. R., Fedele L., and Bodnar R. J. (2007) AMS a new software package for reduction of Laser Ablation ICPMS data. *ECROFI XIX*.
Nash W. P. and Crecraft H. R. (1985) Partition coefficients for trace elements in silicic magmas. *Geochimica et Cosmochimica Acta* **49**, 2309-2322.
Norman M., Garcia M. O., and Pietruszka A. J. (2005) Trace-element distribution coefficients for pyroxenes, plagioclase, and olivine in evolved tholeiites from the 1955 eruption of Kilauea Volcano, Hawai'i, and petrogenesis of differentiated rift-zone lavas. *American Mineralogist* **90**, 888-899.
Okamoto K. (1979) Geochemical study on magmatic differentiation of Asama Volcano, Central Japan. *Journal of the Geological Society of Japan* **85**(8), 525-535.
Pearce J. A. and Cann J. R. (1973) Tectonic setting of basic volcanic rocks determined using trace element analyses. *Earth and Planetary Sciences Letters* **19**, 290-300.
Philpotts J. A. and Schnetzler C. C. (1970) Phenocryst-matrix partition coefficients for K, Rb, Sr and Ba, with applications to anorthosite and basalt genesis. *Geochimica et Cosmochimica Acta* **34**, 307-322.
Rapien M. H. (1998) Geochemical evolution at White Island, New Zealand. Masters, Virginia Polytechnical Institute and State University.
Rapien M. H., Bodnar R. J., Simmons S. F., Szabo C. S., Wood C. P., and Sutton S. R. (2003) Melt inclusion study of the embryonic porphyry copper system at White Island, New Zealand. *Society of Economic Geologists Special Publication* **10**, 41-59.
Schnetzler C. C. and Philpotts J. A. (1970) Partition coefficients of rare-earth elements between igneous matrix material and rock-forming mineral phenocrysts - II. *Geochimica et Cosmochimica Acta* **34**, 331-340.
Schwandt C. S. and McKay G. A. (1998) Rare earth element partition coefficients from enstatite/melt synthesis experiments. *Geochimica et Cosmochimica Acta* **62**(16), 2845-2848.
Shannon R. D. (1976) Revised effective ionic radii and systematic studies of interatomic distances in halides and chalcogenides. *Acta Crystallographica* **A32**, 751-767.
Shimizu N. (1974) An experimental study of the partitioning of K, Rb, Cs, Sr, and Ba between clinopyroxene and liquid at high pressures. *Geochimica et Cosmochimica Acta* **38**, 1789-1798.
Sisson T. W. (1991) Pyroxene-high silica rhyolite trace element partition coefficients measured by ion microprobe. *Geochimica et Cosmochimica Acta* **55**(55).

Sobolev A. V., Migdisov A. A., and Portnyagin M. V. (1996) Incompatible element partitioning between clinopyroxenes and basaltic liquid revealed by study of melt inclusions in minerals from Troodos Lavas, Cyprus. *Petrology* **4**, 307-317.

Student J. J. and Bodnar R. J. (1999) Synthetic fluid inclusions XIV: Coexisting silicate melt and aqueous fluid inclusions in the haplogranite-H_2O-NaCl-KCl system. *Journal of Petrology* **40**(10), 1509-1525.

Thomas J. B., Bodnar R. J., Shimizu N., and Sinha A. K. (2002) Determination of zircon/melt trace element partition coefficients from SIMS analysis of melt inclusions in zircon. *Geochimica et Cosmochimica Acta* **66**(16), 2887-2901.

Tsuchiyama A. (1985) Crystallization kinetics in the system $CaMgSi_2O_6$ - $CaAl_2Si_2O_8$: Development of zoning and kinetics effects on element partitioning. *American Mineralogist* **70**, 474-486.

Wardell L. J., Kyle P. R., Dunbar N., and Christenson B. (2001) White Island volcano, New Zealand: Carbon dioxide and sulfur dioxide emission rates and melt inclusion studies. *Chemical Geology* **177**, 187-200.

Wood C. P. and Browne P. R. L. (1996) Chlorine-rich pyrometamorphic magma at White Island volcano, New Zealand. *Journal of Volcanology and Geothermal Research* **72**, 21-35.

Zielinski R. A. and Frey F. A. (1970) Gough Island: Evaluation of a fractional crystallization model. *Contributions to Mineralogy and Petrology* **29**, 242-254.

Zielinski R. A. and Frey F. A. (1974) An experimental study of a rare earth element in the system diopside/water. *Geochimica et Cosmochimica Acta* **38**, 545-565.

Tables

Table 1. Average major and trace element compositions of clinopyroxene, orthopyroxene, and plagioclase phenocrysts as determined using EPMA and LA-ICP-MS. Major elements are in wt% and trace elements are in ppm. Numbers in parentheses represents the number of analyses.

EPMA

	CPX (8)	Std Dev	OPX (3)	Std Dev	Plag (3)	Std Dev
Na_2O	0.26	0.06	0.12	0.08	3.49	0.20
MgO	16.15	0.73	24.86	0.40	0.19	0.02
Al_2O_3	2.11	0.30	1.38	0.25	28.46	0.19
SiO_2	52.69	0.25	54.32	0.27	52.98	0.58
K_2O	0.03	0.05	0.07	0.07	0.26	0.05
CaO	18.22	0.54	2.48	0.70	13.12	0.61
TiO_2	0.43	0.06	0.27	0.01	0.06	0.02
MnO	0.23	0.02	0.34	0.02	0.02	0.01
FeO	8.90	0.78	15.65	0.46	0.84	0.21
NiO	0.03	0.01	0.06	0.02	0.01	0.01
Total	99.05	0.40	99.56	0.19	99.44	0.53

LA-ICP-MS	CPX (9)	Std Dev	OPX (8)	Std Dev	Plag (5)	Std Dev
Na_2O	0.218	0.016	0.038	0.008	3.017	0.173
MgO	15.88	0.648	24.604	1.038	0.154	0.006
Al_2O_3	2.00	0.127	1.260	0.042	31.280	1.839
SiO_2	53.62	0.694	56.183	1.595	52.571	2.593
K_2O	0.01	0.005	0.007	0.007	0.213	0.015
CaO	18.51	1.206	1.870	0.085	12.006	0.910
TiO_2	0.38	0.060	0.226	0.014	0.047	0.006
MnO	0.23	0.032	0.334	0.019	0.004	0.001
FeO	8.98	1.377	15.465	0.713	0.639	0.025
Sr	12.30	0.78	0.47	0.20	349.40	22.74
Y	21.74	3.71	4.35	0.30	0.37	0.16
Zr	15.23	2.46	2.81	0.47	1.06	0.90
Nb	0.03	0.01	0.05	0.04	0.06	0.04
Ba	1.30	1.12	1.98	0.88	172.26	15.28
La	1.00	0.17	0.04	0.02	1.47	0.25
Nd	5.33	1.15	0.21	0.08	1.10	0.36
Sm	2.21	0.41	0.14	0.05	0.15	0.04
Eu	0.53	0.10	0.04	0.03	0.43	0.04
Gd	3.32	0.69	0.25	0.08	0.21	0.14
Dy	4.00	0.78	0.58	0.10	0.10	0.07
Ho	0.85	0.12	0.18	0.04	0.02	0.01
Yb	2.43	0.47	0.85	0.11	0.03	0.02
Hf	0.72	0.15	0.15	0.04	0.04	0.02
Pb	0.13	0.06	0.18	0.09	1.53	0.17

Table 2. Average major and trace element compositions of melt inclusions hosted in clinopyroxene, orthopyroxene and plagioclase as determined by EPMA and LA-ICP-MS analyses. Major elements are in wt% and trace elements are in ppm. Number in parentheses is the number of analyses.

EPMA

	CPX MI (7)	Std Dev	OPX MI (3)	Std Dev	Plag MI (5)	Std Dev
SiO_2	65.39	1.33	65.57	0.93	66.06	0.84
TiO_2	0.98	0.19	1.09	0.14	1.11	0.22
Al_2O_3	13.60	1.46	13.83	0.25	13.39	0.24
MgO	2.32	1.36	2.02	0.80	2.12	0.16
CaO	5.39	1.22	4.92	0.01	4.63	0.10
MnO	0.08	0.03	0.09	0.02	0.09	0.03
FeO	6.10	0.49	6.82	0.07	6.07	0.43
NiO	0.04	0.02	0.03	0.01	0.04	0.02
K_2O	1.81	0.46	1.96	0.61	2.05	0.06
Na_2O	2.48	0.15	2.64	0.17	2.94	0.04
Total	98.20	0.55	98.99	0.00	98.50	0.41

LA-ICP-MS	CPX MI (22)	Std Dev	OPX MI (27)	Std Dev	Plag MI (23)	Std Dev
Na_2O	2.61	0.17	2.77	0.22	3.00	0.13
MgO	1.66	0.39	1.79	0.63	1.88	0.15
Al_2O_3	15.96	1.55	16.29	1.68	15.90	1.46
SiO_2	65.44	2.37	64.98	2.70	65.28	1.68
K_2O	3.10	1.03	2.41	0.48	2.39	0.24
CaO	4.42	1.17	4.91	1.01	4.84	0.63
TiO_2	0.89	0.27	0.97	0.16	1.06	0.18
MnO	0.08	0.02	0.08	0.01	0.08	0.01
FeO	5.68	1.90	5.64	0.99	5.39	0.40
Sr	132.32	30.90	154.45	31.93	144.54	19.16
Y	23.43	9.97	27.09	5.39	28.66	5.98
Zr	164.62	31.22	180.16	44.28	220.21	53.17
Nb	5.69	1.79	5.52	1.36	6.85	2.08
Ba	996.25	186.36	908.98	98.12	909.47	89.85
La	13.07	3.50	14.86	3.04	16.30	2.68
Nd	14.51	5.81	17.44	9.85	18.12	3.56
Sm	3.92	1.93	4.15	1.79	4.33	1.01
Eu	0.92	0.30	0.97	0.57	1.05	0.21
Gd	3.79	1.85	4.76	2.21	4.51	1.14
Dy	4.45	1.58	4.66	1.63	5.07	1.13
Ho	0.89	0.33	0.97	0.58	1.04	0.25
Yb	2.60	0.99	2.67	0.77	3.41	0.81
Hf	4.84	2.12	5.07	1.15	5.59	1.71
Pb	10.95	1.89	11.41	2.30	11.91	1.38

Table 3. Average partition coefficients (KD) calculated using the individual melt inclusion-host pairs that were used to calculate the average values found in Tables 1 and 2. Also shown are data from twelve other studies for the three different phenocryst phases.

	CPX	CPX	CPX	OPX	OPX	OPX	PLAG	PLAG	PLAG
	Mean	Std Dev	Literature Values	Mean	Std Dev	Literature Values	Mean	Std Dev	Literature Values
K	0.002	0.002	0.0185-0.056	0.004	0.004	0.0014-0.016	0.090	0.015	0.065-0.263
Ti	0.412	0.064	0.37-0.615	0.228	0.029	0.265-0.405	0.043	0.006	0.0433-0.0485
Mn	2.877	0.420	1.65-45	4.055	0.498	2.5-45.5	0.060	0.009	0.038-0.44
Sr	0.101	0.023	0.0648-0.516	0.003	0.002	0.005-0.2205	2.422	0.258	1.55-19.9
Y	0.949	0.198	0.28-2.7	0.169	0.032	0.365-0.755	0.012	0.005	0.01-0.51
Zr	0.097	0.024	0.162-2.4	0.016	0.003	0.0305-0.13	0.005	0.002	0.001-0.55
Nb	0.008	0.004	0.012-1.0	0.007	0.003	0.0027-0.78	0.008	0.004	0.0215-1.3
Ba	0.001	0.001	0.035-0.33	0.003	0.002	0.0027-0.56	0.186	0.020	0.125-1.93
La	0.082	0.024	0.047-1.23	0.003	0.003	0.0021-0.78	0.088	0.020	0.11-0.393
Nd	0.380	0.116	0.166-1.4	0.014	0.008	0.016-1.25	0.054	0.013	0.057-0.189
Sm	0.610	0.189	0.377-5.95	0.041	0.024	0.017-1.6	0.033	0.015	0.0425-0.17
Eu	0.626	0.239	0.411-4.5	0.052	0.052	0.028-0.825	0.397	0.134	0.394-5.85
Gd	0.907	0.275	0.583-1.41	0.064	0.043	0.027-0.223	0.037	0.025	0.039-0.129
Dy	0.926	0.202	0.774-8.4	0.138	0.056	0.041-1.8	0.013	0.007	0.0295-0.256
Ho	1.009	0.246	1.04	0.199	0.068	0.52	0.017	0.006	
Yb	0.973	0.297	0.634-7.55	0.350	0.111	0.115-2.2	0.010	0.005	0.013-0.1323
Hf	0.171	0.059	0.173-0.67	0.032	0.017	0.031-0.2	0.016	0.007	0.012-0.175
Pb	0.012	0.008	0.11-0.63	0.018	0.009	0.17-0.54	0.134	0.028	0.23-2.8

Table 4. Comparison of mean partition coefficients calculated from this study to the three most recent studies of similar magma compositions that utilized microanalytical technqiues. (1) Dunn & Sen, 1994; (2) Ewart & Griffin, 1994; (3) Forsythe et al., 1994.

	CPX	CPX 2	CPX 2	CPX 3	OPX	OPX 1	OPX 2	OPX 2	PLAG	PLAG 1	PLAG 2	PLAG 2	PLAG 2
	Mean	Andesite	Low-Si Rhyolite	Dacite	Mean	Andesite	Andesite	Low-Si Rhyolite	Mean	Andesite	Andesite	Dacite	Low-Si Rhyolite
Ti	0.412			0.34-0.89	0.228				0.043	0.04-0.057			
Mn	2.877	4.5	6.1		4.055		7.3	13.6-71.3	0.060		<0.038	0.17	<0.19
Sr	0.101	0.075	0.2		0.003	0.003-0.007	0.13	0.068-0.18	2.422	2.7-3.5	5.28	10.7	7.6-7.8
Y	0.949	0.28	2.7		0.169	0.19-0.54	0.46	0.44-1.07	0.012	0.01	<0.066	0.51	0.083-<0.18
Zr	0.097	2.4	0.17	0.096-0.291	0.016	0.021-0.04	0.13	0.075-0.086	0.005	0.001	0.15	0.55	0.10-0.18
Nb	0.008	<0.87	<1.0	0.004-0.02	0.007	0.0027	<0.78	<0.54-<0.73	0.008	0.01-0.033	<1.3		<0.31-<0.41
Ba	0.001	0.33	0.084		0.003		0.13	<0.063-<0.084	0.186	0.38-0.55	0.56	1.05	0.28-0.33
La	0.082				0.003	0.0019-0.0023			0.088	0.082-0.14			
Nd	0.380				0.014	0.013-0.027			0.054	0.045-0.069			
Sm	0.610				0.041	0.063-0.089			0.033	0.033-0.052			
Eu	0.626				0.052	0.059-0.086			0.397	0.55-0.79			
Gd	0.907				0.064	0.069-0.24			0.037	0.034-0.044			
Dy	0.926				0.138	0.15-0.4			0.013	0.025-0.034			
Ho	1.009				0.199	0.52			0.017				
Yb	0.973				0.350	0.39-0.92			0.010	0.012-0.014			
Pb	0.012	0.11	<0.63		0.018	0.29	<0.52	<0.028-<0.54	0.134	1.07	2.8	1.3	0.35-0.84

Table 5. Best-fit parameters for the Lattice Strain Model. Values in parentheses are 1 standard deviation on that parameter in terms of the least significant figure. E is Young's Modulus, ro is the ideal radius for the crystallographic site, and Do is the ideal non-strained partition coefficient for the crystallographic site.

Reference	**This study**	**1**	**1**	**2**
Mineral	Clinopyroxene	Diopside	Augite	Augite
Valence	3+	3+	3+	3+
r_0 (Å)	0.993 (6)	1.05	1.02	0.977-1.027
D_0	1.067 (9)	≈0.25		
E (GPa)	205 (25)	395.6	353.5	180-390

(1) Blundy & Wood 1994, (2) Wood and Blundy 1997

Figures

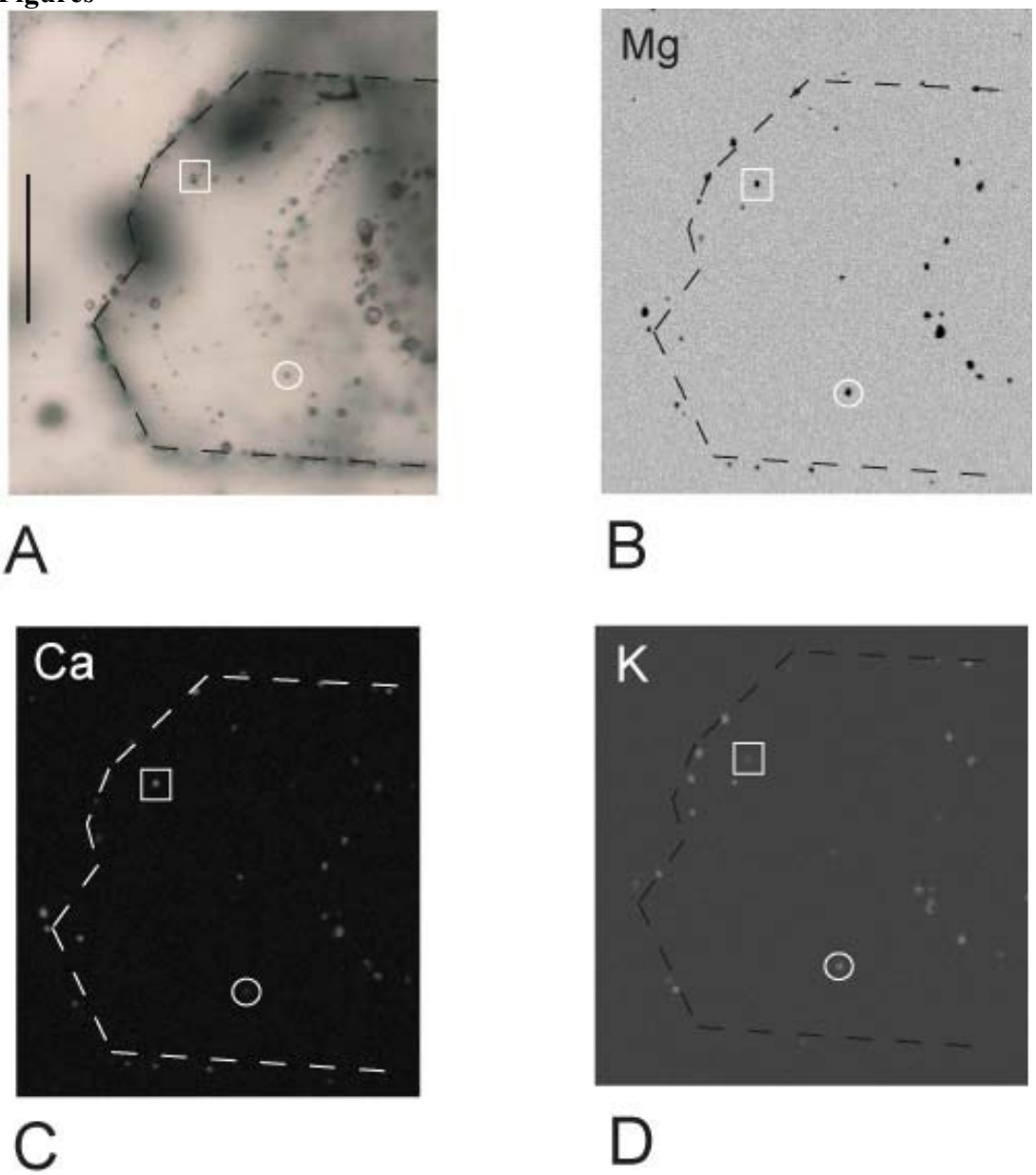

Figure 1 – (a) Photomicrograph of a portion of an orthopyroxene crystal from the 1988 eruption showing several well-defined crystal growth zone assemblages containing mineral and melt inclusions. One growth zone is outlined by a dashed line. Scale bar is 50μm. (b) Electron microprobe (EPMA) map of Mg with the host crystal significantly brighter than the inclusions. (c) EPMA map of Ca with the orthopyroxene host containing little Ca. Some inclusions are significantly brighter than others and contain more Ca than the others. The brighter inclusions are plagioclase while those slightly darker inclusions are melt inclusions. (d) EPMA map of K with the orthopyroxene host containing little K. All of the inclusions that are bright contain more K than either the host or the inclusions that were bright in (c) and are melt inclusions. The inclusion in the box are plagioclase inclusions, while the inclusion in the circle is a melt inclusion.

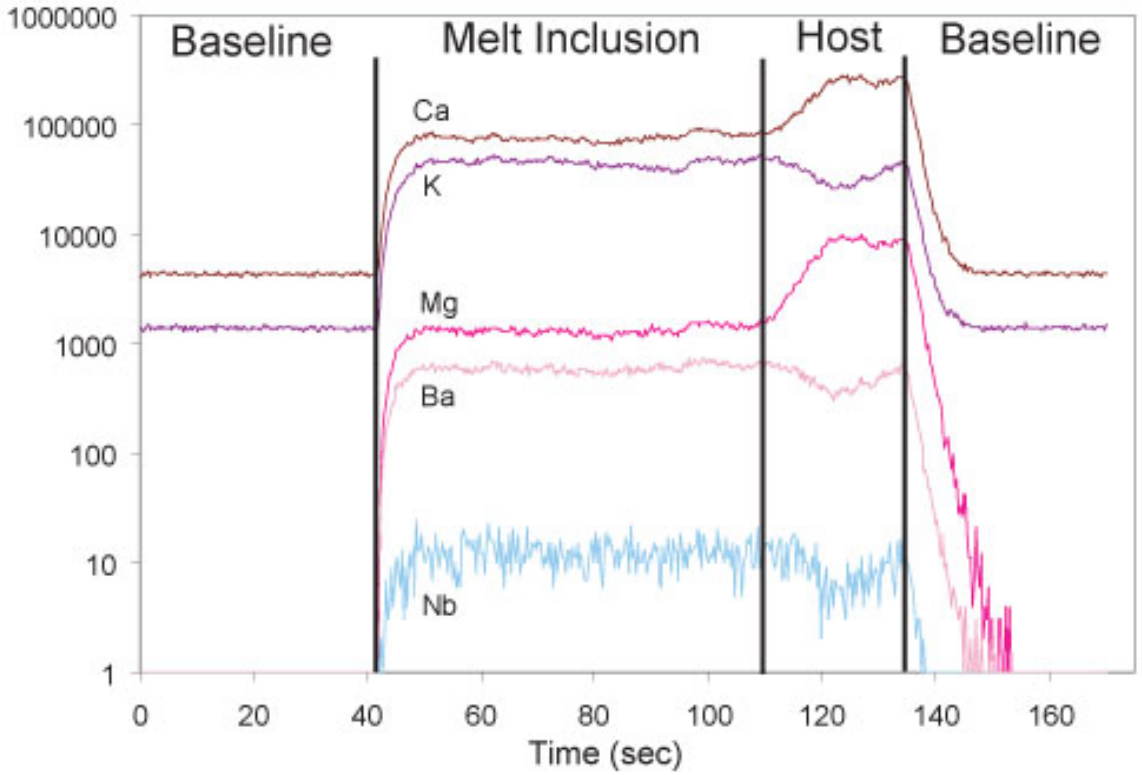

Figure 2 –LA-ICP-MS spectrum of a melt inclusion in orthopyroxene. The first section is the baseline signal of approximately 40 seconds. The vertical line separating this section from the next is when the laser has been turned onto the surface of the sample where the melt inclusion is located. The second section is the analysis of the melt inclusion lasting approximately 65 seconds, and the second vertical line separating this section from the third section is where the laser is now ablating through the host crystal beneath the melt inclusion. The section of host analysis last approximately 10 seconds long. The third vertical line indicates when the laser has been turned off and the final section is the flushing of the tubing to the ICP-MS and return of the signal to the background levels.

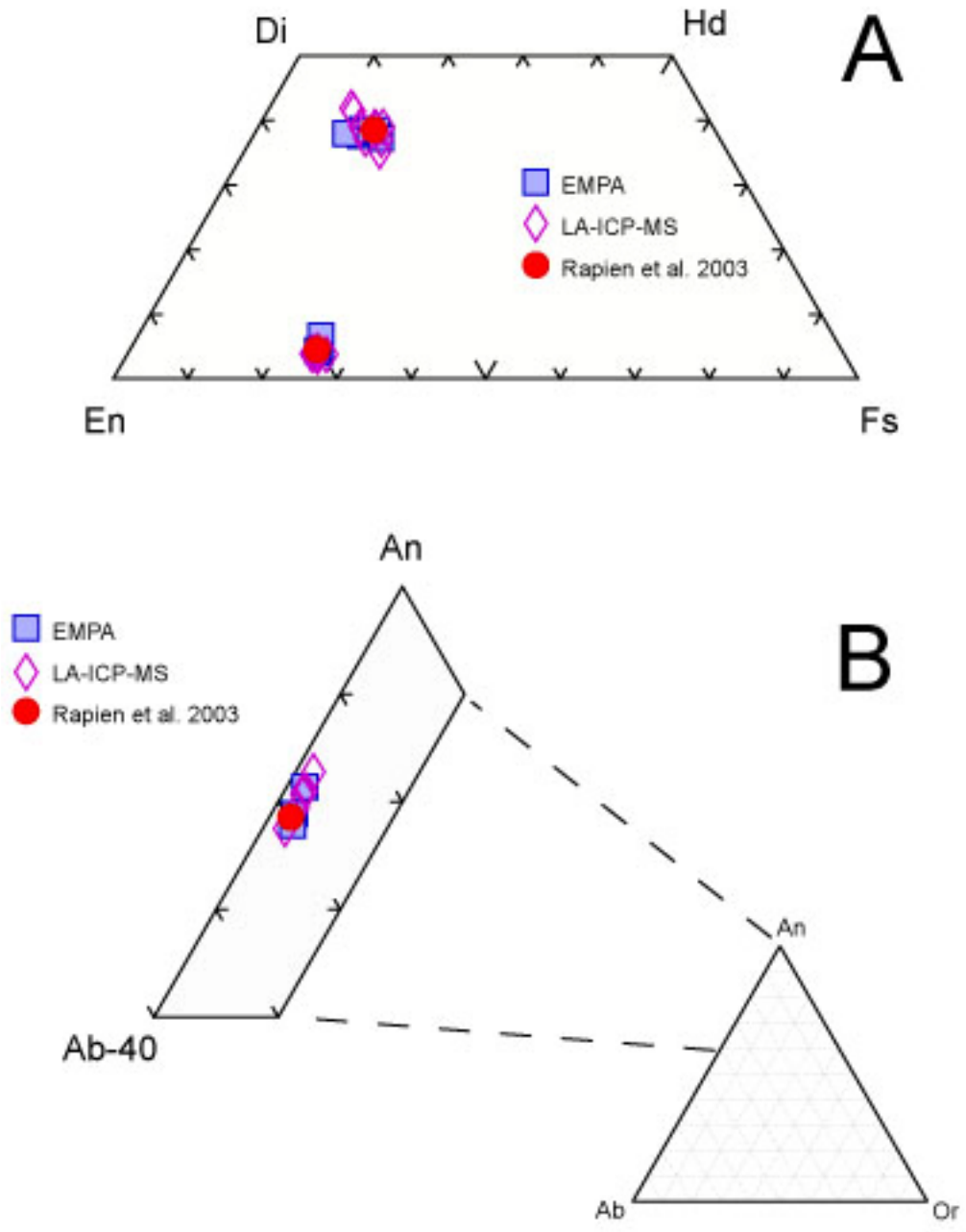

Figure 3 – (a) Pyroxene quadrilateral showing the compositions of the host clinopyroxene and orthopyroxene using both EPMA (filled square) and LA-ICP-MS (open diamond) techniques. Also shown are the average compositions determined by Rapien (1998) represented by the filled circle. (b) Plagioclase CNK triangle showing the compositions of the host plagioclase determined by EPMA and LA-ICP-MS and the average composition of Rapien (1998). Symbols are as in (a).

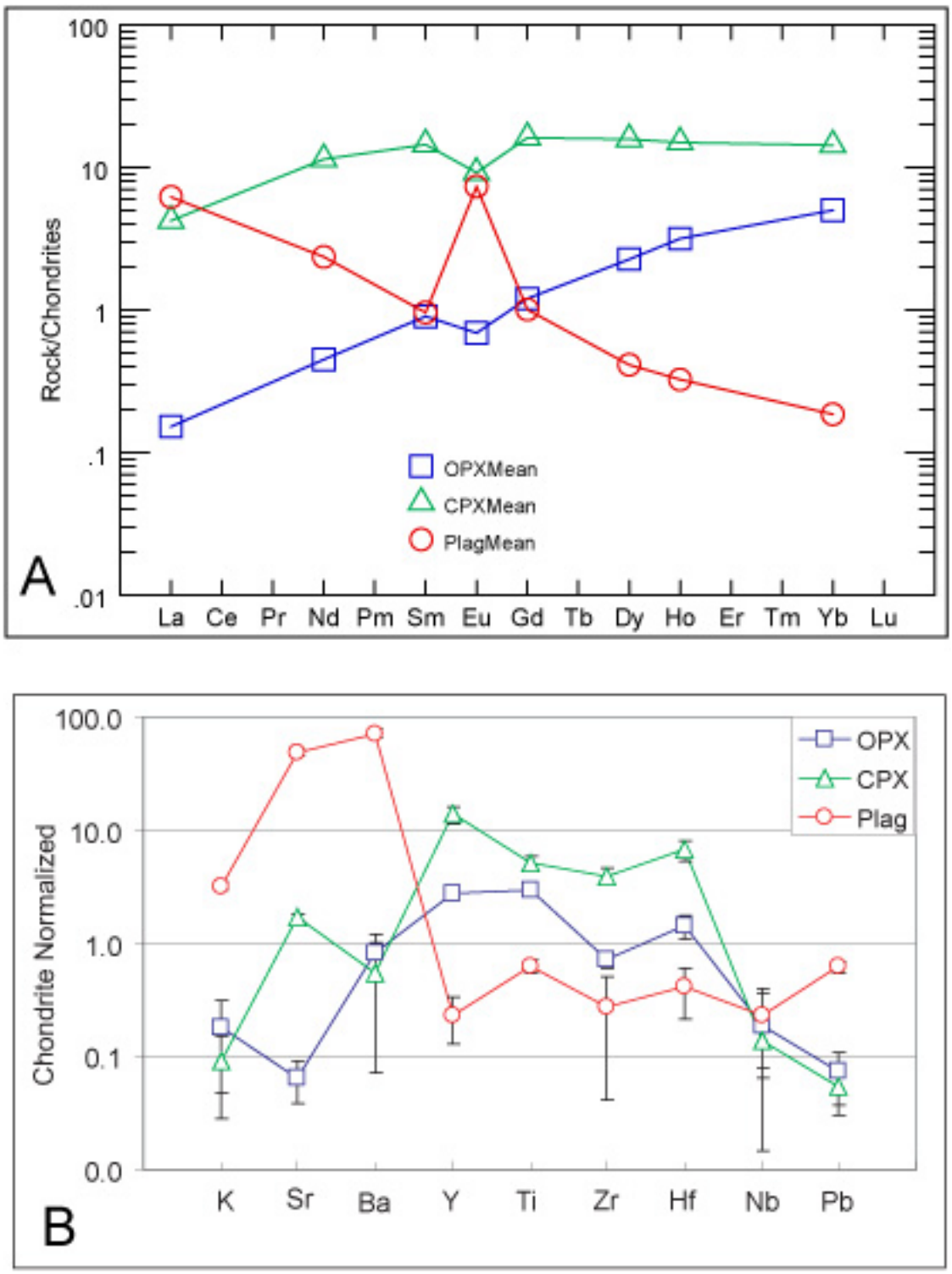

Figure. 4 – Chondrite-normalized (SUN and MCDONOUGH, 1989b) (a) REE concentrations and (b) LILE and HFSE concentrations for the average host compositions. Clinopyroxene, orthopyroxene, and plagioclase are represented by open triangles, open squares, and open circles respectively.

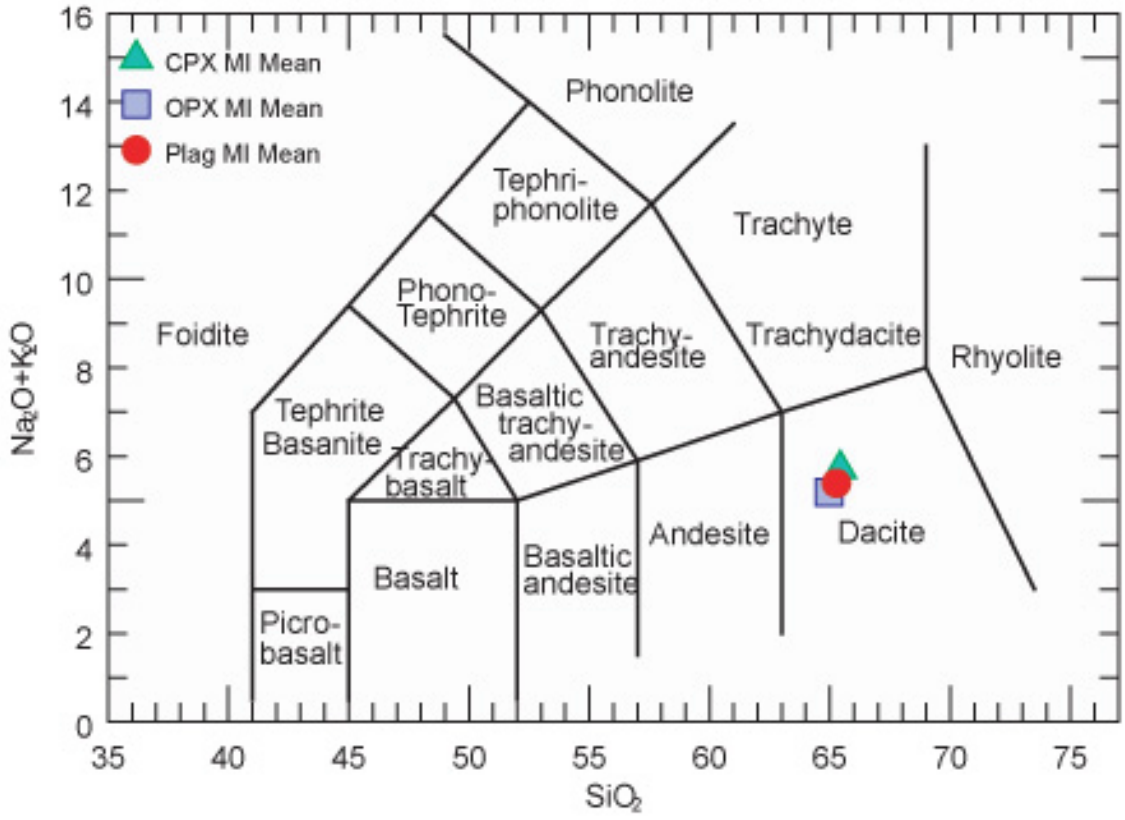

Figure 5 – Total alkali versus silica diagram showing the average melt inclusion compositions determined by LA-ICP-MS analyses. Clinopyroxene-hosted MI are represented by a filled triangle, orthopyroxene-hosted MI are represented by a filled square, and plagioclase-hosted MI are represented by a filled circle.

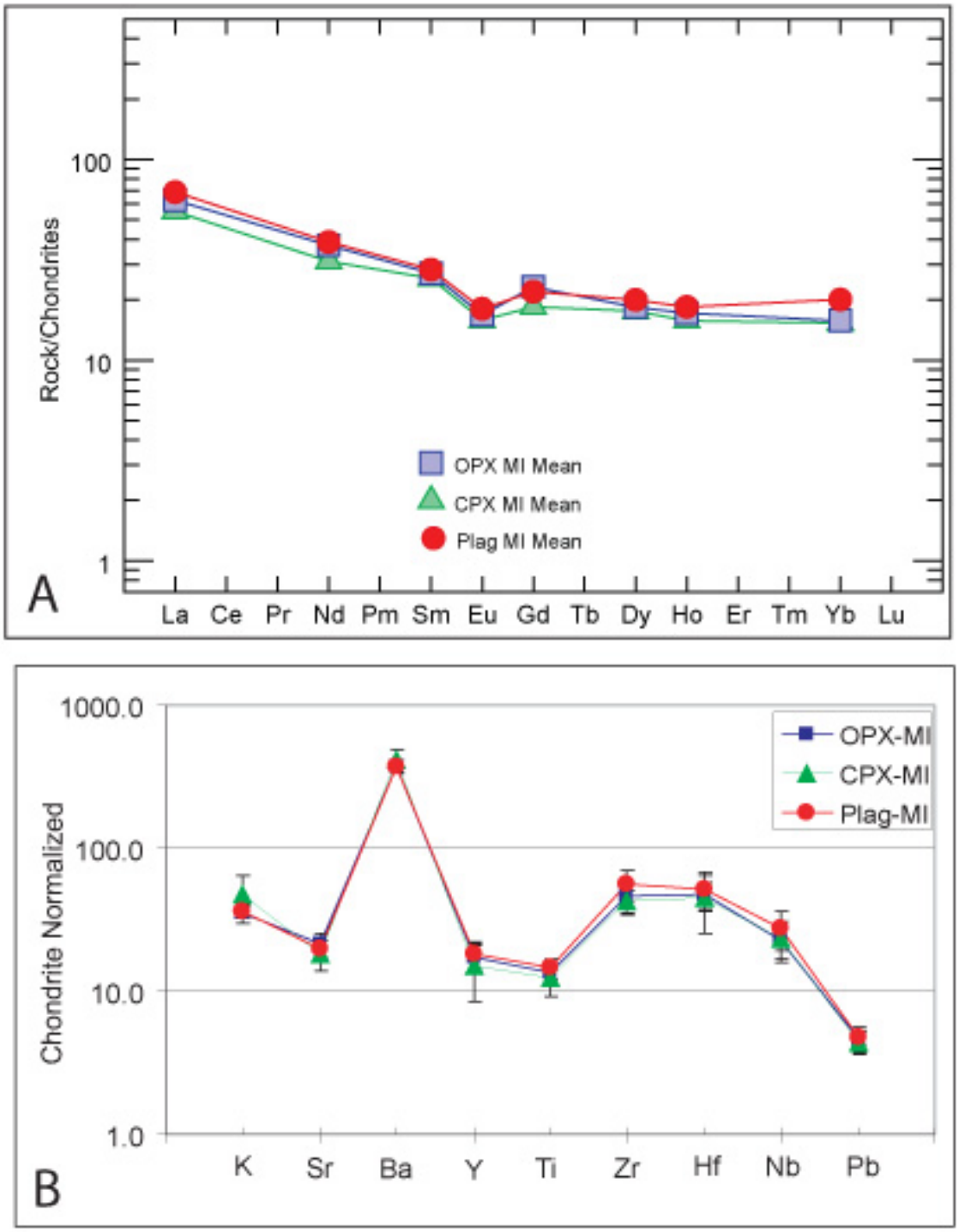

Figure 6 – Chondrite-normalized (Sun and McDonough 1989) (a) REE concentrations and (b) LILE and HFSE concentrations from average melt inclusion compositions. Clinopyroxene-hosted, orthopyroxene-hosted, and plagioclase-hosted melt inclusions are represented by filled triangles, filled squares, and filled circles respectively.

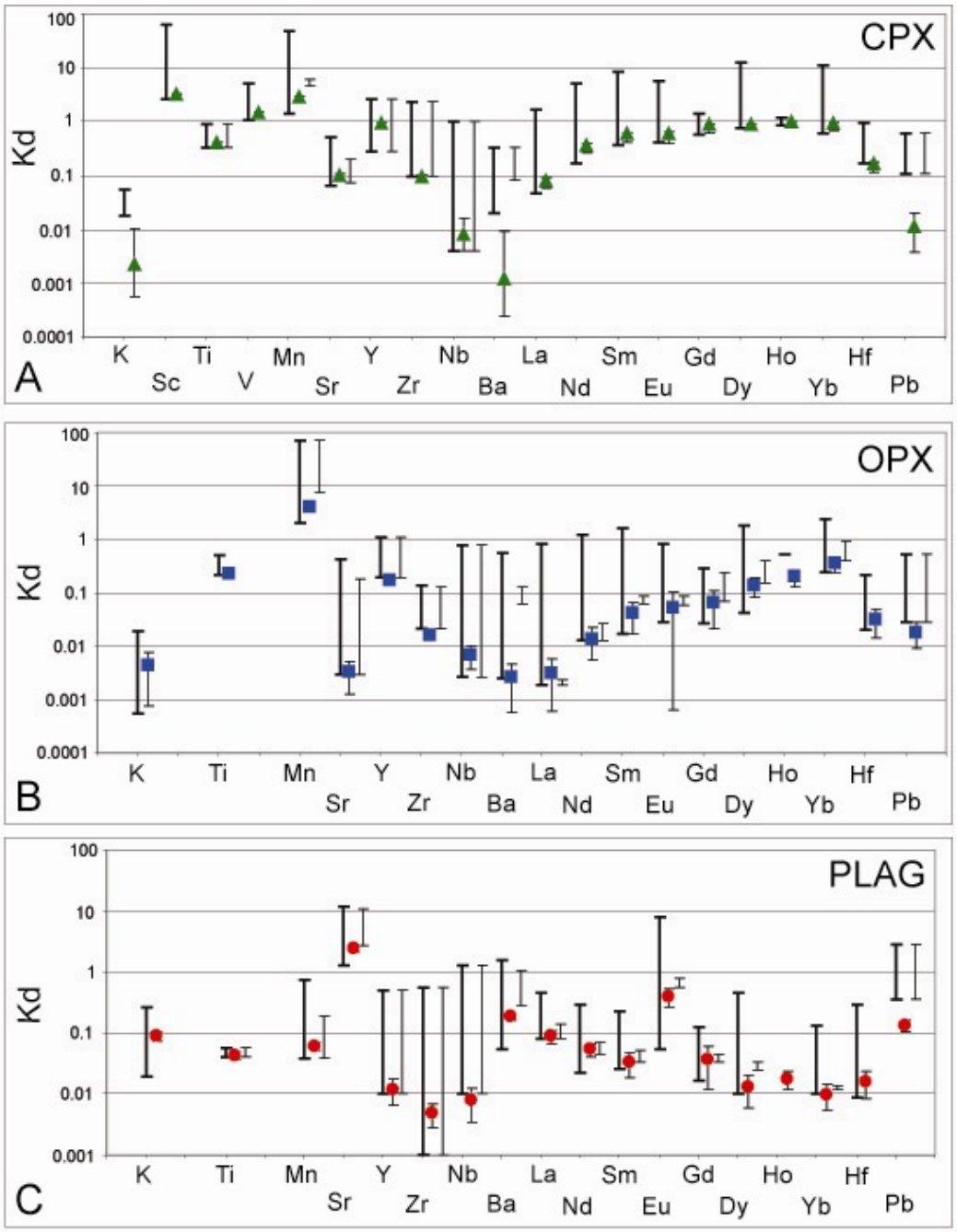

Figure 7 – Partition coefficients (K_d) for LILE, HFSE, and REE calculated from data listed in Tables 1 and 2 (represented by the symbols as in Fig. 6) compared to published literature values. The entire range of literature values are either plotted as single points or as a vertical bar representing the range of data published in that study. The three most recent studies utilizing microanalytical techniques (Dunn & Sen, 1994; Ewart & Griffin, 1994; Forsythe et al., 1994) are plotted as a separate vertical line to the right of the symbol for the data from this study. Partition coefficients are also listed in Table 3. Each data point includes 2σ standard deviation. (a) K_d for plagioclase, (b) K_d for orthopyroxene, (c) K_d for clinopyroxene.

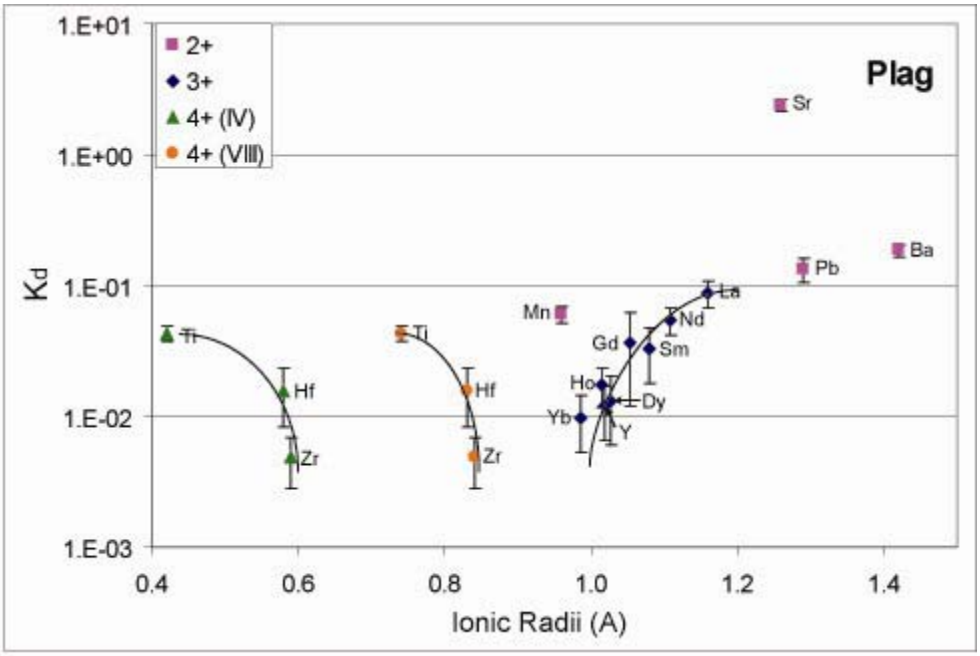

Figure 8 – "Onuma plot" of the average K_d calculated using melt inclusion/plagioclase pairs versus ionic radii (Onuma et al. 1966) for plagioclase. Cation radii are from Shannon (1976). 2σ standard deviation error bars are shown or are smaller than the symbol size. Also shown are the parabolic curves that fit the 4+ and 3+ cation series.

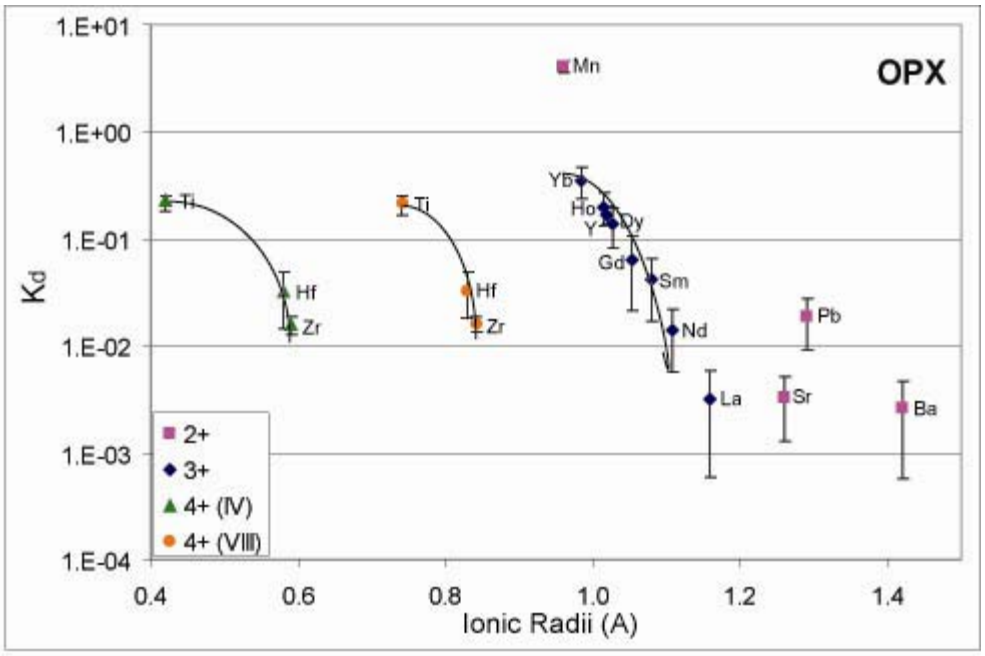

Figure 9 – "Onuma plot" of the average K_d calculated using melt inclusion/orthopyroxene pairs versus ionic radii (Onuma et al. 1966) for orthopyroxene. Cation radii are from Shannon (1976). 2σ standard deviation error bars are shown or are smaller than the symbol size. Also shown are the parabolic curves that fit the 4+ and 3+ cation series.

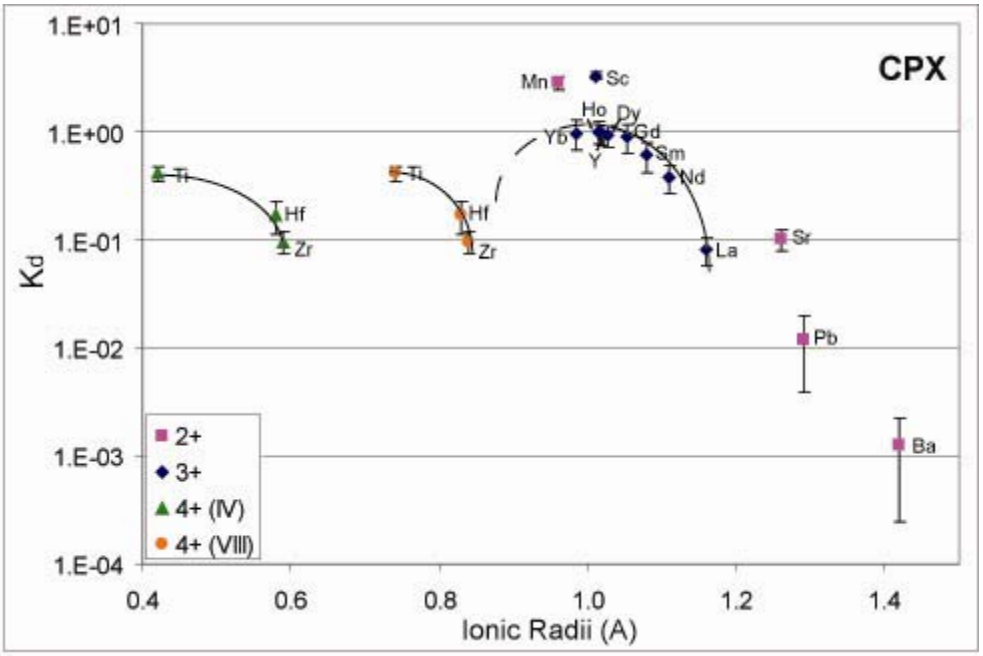

Figure 10 – "Onuma plot" of the average K_d calculated using melt inclusion/clinopyroxene pairs versus ionic radii (Onuma et al. 1966) for clinopyroxene. Cation radii are from Shannon (1976). 2σ standard deviation error bars are shown or are smaller than the symbol size. Also shown are the parabolic curves that fit the 4+ and 3+ cations.

Appendix 1

1.1 Trace element substitution behavior

To better understand the distribution of elements between phases we must first examine how these elements behave in the clinopyroxene, orthopyroxene, and plagioclase. Substitution of elements into crystals is controlled primarily by the charge and ionic radius of the substituting element. The closer the replacing element is in charge and size compared to the element to be replaced, the easier the substitution. Within the crystal lattice there may be multiple sites for replacement, such that elements with different size and charge may both enter the same crystal lattice in different crystallographic sites. The idealized formula for pyroxene is $XY(Si,Al)_2O_6$ where X typically represents Mg^{2+}, Fe^{2+}, Ca^{2+}, Na^{+}, and other large 1+ or 2+ cations, while Y represents Fe^{3+}, Al^{3+}, Cr^{3+}, Sc^{3+}, and other smaller cations. Both X and Y occur in octahedral coordination and are termed the M2 and M1 sites, respectively, while Si and Al occur in tetrahedral coordination. REE^{3+} have similar ionic radii to Ca^{2+} and should replace Ca^{2+} in the M2 site while $LILE^{1+}$ should also enter the larger M2 site rather than the smaller M1 site (JONES, 1995). Charge balancing of REE^{3+} would be accomplished by either a Tschermak substitution or additional incorporation of Al^{3+} for Si^{4+}. $HFSE^{4+}$ have been hypothesized to enter both the tetrahedral site in the place of Si or Al and in octahedral sites Ti and Nb should enter the M1 site and Zr and Hf entering the M2 site (WOOD and BLUNDY, 1997). The idealized formula for plagioclase is AT_4O_8 with A representing cation sites coordinated with nine oxygens and T representing tetrahedral sites. Previous research (SMITH and BROWN, 1988) has indicated that elements including $LILE^{1+}$, Na^{1+}, Ca^{2+}, and Fe^{2+}, and REE^{3+} should enter octahedral sites within the crystal structure, elements such as $HFSE^{4+}$, Fe^{3+}, Al^{3+}, and Si^{4+} should enter the tetrahedral site (AIGNER-TORRES et al., 2007). In addition, it has also been suggested that highly incompatible elements may enter defects in the crystal lattice and not have a direct relationship with ionic radius (URUSOV and DUDNIKOVA, 1998).

1.2 Accesory mineral effect

Different accessory mineral phases can incorporate different trace elements. For example, zircon can hold abundant HREE and HFSE, while inclusions of allanite could hold small amounts of LREE. If small proportions of these minerals are found as inclusions within phenocrysts they can greatly affect the partition coefficient. For example, if we assume a melt that contains 100 ppm La, and use a K_d of 0.08 for clinopyroxene (this study), this will result in a clinopyroxene crystal containing 8 ppm La. Inclusion in the clinopyroxene of different volumetric proportions of allanite-La, which can contain 8.5 wt% La_2O_3 (ORLANDI and PASERO, 2006), will greatly affect the amount of La that is measured in a bulk analysis of the clinopyroxene. Figure 11 shows the effect on the partition coefficient of incorporation of up to 1 vol% allanite in the crystal. Zircon has a K_d of 0.05 for La, so incorporation of small amounts of zircon as inclusions in the clinopyroxene will have a limited effect on the calculated partition coefficient (Fig. 11). However, this relationship would be reversed if an element such as Zr was considered, which is at high concentrations in zircon, and at very low concentrations in allanite. This hypothesis was suggested by Thomas et al. (2002) as the cause for the similar results found in that study using the melt inclusion-matrix technique compared to literature values.

References:

Aigner-Torres M., Blundy J., Ulmer P., and Pettke T. (2007) Laser ablation ICPMS study of trace element partitioning between plagioclase and basaltic melts: An experimental approach. *Contributions to Mineralogy and Petrology* **153**, 647-667.

Jones J. H. (1995) Experimental trace element partitioning. In *Rock Physics and Phase Relations: A Handbook of Physical Constants*, Vol. 3 (ed. T. J. Ahrens), pp. 73-104. American Geophysical Union.

Orlandi P. and Pasero M. (2006) Allanite-(La) from Buca della Vena mine, Apuan Alps, Italy, an epidote-group mineral. *Canadian Mineralogist* **44**, 63-68.

Smith J. V. and Brown W. L. (1988) *Feldspar Minerals: Crystal Structures, Physical, Chemical, and Microtextural Properties*. Springer.

Urusov V. S. and Dudnikova V. B. (1998) The trace-component trapping effect; Experimental evidence, theoretical interpretation, and geochemical application. *Geochimica et Cosmochimica Acta* **62**(7), 1233-1240.

Wood B. J. and Blundy J. D. (1997) A predictive model for rare earth element partitioning between clinopyroxene and anhydrous silicate melt. *Contributions to Mineralogy and Petrology* **129**, 166-181.

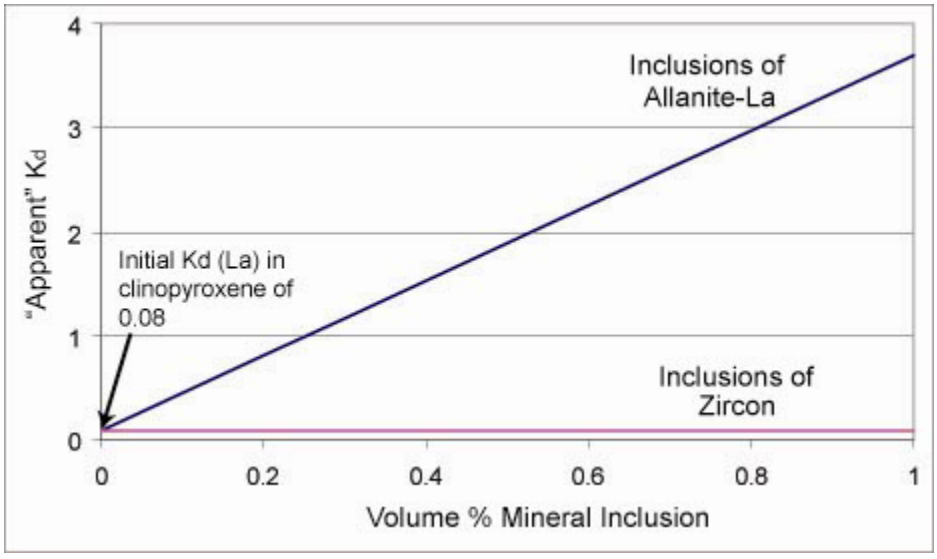

Figure 11 – Plot showing the affect of small (<1.0 vol%) amounts of allanite or zircon contaminants on the partition coefficient of La in a clinopyroxene host. The calculation used for this assumed 8.6 wt% La in allanite and K_D values of 0.08 and 0.05 for clinopyroxene and zircon, respectively.

Chapter 4: Magmatic processes between monogenetic eruptions, Procida Island, Campi Flegrei, Italy: Geochemical evidence from melt inclusions

Matthew J. Severs, Luca Fedele, and Robert J. Bodnar
Fluids Research Laboratory, Department of Geosciences, Virginia Polytechnic Institute and State University, Blacksburg VA 24061, USA

Paola Frattini, Annamaria Lima, and Benedetto De Vivo
Dipartimento di Scienza della Terra, Universita di Napoli "Federico II", Naples, Italy

Nobumichi Shimizu
Department of Geology and Geophysics, Woods Hole Oceanographic Institute, Woods Hole, MA 02543, USA

Abstract

Campi Flegrei is an active volcanic complex located in the greater Naples area, and has produced more than 50 eruptions ranging from small to extremely large over the past 60,000 years, including the Campanian Ignimbrite. The volcanic field includes not only the mainland area west of Naples, but also the two islands of Ischia and Procida. The volcanic products range from basalts to shoshonitic phonolites and trachytes, with the more evolved magmas being more abundant. Three eruptive units from Procida Island have been studied to observe geochemical trends over time within a small area.

Juvenile samples from Pozzo Vecchio, Breccia Museo, and Solchiara were collected to examine the compositions of melt inclusions (MIs). Fractional crystallization of olivine, clinopyroxene, and sanidine are probably responsible for the trends in major and trace elements observed in all three eruptions. Melt inclusions from Solchiara have narrow compositional ranges in major and trace elements (i.e., CaO, TiO_2, FeO, Zr, Dy, La, etc.) over a larger range in SiO_2 contents (47 to 55 wt%) while MI from the Breccia Museo have a limited range of SiO_2 contents (57 to 61 wt%) with a wider range for major and trace elements (i.e., FeO, Al_2O_3, CaO, La, Th, Rb). Pozzo Vecchio MI in clinopyroxene and sanidine define different chemical compositions, and petrographic evidence does not suggest a xenocrystic origin for either mineral phase. This suggests that Pozzo Vecchio is the result of magma mixing and not simply fractional crystallization. Volatile concentrations of Breccia Museo and Solchiara samples are not significantly different for CO_2, and S, while Cl, H_2O, and F are slightly higher in Breccia

Museo MIs compared to those from Solchiara. Trace element data suggests that the magma source was affected by both within-plate and subducted slab contributions to the original T-MORB seafloor.

Introduction

The Campanian region of Italy is one of the most heavily populated volcanic areas in the world. It has been experiencing approximately 60,000 years of explosive volcanic activity and has approximately 1.5 million people in the greater Neapolitan area. Inside the region reside the Somma-Vesuvius complex, and the Campi Flegrei field that also encompasses the islands of Ischia and Procida. Most of the eruptive units that are from the Campi Flegrei district are the results of small monogenetic eruptions, but the district is also responsible for one of the largest eruptions in the past 50,000 years, the Campanian Ignimbrite (CI). The CI covered about 30,000 km^2 with about 150-200 km^3 (DRE) of erupted material (BARBERI et al., 1991; ORSI et al., 1996). Samples from Procida are among the most primitive samples of the region and might be the closest to a parental magma. However, the island has also produced material that is compositionally closer to the more evolved shoshonitic rocks that are more common on Ischia and the mainland Campi Flegrei.

The source of the magmas in the Campanian region is not well understood and there are several models proposed. One model is that the magmas are predominantly the result of intra-plate, OIB-type magma (BECCALUVA et al., 1991). Another model is that there was mixing between mantle-derived magmas and upper continental crust. Several authors (AYUSO et al., 1998; CONTICELLI et al., 2004) have suggested that the parental source for Somma-Vesuvius was metasomatized asthenospheric mantle, with the source of the metasomatization due to fluids derived from the subducting slab. Finally, there is the hypothesis that the magmas are the result of a combination of intra-plate activity that is combined with a slab-derived source (PECCERILLO, 2001; PIOCHI et al., 2004). We have examined melt inclusions hosted in phenocrysts from three eruptive units on Procida (Solchiara, Breccia Museo, and Pozzo Vecchio), to try and better understand the source

of the magma in the Campi Flegrei region and to examine the evolution of the magmatic system over time.

Geologic Setting

The Phlegraean Volcanic District (PVD) lies in the Campanian Plain (CP) between the Southern Apennine Chain and the Tyrrhenian abyssal plain. The Tyrrhenian Sea has been opening since the late Miocene (SCANDONE, 1979) and caused the Calabrian arc to migrate SE and the subducted Ionian plate to rollback under Calabria (PANZA et al., 2007; PIROMALLO and MORELLI, 1997; SELVAGGI and CHIARABBA, 1995). The CP formed as a result of compression in the Apennine chain paired with the extension in the Tyrrhenian Sea and produced a graben-like structure within a Mesozoic carbonate platform. In addition the subduction beneath the Apennines also produced thinning of the continental lithosphere in the area between the Adriatic Sea and North Africa (PECCERILLO, 1999; SELVAGGI and AMATO, 1992; SERRI et al., 1993).

The PVD consists of three different volcanic fields: Campi Flegrei, Procida-Vivara island, and Ischia island (Fig. 1). The fields located in Campi Flegrei and Ischia have both current hydrothermal activity and recent recorded eruptions in 1538 AD for Campi Flegrei (Monte Nuovo eruption), and 1302 AD for Ischia (Arso eruption). The island of Procida is quiescent and the last eruption occurred approximately 13,000 YBP. Campi Flegrei is composed of both small monogenetic vents including Minopoli, Fondo Riccio, Torregaveta, and approximately 30 other eruptions, as well as the large eruptions of the Campanian Ignimbrite and the Neapolitan Yellow Tuff. Likewise Ischia is composed of both small monogenetic vents including Monte Cotto, Sant'Angelo, Molara, and approximately 30 other eruptions, as well as a large eruption in the Epomeo Green Tuff.

Procida-Vivara is only composed of small monogenetic vents that have limited areal output. There are five eruptive centers located on the island and include Vivara, Pozzo Vecchio, Terra Murata, Fiumicello, and Solchiara (Fig. 1a). Most of the stratigraphic sections showing these different units are found along the shorelines of the

island. Pozzo Vecchio, Fiumicello, and Solchiara are all tuff rings and Vivara and Terra Murata are both tuff cones.

The three oldest eruptions are Vivara, Pozzo Vecchio, and Terra Murata, however there is no stratigraphic evidence showing a direct temporal relationship between them. All three eruptive units are overlain by the Mt. Epomeo Green Tuff (derived from Ischia) which has been dated at 55 ka (VEZZOLI, 1988), thus providing a minimum age for the eruptions. De Astis et al. (2004) placed a maximum age of 70 ka for all of these units based upon the lack of additional deposits from the Parata Formation from Ischia. The age of the Fiumicello eruption is not well constrained. Some authors have placed it at approximately 30 ka based upon ^{14}C dating of paleosols directly underlying and overlying the Fiumicello products found at Monte di Procida (ALESSIO et al., 1973; ALESSIO et al., 1976), but more recent work has observed that the unit is interfingered with pumice deposits from the Pignatiello formation of Ischia that has an age range of 74-55 ka (DE ASTIS et al., 2004; ROSI et al., 1988). This places it in the same time interval as the Pozzo Vecchio, Vivara, and Terra Murata eruptions. However, there are no exposed sections that can definitively place one eruption before the others. Solchiara was the final eruption on the island and took place between 19.6 and 17.2 ka (ALESSIO et al., 1976; LIRER et al., 1991).

Another significant eruptive unit on Procida Island is the Breccia Museo that outcrops along the north and eastern parts of the island. Its origin is debated, with some authors describing it as being the proximal lag-deposits of the Campanian Ignimbrite (DE ASTIS et al., 2004; ORSI et al., 1996), while others place it as a separate unit with a vent location just off the northeastern shore of Procida (MELLUSO et al., 1995; PERROTTA and SCARPATI, 1994). If the Breccia Museo was indeed affiliated with the Campanian Ignimbrite than it was erupted between 37 ka (DEINO et al., 1992; PAPPALARDO et al., 2002a) and 39 ka (DE VIVO et al., 2001). Alternatively, data from ^{14}C dating place the eruption of the Breccia Museo at approximately 22 ka (LIRER et al., 1991).

Samples and Analytical Methods

Samples were collected from all the eruptive units from Procida, including the Breccia Museo. This study focused on samples from the Pozzo Vecchio, Breccia Museo, and Solchiara eruptive centers (Fig. 1). The other samples will be discussed in a future study. Sample PR03 was taken from the Solchiara I eruption and consists of juvenile scoriaceous material. The sample is a porphyritic basalt with few phenocrysts in a glassy vesicular matrix. Vesicles make up approximately 25-30% of the bulk rock. Phenocrysts make up less than 10% of the bulk rock and consist of olivine and clinopyroxene in equal proportions. Microlites are composed of clinopyroxene and plagioclase feldspar. Sample PR06 was taken from the distal phase of the Breccia Museo and consists of vesiculated, trachytic-phonolitic, juvenile pumice with approximately 10% phenocrysts of sanidine, clinopyroxene, biotite, and Ti-magnetite. Sanidine makes up approximately 60% of the phenocrysts, clinopyroxene approximately 30%, and biotite and magnetite make up the remaining 10%. These same minerals also occur as microlites in the glassy matrix. Vesicularity is approximately 30% of the bulk rock. Sample PR10 is a trachytic-phonolitic pumice from the Pozzo Vecchio eruptive unit. Phenocrysts (5%) are made up of sanidine, clinopyroxene, biotite, and magnetite in decreasing order of abundance. These same minerals occur as microlites in the matrix. Samples of each eruptive unit were lightly crushed in a mortar and crystals were separated by handpicking. Phenocrysts of olivine, clinopyroxene, and sanidine containing melt inclusions were selected for this study.

Olivine and clinopyroxene from Solchiara contained melt inclusions (MI) that ranged from glassy to slightly devitrified (Fig. 2). Most MIs had small shrinkage bubbles (i.e., "vacuum" bubbles created during cooling of the sample as a result of shrinkage around the glass transition temperature rather than a distinct vapor phase) (LOWENSTERN, 1995). Most MIs from the Solchiara sample were not heated because they were nearly homogenous initially. Also present in some of the olivine crystals were black inclusions that were not easily identifiable as melt inclusions. A few crystals containing these black inclusions were heated to see if they would homogenize, and they did not, suggesting they were empty spaces that had lost the melt component. Clinopyroxene and sanidine from both Pozzo Vecchio and the Breccia Museo contained MI with varying degrees of devitrification. All MIs were a dark brown color, most contained a shrinkage bubble, and

some inclusions had small daughter minerals present as well (Fig. 2). All crystals from these two eruptions were subsequently heated in order to obtain a homogenous glass for analysis.

Heating experiments were conducted at Virginia Tech using the heating stage developed at the Vernadsky Institute, Moscow (SOBOLEV and SLUTSKII, 1984). The melting temperatures of silver and gold (968°C and 1064°C, respectively) were used to calibrate the stage. Temperature measurement precision is ±3°C at 1200°C. Helium gas flowed through the stage in order to prevent oxidation of the samples during the heating experiment (DANYUSHEVSKY et al., 2000). Melt inclusions were heated until the brown color and all solid phases disappeared. Total homogenization of the melt inclusion was not always possible because the bubble (if present) did not dissolve back into the melt before the MI decrepitated (FEDELE et al., 2003). Thus the partial homogenization temperature (T_h) represents only a minimum trapping temperature. Samples were quenched to room temperature within 1-2 seconds and maintained their homogenous glassy state.

After the partial homogenization temperature had been recognized using the heating stage for MI in several clinopyroxene and sanidine crystals, more crystals were re-heated using a vertical tube furnace. Melt inclusion-bearing phenocrysts (of only one phase at a time) were placed into a Pt capsule that was lightly crimped at both ends. The capsule was then put into a vertical tube furnace that was set at approximately 350°C and was then taken to 75°C less than the approximate T_h as determined by the Vernadsky stage described above. This was done because it has been suggested that T_h attained using heating stages are typically higher than the actual trapping temperature due to rapid heating rates compared to heating rates in larger furnaces (LOWENSTERN, 1994; STUDENT and BODNAR, 1999; THOMAS, 1994). The samples were kept at that temperature for 5 minutes to equilibrate and then subsequently quenched by releasing the sample into a water bath below the furnace. Samples were then removed from the capsule and examined to see if homogenization was complete and phenocrysts with homogenized inclusions were removed from the capsule. For those that were not, they were placed back into the capsule and put back into the furnace, with the temperature being set 15°C higher. This process was repeated until all inclusions were homogenized.

Phenocrysts containing homogenized MI were mounted in Crystalbond, polished, and brought to the surface (THOMAS and BODNAR, 2002). Melt inclusions located along fractures were not selected for this study to minimize the possibility of re-equilibration of the samples. After one or more melt inclusions were exposed at the surface, the mounting medium was removed with acetone, and the crystal and exposed inclusions were then photographed so the location of the inclusion(s) was identifiable for future analyses.

Volatile concentrations (H_2O, CO_2, F, S, and Cl) in MIs were measured using a Cameca IMS 1280 secondary ion mass spectrometer (SIMS) at Woods Hole Oceanographic Institute, Massachusetts. The crystals (prepared as above) were placed into a metallic indium mount to eliminate possible contamination of hydrogen or carbon during SIMS analysis. Samples were gold-coated before being placed into the sample chamber of the ion microprobe. Analyses were conducted using a $^{133}Cs^{+}$ as the source of the ions with a current of 1.2 nA. All volatile concentrations were calculated using calibration curves relating the volatile concentration to the element/^{30}Si (where element is $^{16}O^{1}H$, ^{12}C, ^{19}F, ^{32}S, or ^{35}Cl) ratio determined using standards. A primary beam of 10 μm was rastered over a 30 μm × 30 μm spot for approximately 3 minutes before the analysis was conducted.

Major, minor, and trace element compositions of MIs and their host crystals were determined by laser-ablation inductively-coupled plasma mass-spectrometry (LA-ICP-MS) (HEINRICH et al., 2003). Analyses were conducted at Virginia Tech using an Agilent 7500ce quadrupole ICPMS and a 193 nm GeoLas Pro excimer laser ablation system. NIST 610 glass was analyzed as the standard for data reduction and for drift correction two times before and after a set of approximately 20 MI or host analyses. Laser setup for the analyses of the NIST glass, MIs, and host analyses was 27 kV, 150 mJ, with a pulse rate of 5 Hz.

Analyses were conducted by collecting approximately 30-45 seconds to establish the background signal before the laser was turned onto the surface of the inclusion or host. The laser ablates through the entire MI and into the host crystal, at which point the laser was shut off and the signal was allowed to return to background levels (Fig. 3). This transition between the inclusion and the host was monitored by observing the behavior of elements that were more abundant in the host phase than in the melt (such as Ni or Sc for

olivine or clinopyroxene). The first second or two of each analysis was ignored to avoid possible contaminants on the sample surface from airborne particles or previously ablated material deposited onto the surface.

The time resolved signals produced from the system were analyzed using AMS analytical software (MUTCHLER et al., 2007). All results were calculated by normalizing to 100% oxide totals. If volatile concentrations are high in the MIs then this can introduce a small error based upon the normalization, but for samples with low volatiles contents such as those from Procida (see below) this error is small (<2-3%). Some inclusions were exposed at the surface by hand polishing while other MIs occurred below the surface (≤100 μm). Melt inclusions below the surface were exposed using the laser ablation system with a laser pulse rate of 5 Hz, a laser spot size significantly larger than the MI (>45 μm), and turning the laser on for approximately 5 or 10 pulses. This removed the host material between the surface and the inclusion. After each 5 or 10 pulses of the laser, the sample was examined to see if the inclusion was exposed and if it was not then it another set of 5 or 10 pulses was applied to the sample. This process was repeated until the MI was exposed and clearly visible at the center of the ablation crater. After the signal returned to the background levels the MI was analyzed using the techniques mentioned above.

Each MI was analyzed using a laser spot size that was completely located within the MI to exclude signal from the host phase. This assured that MI analyses included only a contribution from the melt phase and eliminated the need to make a host correction as outlined by previous authors (HEINRICH et al., 2003; ZAJACZ and HALTER, 2007). Similarly, analyses of the host phase were conducted by choosing a laser spot located entirely in the host mineral and carefully avoiding inclusions at depth. Analytical conditions for the minerals were the same as those for the inclusions, except the minerals were analyzed for at least 20-30 seconds at each spot. Three or four spots in the host mineral around the melt inclusion were analyzed to test for homogeneity in the host mineral composition and to see if zonation was present.

Results

Table 1 summarizes the average host compositions for the three different phases present in the different eruptive units and all of the analyses are in Appendix 1. Olivines from Solchiara have compositions ranging from Fo_{75} to Fo_{79}. Clinopyroxene from the Pozzo Vecchio samples are diopsidic-salitic and have compositions in the range $En_{24-29}Fs_{17-24}Wo_{51-59}$ with a mean of $En_{27}Fs_{20}Wo_{53}$ and Mg# (calculated using FeO as the total Fe) ranging from 50.5 to 61.2. Clinopyroxene from the Breccia Museo fall in the diopside-salite field as well with compositions $En_{27-35}Fs_{10-22}Wo_{50-55}$ with a mean of $En_{31}Fs_{17}Wo_{52}$ and have Mg# ranging from 55.2 to 76.6. There is a gap in the Mg# between 65 and 75. Clinopyroxene from Solchiara are also diopsidic-salitic with compositions in the range $En_{30-39}Fs_{7-16}Wo_{52-55}$ with a mean of $En_{36}Fs_{10}Wo_{53}$ and have Mg# ranging from 64.7 to 84.6 with no compositional gap. Sanidine from the Breccia Museo has compositions in the range of $Or_{84-89}Ab_{8-13}An_{2-4}$ with a mean of $Or_{86.6}Ab_{10.1}An_{3.3}$. Sanidine from Pozzo Vecchio samples has compositions ranging from $Or_{81-84}Ab_{13-14}An_{3-6}$ with a mean of $Or_{82.7}Ab_{13.4}An_{3.9}$. Multiple laser ablation spots within the same crystal produced similar results suggesting that the crystals are not zoned, contrary to results reported by other authors (D'ANTONIO and DI GIROLAMO, 1994), or that the chemical zonation is below the detection limits of the analytical technique.

Melt inclusion T_h obtained using the Vernadsky stage ranged from 1009°C to 1100°C for sanidine and 1018°C to 1045°C for clinopyroxene from the Breccia Museo with a mean of 1035°C for sanidine and 1032°C for clinopyroxene. T_h ranged from about 1070°C to 1178°C for sanidine and from about 1080°C to 1125°C for clinopyroxene from Pozzo Vecchio with means of 1119°C and 1103°C for sanidine and clinopyroxene respectively. Tube furnace T_h for the Breccia Museo samples were in the range 975°C to 1050°C and for Pozzo Vecchio samples T_h was in the range 1050°C to 1115°C confirming the observations of previous authors that tube furnace homogenization temperatures are consistently lower than those obtained using a heating stage.

Chemical compositions (major and trace elements, and volatile concentrations) of MIs from Solchiara (PR03), Breccia Museo (PR06), and Pozzo Vecchio (PR10) are shown in Table 2. Volatile concentrations were measured using SIMS and major and trace element concentrations were measured using LA-ICP-MS as described above.

On the total alkali-SiO_2 classification diagram (Fig. 4, LE BAS et al., 1986), MIs from Solchiara plot in the basalt, basaltic andesite, trachybasalt, and basaltic trachyandesite fields, MIs from the Breccia Museo plot in the trachyandesite to trachyte fields (with one exception plotting as a basalt), and MIs from Pozzo Vecchio are divided with clinopyroxene hosted MIs plotting in the phonotephrite to trachyandesite fields while MIs from sanidine plot as phonolites and trachytes. The solitary clinopyroxene hosted MI from the Breccia Museo that plots as basalt is predicted to be a xenocryst and its composition was removed from the mean values for the rest of the Breccia Museo clinopyroxenes. Melt inclusions from Solchiara have a wide range of alkalis for a limited range for SiO_2 (Figs. 4 and 5). A similar trend is observed for clinopyroxene-hosted MIs from the Breccia Museo (Figs. 4 and 5). As suggested by previous workers (D'ANTONIO et al., 1999a; D'ANTONIO and DI GIROLAMO, 1994; DE ASTIS et al., 2004; PIOCHI et al., 2004), Solchiara is the most primitive of the three eruptive units used in this sample and Pozzo Vecchio is the most evolved. The classification for some of the MIs from the Breccia Museo as trachytes to phonolites are similar to those reported in the literature for the Breccia Museo itself (FULIGNATI et al., 2004; MELLUSO et al., 1995) and for the affiliated Campanian Ignimbrite (CIVETTA et al., 1997; MARIANELLI et al., 2006; SIGNORELLI et al., 1999). However, other MIs from both sanidine and clinopyroxene plot as trachyandesites (Fig. 4).

Harker diagrams showing major element concentrations for MIs versus SiO_2 show the wide range of composition between the three eruptions (Fig. 5). Olivine hosted MIs from Solchiara typically show a narrower range of compositions for SiO_2, Al_2O3, CaO, MgO, Na_2O, and TiO_2 than clinopyroxene hosted MIs from the same eruption. However, they do show the same lack of significant trends, as all major elements do not seem to increase or decrease significantly with SiO_2 content. Melt inclusions from Solchiara also show a larger range in SiO_2 (47.4% to 54.9%) compared to the Breccia Museo (56.9% to 60.2%), but a smaller range than the total range of both clinopyroxene and sanidine hosted melt inclusions from Pozzo Vecchio (51.8% to 61.0%). However, if the two different mineral phases from Pozzo Vecchio are considered separately, then the SiO_2 range for Solchiara is larger than either individual group. Clinopyroxene hosted MIs from the Breccia Museo have a significantly larger range in K_2O, CaO, Al_2O_3, and MgO than

sanidine hosted MIs from the same unit. MIs from Pozzo Vecchio show little to no significant change in major element chemistry for a small range in SiO_2 values with the exception of Na_2O. The overall trend when looking at all samples and not between sample sets is one of decreasing CaO, TiO_2, MgO, and FeO* and increasing K_2O, Na_2O with increasing SiO_2 content. These patterns are typical of crystallization of olivine and clinopyroxene from a parental alkali basalt magma.

Variations in volatile concentrations with SiO_2 are shown in Figure 6. The more evolved Breccia Museo samples have more Cl and possibly more F and H_2O than the less evolved Solchiara. However, these trends are not particularly strong. Solchiara products have a larger range of all volatiles compared to Breccia Museo samples with the exception of F.

Diagrams of SiO_2 versus trace elements and Zr versus Sc, Th, Nb, and Rb show similar trends to those from the major elements (Figs. 7 and 8). When all samples are considered, they show increasing Rb, La, Th, and Zr with increasing SiO_2 content, decreasing Ni (and also Sc, V, and Cr) content with increasing SiO_2 content, and no significant change in Dy content with increasing SiO_2 content. This is expected for a magma crystallizing olivine and clinopyroxene such that compatible elements such as Ni are taken into the crystal structure decreasing the amount left in the melt and incompatible elements (HFSE and LILE) increase in the melt with the amount of crystallization. Solchiara MI samples plot as a narrow range of trace elements for a range of SiO_2 content. Breccia Museo and Pozzo Vecchio MIs on the other hand typically have wide ranges of trace elements for a relatively narrow range of SiO_2 content. Trace element concentrations in MIs from Pozzo Vecchio clinopyroxenes are different from MIs from Pozzo Vecchio sanidines (Figs. 7 and 8).

Chondrite-normalized (SUN and MCDONOUGH, 1989) REE patterns of all Procida MI samples show the LREE enrichment compared to the HREE (Fig. 9). Pozzo Vecchio MIs show the greatest LREE/HREE enrichment and also display a negative Eu anomaly indicative of feldspar crystallization. Breccia Museo MI REE do not have as steep a slope as Pozzo Vecchio and do not show a significant Eu anomaly. Melt inclusions from Solchiara show limited enrichment of LREE compared to HREE and no negative Eu anomaly. This enrichment of incompatible elements is typical of Campanian province

including samples both from Procida, Ischia, and Campi Flegrei, including the Campanian Ignimbrite and smaller eruptions (CANNATELLI et al., 2007; CIVETTA et al., 1997; D'ANTONIO et al., 1999a; D'ANTONIO et al., 1999b; DE ASTIS et al., 2004; FEDELE et al., 2006; PAPPALARDO et al., 1999; PIOCHI et al., 2004). The spider diagram for Sr, K, Rb, Ba, Th, Ta, Nb, Ce, Zr, Hf, Sm, Ti, Y, and Yb normalized to MORB (Fig. 10, PEARCE, 1983) show a similar enrichment in LILE elements with the exception of Ba which is suggested to reflect crystallization of feldspar. This pattern is similar to that described by previous workers for the greater Campi Flegrei region (AYUSO et al., 1998; CANNATELLI et al., 2007; CIVETTA et al., 1997; DE ASTIS et al., 2004; PIOCHI et al., 2005; PIOCHI et al., 2004). Figure 11 shows the LILE/HFSE ratios are not changing significantly from less-evolved to more evolved samples. The Solchiara samples also show an enrichment in Ba compared to the more-evolved samples.

Discussion

Previous workers have shown that the Solchiara eruption produced one of the most primitive magmas in the Phlegraean Volcanic District and the results from this study confirm those observations. However, the compositions of MIs show that there is a range of compositions within the eruption as well. The major and trace element trends within the Solchiara sample set suggest that fractional crystallization of olivine, clinopyroxene, and magnetite is the dominant process taking place in that magma chamber (Figs. 5 and 6). This hypothesis is further enhanced by those trends continuing through the Breccia Museo and Pozzo Vecchio eruptions and elsewhere in the PVD (D'ANTONIO et al., 1999a; D'ANTONIO et al., 1999b; DE ASTIS et al., 2004; PAPPALARDO et al., 1999; PAPPALARDO et al., 2002b). However, one thing that needs to be considered is that the most evolved samples (Pozzo Vecchio) are the oldest, and the least evolved samples (Solchiara) are the youngest. This suggests that these eruptive products came from different reservoirs rather than from a single large magma chamber (DE ASTIS et al., 2004; PAPPALARDO et al., 2002b; PIOCHI et al., 2004). These eruptive units could originate from a single magma chamber only if the fractionating magmas were isolated from one another such as in a stratified magma chamber. This seems unlikely given the

fact that Sr, Nd, and Pb isotopes indicate that Solchiara and Pozzo Vecchio have different isotopic compositions (D'ANTONIO et al., 1999a; DE ASTIS et al., 2004). However, for Pozzo Vecchio, the presence of MIs with significantly different compositions (Figs 6-11) does suggest that mixing between different magmas was probable for this particular eruption. An alternative explanation is that the clinopyroxenes were xenocrysts and were from another source, but there is no petrographic evidence suggesting a xenocrystic origin for those crystals. This favors a hypothesis that each of the eruptive units were produced in small magma chambers that individually undergo fractional crystallization, and that for the eruption of Pozzo Vecchio, that magma mixing took place within the chamber, probably as a result of introduction of less differentiated magma, represented by MIs from the clinopyroxene phenocrysts, into the more evolved magma, represented by MIs from the sanidine crystals.

Although the overall tectonic setting is well constrained by geophysical observations (ORSI et al., 1999; PANZA et al., 2007; PIOCHI et al., 2005), there has been some debate about the exact origin of the magmas feeding the Phlegraean Volcanic District. Some authors favor an argument for primarily a volcanic arc generation related to the subduction zone, while others workers favor a model wherein the magmas have a source within the plate. There is also the possibility that aspects of both models may be accurate as well. Trace element discrimination diagrams were constructed using samples from Solchiara because they are the most primitive and closest to the parental magma to try and elucidate between these two models.

Figure 12 shows the Zr versus Zr/Y ratio (PEARCE and NORRY, 1979) and samples from Solchiara plot in both the MORB field and in the calc-alkaline basalt field. More evolved Campi Flegrei samples, such as Pozzo Vecchio, are typically of the shoshonitic trend, and their source magmas all have elevated incompatible elements derived from interaction with a subduction-derived fluid enriched in LILE and LREE. The location of some of the Solchiara samples within the calc-alkaline basalt field on Figure 12 supports this hypothesis. However, some of the samples also plot in the MORB field indicating that they still have a component of their original composition when they were located in what is now the Tyrrhenian Sea. Alternatively, the plot of the Nb/Y ratio versus Ti/Y ratio (Fig. 13, PEARCE, 1982) shows that Solchiara samples plot between the fields of

MORB, volcanic arc basalts, and also in the transitional to alkaline within-plate basalt fields. This behavior is also seen for the Zr-Ti/100-3Y diagram (Fig. 14, PEARCE and CANN, 1973) where the melt inclusion samples plot around the triple junction between the within-plate basalts, calc-alkaline basalts, and MORB. As the samples from Procida become more evolved, they have an increased component from intra-plate magmatic activity (Fig. 15, PEARCE and NORRY, 1979). As the magmas evolve into phonolites and trachytes they are also becoming more contaminated by crustal material that can also elevate the concentrations of incompatible elements (Fig. 10). The fact that the Solchiara melt inclusions are not affected by contamination or alteration allows for the identification of the MORB type. The plot of different HFSE (Zr, Nb, Y) against each other they suggest that the MORB source is transitional between the N-MORB and E-MORB types (Fig. 16, LE ROEX, 1987). A transitional MORB source is also suggested by D'Antonio et al. (1999a) for the Phlegraean Volcanic District.

Conclusions

Melt inclusions from Pozzo Vecchio, Breccia Museo, and Solchiara show an overall major and trace element trend of fractional crystallization of olivine, clinopyroxene, and ultimately sanidine. Compositions of melt inclusions from different phenocrysts for the different eruptions behave differently. MIs from olivine and clinopyroxene from Solchiara plot within the same area, while MIs from clinopyroxene from Breccia Museo plot over a wider compositional range than sanidine from the same eruption. Compositional data from clinopyroxene-hosted MI in Pozzo Vecchio appear to be completely different than sanidine-hosted MI compositions. Petrographic evidence does not support a xenocrystic origin for either sanidine or clinopyroxene and suggests that a mixing model is necessary to explain the completely different melt compositions. Volatile concentrations between the Breccia Museo and Solchiara samples are not significantly different for CO_2, and S, while Cl, H_2O, and F are slightly higher in Breccia Museo MIs compared to those from Solchiara. All of the trace element data suggests that there are components of the original seafloor, of subduction related fluid activity, and within-plate contamination in the samples from Procida.

Acknowledgements

The authors would like to thank Claudia Cannatelli for laboratory assistance and comments on the manuscript, and Rosario Esposito for discussions on Campanian volcanism. Funding was provided by the Cunningham Fellowship from Virginia Tech to MJS and NSF grants EAR-0337094 and EAR-0322119 to RJB.

References:

Alessio M., Bella F., Improta S., Belluomini G., Calderoni G., Cortesi C., and Turi B. (1973) University of Rome Carbon-14 dates X. *Radiocarbon* **15**(1), 165-178.

Alessio M., Bella F., Improta S., Belluomini G., Calderoni G., Cortesi C., and Turi B. (1976) University of Rome Carbon-14 dates XIV. *Radiocarbon* **18**(3), 321-349.

Ayuso R. A., De Vivo B., Rolandi G., Seal R. R. I., and Paone A. (1998) Geochemical and isotopic (Nd-Pb-Sr-O) variations bearing on the genesis of volcanic rocks from Vesuvius, Italy. *Journal of Volcanology and Geothermal Research* **82**, 53-78.

Barberi F., Cassano E., La Torre P., and Sbrana A. (1991) Structural evolution of Campi Flegrei Caldera in light of volcanological and geophysical data. *Journal of Volcanology and Geothermal Research* **48**(1/2), 33-49.

Beccaluva L., Di Girolamo P., and Serri G. (1991) Petrogenesis and tectonic setting of Roman volcanic province, Italy. *Lithos* **26**, 191-221.

Cannatelli C., Lima A., Bodnar R. J., De Vivo B., Webster J. D., and Fedele L. (2007) Geochemistry of melt inclusions from the Fondo Riccio and Minopoli 1 eruptions at Campi Flegrei (Italy). *Chemical Geology* **237**, 418-432.

Civetta L., Orsi G., Pappalardo L., Fisher R. V., Heiken G., and Ort M. (1997) Geochemical zoning, mingling, eruptive dynamics and depositional processes - the Campanian Ignimbrite, Campi Flegrei caldera, Italy. *Journal of Volcanology and Geothermal Research* **75**, 183-219.

Conticelli S., Melluso L., Perini G., Avanzinelli R., and Boari E. (2004) Petrologic, geochemical and isotopic characteristics of potassic and ultrapotassic magmatism in central-southern Italy: Inferences on its genesis and on the nature of mantle sources. *Periodico di Mineralogia* **73**, 135-164.

D'Antonio M., Civetta L., and Di Girolamo P. (1999a) Mantle source heterogeneity in the Campanian Region (South Italy) as inferred from geochemical and isotopic features of mafic volcanic rocks with shoshonitic affinity. *Mineralogy and Petrology* **67**, 163-192.

D'Antonio M., Civetta L., Orsi G., Pappalardo L., Piochi M., Carandente A., De Vita S., Di Vito M. A., and Isaia R. (1999b) The present state of the magmatic system of Campi Flegrei caldera based on a reconstruction of its behavior in the past 12 ka. *Journal of Volcanology and Geothermal Research* **91**, 247-268.

D'Antonio M. and Di Girolamo P. (1994) Petrological and geochemical study of mafic shosonitic volcanics from Procida-Vivara and Ventotene Islands (Campanian Region, South Italy). *Acta Vulcanologica* **5**, 69-80.

Danyushevsky L. V., Della-Pasqua F. N., and Sokolov S. (2000) Re-equilibration of melt inclusions trapped by magnesian olivine phenocrysts from subduction-related magmas: Petrological implications. *Contributions to Mineralogy and Petrology* **138**, 68-83.

De Astis G., Pappalardo L., and Piochi M. (2004) Procida volcanic history: New insights into the evolution of the Phlegraean Volcanic District (Campania region, Italy). *Bulletin of Volcanology* **66**, 622-641.

De Vivo B., Rolandi G., Gans P. B., Calvert A., Bohrson W. A., Spera F. J., and Belkin H. E. (2001) New constraints on the pyroclastic eruptive history of the Campanian volcanic Plain (Italy). *Mineralogy and Petrology* **73**, 121-143.

Deino A., Curtis G., and Rosi M. (1992) $^{40}Ar/^{39}Ar$ dating of the Campanian Ignimbrite, Campanian Region, Italy. *International Geological Congress*, 633.

Fedele L., Bodnar R. J., De Vivo B., and Tracy R. J. (2003) Melt inclusion geochemistry and computer modeling of trachyte petrogenesis at Ponza, Italy. *Chemical Geology* **194**, 81-104.

Fedele L., Morra V., Perrotta A., and Scarpati C. (2006) Volcanological and geochemical features of the products of the Fiumicello eruption, Procida Island, Campi Flegrei (southern Italy). *Periodico di Mineralogia* **75**(1), 43-72.

Fulignati P., Marianelli P., Proto M., and Sbrana A. (2004) Evidences for disruption of a crystallizing front in a magma chamber during caldera collapse: An example from the Breccia Museo unit (Campanian Ignimbrite eruption, Italy). *Journal of Volcanology and Geothermal Research* **133**, 141-155.

Heinrich C. A., Pettke T., Halter W. E., Aigner-Torres M., Audetat A., Gunther D., Hattendorf B., Bleiner D., Guillong M., and Horn I. (2003) Quantitative multi-element analysis of minerals, fluid and melt inclusions by laser-ablation inductively-coupled-plasma mass-spectrometry. *Geochimica et Cosmochimica Acta* **67**(18), 3473-3496.

Le Bas M. J., Le Maitre R. W., Streckeisen A., and Zanettin B. (1986) A chemical classification of volcanic rocks based on the total alkali-silica diagram. *Journal of Petrology* **27**, 745-750.

Le Roex A. P. (1987) Source regions of mid-ocean ridge basalts: Evidence for the enrichment processes. In *Mantle Metasomatism* (ed. M. A. Menzies and C. J. Hawkesworth), pp. 389-422. Academic Press.

Lirer L., Rolandi G., and Rubin M. (1991) ^{14}C age of the Breccia Museo and its relevance for the origin of the Campanian Ignimbrite. *Journal of Volcanology and Geothermal Research* **48**, 223-227.

Lowenstern J. B. (1994) Chlorine, fluid immiscibility, and degassing in peralkaline magmas from Pantelleria, Italy. *American Mineralogist* **79**, 353-369.

Lowenstern J. B. (1995) Applications of silicate-melt inclusions to the study of magmatic volatiles. In *Magmas, Fluid and Ore Deposits*, Vol. 23 (ed. J. F. H. Thompson), pp. 71-99. Mineralogical Association of Canada.

Marianelli P., Sbrana A., and Proto M. (2006) Magma chamber of the Campi Flegrei supervolcano at the time of the eruption of the Campanian Ignimbrite. *Geology* **34**(11), 937-940.

Melluso L., Morra V., Perrotta A., Scarpati C., and Adabbo M. (1995) The eruption of The Breccia Museo (Campi Flegrei, Italy): Fractional crystallization processes in a shallow, zones magma chamber and implications for the eruptive dynamics. *Journal of Volcanology and Geothermal Research* **68**, 325-339.

Mutchler S. R., Fedele L., and Bodnar R. J. (2007) AMS a new software package for reduction of Laser Ablation ICPMS data. *ECROFI XIX*.

Orsi G., De Vita S., and Di Vito M. (1996) The restless, resurgent Campi Flegrei nested caldera (Italy): Constraints on its evolution and configuration. *Journal of Volcanology and Geothermal Research* **74**, 179-214.

Orsi G., Patella D., Piochi M., and Tramacere A. (1999) Magnetic modeling of the Phlegraean Volcanic District with extension to the Ponza archipelago, Italy. *Journal of Volcanology and Geothermal Research* **91**, 345-360.

Panza G. F., Peccerillo A., Aoudia A., and Farina B. (2007) Geophysical and petrological modelling of the structure and composition of the crust and upper mantle in complex geodynamic settings: The Tyrrhenian Sea and surroundings. *Earth-Science Reviews* **80**(1-2), 1-46.

Pappalardo L., Civetta L., D'Antonio M., Deino A. L., Di Vito M. A., Orsi G., Carandente A., De Vita S., Isaia R., and Piochi M. (1999) Chemical and Sr-isotopical evolution of the Phlegraean magmatic system before the Campanian Ignimbrite and the Neapolitan Yellow Tuff eruptions. *Journal of Volcanology and Geothermal Research* **91**, 141-166.

Pappalardo L., Civetta L., De Vita S., Di Vito M. A., Orsi G., Carandente A., and Fisher R. V. (2002a) Timing of magma extraction during the Campanian Ignimbrite eruption (Campi Flegrei Caldera). *Journal of Volcanology and Geothermal Research* **114**, 479-497.

Pappalardo L., Piochi M., D'Antonio M., Civetta L., and Petrini R. (2002b) Evidence for multi-stage magmatic evolution during the past 60 kyr at Campi Flegrei (Italy) deduced from Sr, Nd and Pb isotope data. *Journal of Petrology* **43**(8), 1415-1434.

Pearce J. A. (1982) Trace element characteristics of lavas from destructive plate boundaries. In *Andesites* (ed. R. S. Thorpe), pp. 525-548. Wiley.

Pearce J. A. (1983) Role of the sub-continental lithosphere in magma genesis at active continental margins. In *Continental Basalts and Mantle Xenoliths* (ed. C. J. Hawkesworth and M. J. Norry), pp. 230-249. Shiva

Pearce J. A. and Cann J. R. (1973) Tectonic setting of basic volcanic rocks determined using trace element analyses. *Earth and Planetary Sciences Letters* **19**, 290-300.

Pearce J. A. and Norry M. J. (1979) Petrogenetic implications of Ti, Zr, Y, and Nb variations in volcanic rocks. *Contributions to Mineralogy and Petrology* **69**, 33-47.

Peccerillo A. (1999) Multiple mantle metasomatism in central-southern Italy: Geochemical effects, timing and geodynamic implications. *Geology* **27**, 315-318.

Peccerillo A. (2001) Geochemical similarities between the Somma-Vesuvius, Phlegraean Fields and Stromboli volcanoes: Petrogenetic, geodynamic and volcanological implications`. *Mineralogy and Petrology* **73**(1-3), 93-105.

Perrotta A. and Scarpati C. (1994) The dynamics of the Breccia Museo eruption (Campi Flegrei, Italy) and the significance of spatter clasts associated with lithic breccias. *Journal of Volcanology and Geothermal Research* **59**(3), 335-355.

Piochi M., Bruno P. P., and De Astis G. (2005) Relative roles of rifting tectonics and magma ascent processes: Inferences from geophysical, structural, volcanological, and geochemical data for the Neapolitan volcanic region (southern Italy). *Geochemistry, Geophysics, Geosystems* **6**(7), 25.

Piochi M., Pappalardo L., and De Astis G. (2004) Geochemical and isotopical variations within the Campanian Comagmatic Province: Implications on magma source composition. *Annals of Geophysics* **47**(4), 1485-1499.

Piromallo C. and Morelli A. (1997) Imaging the Mediterranean upper mantle by P-wave travel time tomography. *Annuals of Geophysics* **40**, 963-979.

Rosi M., Sbrana A., and Vezzoli L. (1988) Tephrostratigraphy of Ischia, Procida and Campi Flegrei volcanic products. *Memorie della Societa Geologica Italiana* **41**, 1015-1027.

Scandone P. (1979) Origin of the Tyrrhenian Sea and Calbrian Arc. *Bolletino della Societa Geologica Italiana* **98**, 27-34.

Selvaggi G. and Amato A. (1992) Subcrustal earthquakes in the Northern Apennines (Italy): Evidence for a still active subduction zone? *Geophysical Research Letters* **19**, 2127-2130.

Selvaggi G. and Chiarabba G. (1995) Seismicity and P-wave velocity image of the southern Tyrrhenian subduction zone. *Geophysics Journal International* **121**, 818-826.

Serri G., Innocenti F., and Manetti P. (1993) Geochemical and petrological evidence of the subduction of delaminated Adriatic continental lithosphere in the genesis of the Neogene-Quaternary magmatism of central Italy. *Tectonophysics* **223**, 117-147.

Signorelli S., Vaggelli G., Francalanci L., and Rosi M. (1999) Origin of magmas feeding the Plinian phase of the Campanian Ignimbrite eruption, Phlegraean Fields (Italy): Constraints based on matrix-glass and glass-inclusion compositions. *Journal of Volcanology and Geothermal Research* **91**, 199-220.

Sobolev A. V. and Slutskii A. B. (1984) Composition and crystallization conditions of the initial melt of the Siberian meimechites in relation to the general problem of ultrabasic magmas. *Soviet Geology and Geophysics* **25**(12), 93-104.

Student J. J. and Bodnar R. J. (1999) Synthetic fluid inclusions XIV: Coexisting silicate melt and aqueous fluid inclusions in the haplogranite-H_2O-NaCl-KCl system. *Journal of Petrology* **40**(10), 1509-1525.

Sun S. S. and McDonough W. F. (1989) Chemical and isotopic systematics of oceanic basalts: Implications for mantle composition and processes. In *Magmatism in the Ocean Basins* Vol. 42 (ed. A. D. Saunders and M. J. Norry), pp. 313-345. Blackwell Scientific Publications.

Thomas J. B. and Bodnar R. J. (2002) A technique for mounting and polishing melt inclusions in small (>1 mm) crystals. *American Mineralogist* **87**(10), 1505-1508.

Thomas R. (1994) Estimation of water contents of granitic melts from inclusion data. In *Metallogeny of collisional orogens focused on the Erzgebirge and comparable metallogenetic settings* (ed. R. Seltmann, H. Kampf, and P. Moller), pp. 224-229. Czech Geological Survey.

Vezzoli L. (1988) *Island of Ischia*. C.N.R.

Zajacz Z. and Halter W. (2007) LA-ICPMS analyses of silicate melt inclusions in co-precipitated minerals: Quantification, data analysis and mineral/melt partitioning. *Geochimica et Cosmochimica Acta* **71**, 1021-1040.

Tables

Table 1. Average host composition as determined by LA-ICP-MS for Solchiara (PR03), Breccia Museo (PR06), and Pozzo Vecchio (PR10). All oxides are in wt% and all trace elements are in ppm. Dashes indicate the element was below detection limits. Ol = Olivine host, CPX = clinopyroxene host, San = sanidine host

Sample	PR03	PR03	PR06	PR06	PR10	PR10
Host Label	Ol	CPX	CPX	San	CPX	San
Na_2O	0.01	0.26	0.35	1.58	0.50	2.02
MgO	44.23	15.25	13.23	0.00	11.84	0.01
Al_2O_3	0.04	4.57	3.95	20.47	4.31	21.33
SiO_2	42.02	51.73	51.35	63.54	50.41	62.87
K_2O	0.00	0.03	0.07	13.56	0.01	12.48
CaO	0.26	22.45	22.73	0.52	22.87	0.59
TiO_2	0.01	0.77	0.51	0.05	0.77	0.07
MnO	0.22	0.10	0.32	0.00	0.49	0.00
FeO*	12.87	4.40	7.32	0.18	8.60	0.20
Sc	15.106	109.818	92.850	11.942	43.680	11.514
V	4.207	234.418	165.875	0.354	125.666	1.152
Cr	112.363	2197.157	112.629	1.360	-	30.148
Ni	2510.673	547.843	680.828	15.905	747.430	19.774
Rb	-	2.073	3.450	215.236	-	217.276
Sr	0.271	75.083	101.516	403.616	96.868	1970.843
Y	0.113	13.951	43.997	0.335	78.996	0.180
Zr	0.064	34.777	105.222	4.133	273.928	0.999
Nb	0.017	0.254	0.545	1.997	1.506	0.258
Cs	-	0.123	0.286	1.188	-	1.198
Ba	0.333	5.128	2.391	163.022	0.533	1320.560
La	0.011	3.265	16.879	6.491	53.732	5.067
Ce	0.035	12.415	58.493	4.976	160.828	3.786
Sm	0.003	3.919	14.069	0.088	28.288	0.176
Eu	0.009	1.190	3.703	1.600	5.621	2.153
Tb	0.012	0.570	1.867	0.017	3.290	0.014
Dy	0.039	3.299	10.362	0.041	17.580	0.033
Yb	0.028	1.097	3.720	0.000	6.432	0.029
Hf	0.005	1.656	4.465	0.072	10.316	0.030
Ta	0.004	0.045	0.098	0.034	0.280	0.028
Th	0.005	0.105	0.335	0.357	1.171	0.035
En	-	36.2	30.6	-	27.3	-
Fs	-	53.3	52.5	-	52.8	-
Wo	-	10.5	16.9	-	19.8	-
Fo	77.5	-	-	-	-	-
Fa	22.5	-	-	-	-	-
Mg#	77.5	77.6	64.4	-	57.9	-
Or	-	-	-	10.1	-	13.4
Ab	-	-	-	86.6	-	82.7
An	-	-	-	3.3	-	3.9

Table 2.

Melt inclusion compositions from Solchiara (PR03), Breccia Museo (PR06), and Pozzo Vecchio (PR10) as determined using LA-ICP-MS for major and trace elements and SIMS for volatiles. Major elements are reported in wt% and trace elements are reported in ppm. H_2O is reported in wt% and CO_2, F, S, and Cl are in ppm. Dashes indicate element was below detection limits. Ol = olivine host, CPX = clinopyroxene host, San = sanidine host

Sample	PR03	PR03	PR03	PR03	PR03	PR03	PR03
MI Label	OL1_M1	OL1_MB2	OL2_M1	OL3_M1	OL3_M2	OL3_MB2	OL_Mean
Host Phase	Ol	Ol	Ol	Ol	Ol	Ol	Ol
LA Spot Size	16	16	44	10	10	32	
LA-ICP-MS							
Na_2O	2.69	2.84	3.04	2.28	2.34	2.31	2.583
MgO	7.52	4.43	9.15	7.64	7.74	9.65	7.688
Al2O3	18.25	20.46	16.94	17.01	15.71	18.07	17.74
SiO2	50.82	50.44	48.72	50.88	52.98	49.2	50.507
K2O	3.72	3.58	1.44	2.71	2.85	2.83	2.855
CaO	8.82	10.48	11.4	11.04	10.13	9.71	10.263
TiO2	0.94	1.14	1.18	1.12	0.96	1.06	1.067
MnO	0.12	0.12	0.14	0.13	0.13	0.12	0.127
FeO*	6.74	6.12	7.67	6.86	6.85	6.68	6.82
Sc	23.551	26.904	41.81	39.477	35.992	37.082	34.136
V	165.234	196.318	176.778	216.716	165.857	181.949	183.808
Cr	30.359	45.95	177.775	78.92	62.387	60.358	75.958
Ni	813.446	594.225	809.382	700.286	705.719	726.563	724.937
Rb	121.251	131.117	48.041	97.127	85.859	87.753	95.191
Sr	586.977	750.648	456.262	691.035	478.389	560.402	587.286
Y	14.757	18.288	18.84	16.757	14.358	15.055	16.342
Zr	103.498	118.022	95.574	116.519	119.743	110.275	110.605
Nb	18.324	17.785	11.649	30.682	30.695	20.477	21.602
Cs	4.488	5.251	2.165	2.229	2.362	3.083	3.263
Ba	1,030.891	1,121.288	462.019	612.312	620.051	890.96	789.587
La	28.326	30.183	14.701	28.432	29.104	28.611	26.559
Ce	56.548	60.535	32.242	57.811	58.727	55.994	53.643
Sm	5.116	5.066	4.562	6.155	2.835	4.802	4.756
Eu	1.297	1.777	1.625	1.744	0.954	1.797	1.532
Tb	0.73	0.732	0.612	0.69	0.559	0.538	0.643
Dy	2.686	4.773	3.871	3.382	2.904	3.078	3.449
Yb	1.044	2.062	1.685	1.024	1.266	1.367	1.408
Hf	2.19	3.283	2.403	2.004	3.335	2.328	2.591
Ta	0.724	0.739	0.534	0.838	1.688	0.808	0.889
Th	6.395	7.801	2.841	7.786	5.653	6.214	6.115
SIMS							
CO_2	1905	-	82	549	-	-	-
H_2O	0.82	-	1.33	0.77	-	-	-
F	996	-	714	810	-	-	-
S	560	-	879	384	-	-	-
Cl	1269	-	882	854	-	-	-

Table 2 Cont.

PR03 PX1_M1 CPX 24	PR03 PX2_M1 CPX 16	PR03 PX2_M2 CPX 10	PR03 PX2_M3 CPX 16	PR03 PX3_M2 CPX 10	PR03 PX3_M5 CPX 32	PR03 PX4_M1 CPX 10	PR03 PX5_M2 CPX 32
2.13	1.49	1.79	1.72	2.18	2.08	1.98	2.31
7.91	9.94	9.01	9.44	7.09	5.47	8.32	7.44
18.13	12.81	12.65	13.48	17.33	21.53	13.84	14.63
49.25	51.14	52.64	51.17	50.93	47.39	52.22	53.67
2.07	1.94	2.27	2.37	2.26	1.72	2.17	3.16
12.88	15.35	14.68	14.63	12.73	15.15	13.76	11.73
1.05	0.83	0.83	0.9	1.41	1.36	1.03	1.12
0.13	0.12	0.12	0.12	0.17	0.13	0.13	0.1
6.04	5.92	5.6	5.7	5.47	4.8	6.18	5.39
43.668	61.543	52.991	56.935	33.523	30.093	75.938	53.889
241.071	210.981	199.983	215.682	432.796	368.845	265.521	250.229
92.499	1,044.514	812.542	953.197	55.877	126.014	288.681	828.844
850.336	630.634	552.467	621.978	582.96	496.19	571.	570.162
54.314	65.305	83.79	81.21	47.319	41.804	82.307	111.333
739.852	529.304	481.915	585.482	741.013	980.25	605.643	454.412
19.297	13.284	12.973	13.955	26.746	28.569	13.84	17.762
120.035	74.595	71.369	86.02	111.929	120.453	91.093	104.375
22.563	10.465	14.949	11.741	21.974	11.823	16.396	20.78
3.486	3.58	3.684	4.44	-	1.988	1.482	4.56
1,013.693	752.079	730.007	830.265	1,169.352	524.987	770.544	949.41
28.18	15.933	18.793	17.903	33.235	33.835	16.235	25.233
57.57	37.107	32.605	39.608	66.73	72.854	42.041	52.235
6.603	5.658	8.447	6.225	-	10.394	2.175	5.396
2.408	1.152	1.045	1.49	1.709	2.666	1.498	1.767
0.812	0.679	0.587	0.621	0.415	0.936	0.462	0.634
3.687	2.426	2.521	4.888	1.857	6.382	3.59	3.906
0.708	0.642	-	0.921	0.	3.292	3.13	1.731
2.284	1.74	1.137	2.081	-	3.266	1.295	2.635
0.742	0.734	0.632	0.617	0.961	0.497	0.342	0.821
8.488	3.822	3.89	5.505	8.492	4.328	4.896	6.287
-	201	108	396	-	-	-	77
-	0.02	0.03	0.24	-	-	-	0.03
-	610	473	1508	-	-	-	1471
-	256	175	835	-	-	-	638
-	481	348	1479	-	-	-	973

Table 2 Cont.

PR03 PX5_MB1 CPX 32	PR03 PX5_M3 CPX 10	PR03 PX7_M1 CPX 32	PR03 PX7_M2 CPX 16	PR03 PX8_M1 CPX 24	PR03 PX8_M2 CPX 24	PR03 PX8_MB1 CPX 24	PR03 PX_Mean CPX
1.86	2.53	1.32	0.71	3.03	3.09	2.14	2.024
9.05	6.6	11.96	12.51	4.42	4.38	7.93	8.098
12.56	14.14	9.07	7.61	20.35	20.28	14.49	14.86
53.53	54.88	50.21	49.82	49.91	50.22	51.7	51.245
2.44	3.21	1.08	0.38	3.93	4.01	2.65	2.377
13.46	11.4	18.74	20.91	9.73	9.49	13.18	13.855
1.06	1.41	1.22	1.07	1.17	1.15	1.03	1.109
0.11	0.11	0.12	0.15	0.13	0.13	0.13	0.127
5.47	5.36	5.79	5.81	6.92	6.85	6.42	5.848
61.219	45.887	91.034	86.188	24.578	23.564	52.452	52.9
260.641	357.644	347.501	423.868	216.422	220.536	222.269	282.266
1,180.673	153.138	1,041.914	1,095.375	-	-	97.86	597.779
596.787	521.015	1,327.098	5,355.689	642.274	623.936	622.374	970.993
85.665	112.62	24.659	8.132	128.588	131.856	86.739	76.376
371.181	482.453	213.422	196.466	814.923	806.735	542.383	569.696
16.235	21.522	22.928	49.29	17.412	17.393	17.078	20.552
89.289	100.001	75.776	83.819	116.288	111.269	91.442	96.517
16.405	19.891	8.311	4.016	24.053	24.913	13.86	16.143
3.471	3.9	1.033	-	5.879	5.559	3.39	3.573
755.704	901.481	398.529	215.567	1,193.787	1,169.681	744.672	807.984
20.941	21.513	22.836	101.813	32.826	31.229	20.638	29.409
45.606	50.796	44.343	115.372	68.15	65.112	44.242	55.625
5.42	6.68	6.81	14.698	8.138	6.264	5.494	7.029
1.785	1.86	1.985	4.308	1.717	1.752	1.839	1.932
0.582	0.776	0.781	1.578	0.541	0.663	0.672	0.716
3.64	3.622	5.226	9.115	4.642	4.422	3.854	4.252
1.525	2.196	2.186	3.575	1.494	1.502	1.98	1.777
2.392	2.662	2.726	2.14	3.484	3.256	2.422	2.394
0.784	1.105	0.315	0.175	1.09	1.079	0.661	0.704
4.782	4.28	2.84	1.158	7.011	6.418	4.614	5.121
-	-	-	-	79	-	-	-
-	-	-	-	0.75	-	-	-
-	-	-	-	1215	-	-	-
-	-	-	-	269	-	-	-
-	-	-	-	1195	-	-	-

Table 2 Cont.

PR06 PX4_M2 CPX 16	PR06 PX4_M7 CPX 10	PR06 PX4_M8 CPX 10	PR06 PX4_MB1 CPX 16	PR06 PX4_MB2 CPX 10	PR06 PX4_MB3 CPX 10	PR06 PX5_M2 CPX 32	PR06 PX6_M1 CPX 24
2.69	1.93	1.99	2.83	3.16	2.87	1.7	2.93
1.77	5.42	4.27	1.84	0.49	1.82	5.71	2.25
22.1	15.74	17.46	22.43	22.08	22.09	19.82	20.25
57.59	57.18	57.01	56.89	59.42	57.38	49.21	57.43
7.77	5.74	6.14	7.92	9.31	8.1	1.86	6.53
3.96	10.05	9.12	4.58	2.36	4.1	17.05	6.54
0.42	0.4	0.41	0.42	0.33	0.41	0.28	0.38
0.09	0.11	0.11	0.09	0.09	0.08	0.16	0.21
3.41	3.24	3.27	2.78	2.57	2.94	3.98	3.29
18.742	52.413	47.088	26.893	-	20.046	44.631	27.999
60.904	80.161	78.352	64.613	49.452	66.154	74.096	42.109
11.51	110.476	98.174	18.707	-	18.928	-	-
320.79	304.199	332.481	270.856	236.835	311.904	378.824	296.265
227.41	173.555	205.728	226.12	292.044	236.108	40.007	204.448
300.009	297.9	321.298	444.224	327.096	425.889	919.509	296.136
19.286	20.437	23.716	18.18	21.389	18.588	24.1	35.046
212.748	134.545	155.284	204.283	239.014	182.389	79.006	262.334
28.652	21.594	28.418	27.772	37.797	29.182	6.69	30.879
11.075	6.596	4.933	8.376	11.288	8.428	3.29	9.425
157.531	263.837	306.127	389.322	227.517	261.517	87.641	97.079
42.219	36.393	46.971	48.599	47.837	48.963	24.983	61.228
72.104	66.462	76.962	77.465	77.183	63.873	55.717	124.406
8.052	4.03	9.787	7.012	7.634	7.579	6.56	9.209
1.534	2.281	3.613	1.422	3.091	0.484	3.295	2.052
0.709	0.642	1.559	0.885	0.406	0.999	0.788	1.297
4.89	4.735	-	3.205	5.278	4.459	5.923	6.597
1.766	-	-	4.257	-	0.516	2.253	4.292
5.397	2.531	-	2.792	3.039	3.284	2.293	6.974
1.211	1.785	2.974	1.348	1.132	2.343	0.509	1.711
16.114	11.944	15.818	16.899	12.72	24.12	4.793	15.938
-	-	-	-	-	-	-	271
-	-	-	-	-	-	-	0.92
-	-	-	-	-	-	-	2636
-	-	-	-	-	-	-	317
-	-	-	-	-	-	-	2070

Table 2 Cont.

PR06 PX6_M2 CPX 16	PR06 PX6_M3 CPX 16	PR06 PX8_M1 CPX 24	PR06 PX8_M2 CPX 24	PR06 PX8_M3 CPX 16	PR06 PX_Mean CPX	PR06 FD2_MB1 San 32	PR06 FD5_M1 San 16
2.27	2.42	3.07	2.93	2.98	2.673	2.26	4.33
6.11	5.57	0.68	1.21	0.55	2.665	0.37	0.27
11.06	11.71	20.19	19.89	21.57	18.881	24.42	22.73
57.96	58.83	60.22	59.46	59.6	58.248	57.55	59.63
4.48	5.03	9.5	9.38	8.86	7.397	8.39	8.39
11.63	10.61	2.41	3.07	2.39	5.902	4.69	1.85
0.46	0.41	0.39	0.4	0.43	0.405	0.23	0.3
0.34	0.28	0.1	0.11	0.1	0.143	0.06	0.11
5.51	4.98	3.2	3.32	3.26	3.481	1.9	2.22
47.174	45.608	16.121	16.299	-	31.838	11.302	-
71.671	70.254	61.072	63.072	57.296	63.759	13.713	23.99
10.229	7.707	-	-	-	39.39	-	-
505.757	459.805	276.222	288.953	259.551	321.968	164.387	212.304
114.078	127.818	258.015	258.78	265.702	215.817	194.2	254.002
84.05	90.969	459.158	491.106	490.937	335.731	183.655	73.541
41.927	33.755	18.037	20.167	19.544	24.173	16.902	28.075
213.356	177.846	172.272	182.312	186.544	193.577	214.035	388.516
17.15	19.13	28.896	28.403	28.472	27.195	31.618	46.682
5.802	6.144	10.004	9.456	163.776	21.275	5.914	9.389
26.892	28.418	540.193	493.078	446.371	269.823	45.112	66.001
38.659	36.066	42.029	45.86	43.668	44.874	72.135	65.502
102.184	90.636	76.521	83.36	93.904	83.755	100.043	122.798
15.205	12.126	5.362	6.655	6.58	8.269	3.579	7.34
2.716	2.581	1.47	2.182	-	2.129	1.262	1.462
1.666	1.485	0.452	0.616	-	0.974	0.641	0.875
10.416	8.094	3.73	4.394	7.511	5.755	1.961	-
3.894	3.353	1.213	1.865	2.701	2.651	1.535	2.187
6.709	5.199	3.851	4.239	6.344	4.578	4.35	10.787
0.733	0.775	1.284	1.315	1.145	1.48	1.821	1.459
8.55	8.982	13.233	13.827	16.714	14.571	16.811	35.377
-	-	358	-	577	-	-	-
-	-	1.66	-	1.39	-	-	-
-	-	1493	-	1259	-	-	-
-	-	476	-	400	-	-	-
-	-	3035	-	2604	-	-	-

Table 2 Cont.

PR06 FD5_MB1 San 16	PR06 FD_Mean San	PR10 FD10_MB1 San 16	PR10 FD8_MB1 San 44	PR10 FD5_M1 San 32	PR10 FD1_M1 San 44	PR10 FD7_MB1 San 24	PR10 FD7_MB2 San 10
4.36	3.65	3.31	3.61	3.4	5.19	3.6	3.59
0.45	0.363	0.12	0.43	0.44	0.51	0.41	0.26
22.1	23.083	22.98	22.03	24.5	22.76	22.87	22.25
59.42	58.867	61.03	57.62	55.2	56.46	58.55	60.42
8.17	8.317	9.82	10.5	10.51	8.77	9.17	9.82
2.28	2.94	1.14	2.04	2.12	2.28	1.77	1.33
0.4	0.31	0.23	0.54	0.42	0.46	0.46	0.35
0.13	0.1	0.04	0.14	0.15	0.17	0.13	0.08
2.53	2.217	0.91	2.67	2.77	3.16	2.76	1.61
-	11.302	9.897	11.241	10.379	11.901	7.982	18.905
19.779	19.161	4.913	35.682	25.973	31.298	26.74	25.806
-	-	-	-	-	-	-	-
180.126	185.605	77.295	236.211	255.253	286.742	248.32	121.694
259.734	235.978	293.714	253.998	263.672	325.205	256.189	288.243
42.166	99.787	1,790.949	1,303.819	1,515.712	255.12	653.462	813.244
40.421	28.466	14.359	39.776	35.305	36.907	33.131	18.616
367.851	323.467	278.36	577.673	411.845	426.943	410.278	304.857
80.649	52.983	21.332	94.877	72.402	77.266	70.931	50.775
12.292	9.198	10.637	10.734	12.564	19.013	9.828	8.373
23.162	44.759	1,090.78	645.595	1,260.581	390.481	368.832	626.194
80.669	72.769	31.28	100.34	97.163	97.073	82.096	45.038
147.224	123.355	54.124	176.785	198.417	190.378	151.244	88.148
8.774	6.564	3.281	11.413	8.192	11.113	7.566	5.091
2.571	1.765	1.985	2.668	1.309	2.278	1.495	1.412
1.121	0.879	0.259	1.233	1.819	1.173	1.146	1.751
-	1.961	2.687	7.19	10.566	8.979	6.247	5.345
4.595	2.772	2.263	3.867	1.767	3.001	2.762	2.03
14.5	9.879	4.493	12.885	7.315	9.909	10.103	10.643
3.643	2.308	0.879	4.801	3.789	3.506	2.816	1.447
36.579	29.589	20.354	42.51	41.358	35.871	34.339	22.434
-	-	-	-	-	-	-	-
-	-	-	-	-	-	-	-
-	-	-	-	-	-	-	-
-	-	-	-	-	-	-	-
-	-	-	-	-	-	-	-

Table 2 Cont.

PR10 FD3_MB1 San 16	PR10 FD3_MB2 San 24	PR10 FD_Mean San	PR10 PX3_M2 CPX 10	PR10 PX3_MB1 CPX 10	PR10 PX3_MB2 CPX 10	PR10 Mean CPX
3.09	3.11	3.613	3.53	2.82	2.99	3.113
0.43	0.34	0.368	5.34	4.58	4.69	4.87
22.48	21.43	22.663	14.79	14.83	15.45	15.023
58.03	59.6	58.364	51.87	55.24	54.77	53.96
10.2	10.66	9.931	6	5.	5.33	5.443
1.92	1.77	1.796	11.72	10.7	10.28	10.9
0.5	0.39	0.419	0.63	0.78	0.66	0.69
0.13	0.1	0.118	0.47	0.29	0.29	0.35
2.65	2.18	2.339	5.4	5.52	5.29	5.403
14.908	11.906	12.022	43.758	23.918	25.98	31.218
32.534	24.067	24.981	110.228	91.759	83.512	95.167
-	-	-	-	-	-	-
242.585	191.762	200.212	742.123	473.668	427.432	547.741
217.186	230.028	264.903	173.041	176.023	171.649	173.571
1,868.623	1,531.259	1,253.953	139.47	221.147	217.986	192.868
45.662	28.627	30.551	70.161	68.326	65.852	68.113
628.931	351.138	410.95	431.744	445.009	478.008	451.587
97.253	64.485	66.593	48.434	49.97	53.714	50.706
6.382	6.847	10.216	9.89	10.074	9.171	9.712
1,162.243	860.036	778.972	40.985	41.861	39.542	40.796
101.01	72.027	75.962	80.499	74.885	84.849	80.078
181.065	134.799	142.119	195.902	192.458	183.752	190.704
10.431	7.76	7.971	21.802	21.164	23.402	22.123
2.79	2.425	2.169	3.996	4.845	4.009	4.283
1.926	0.995	1.235	2.905	2.838	2.635	2.792
10.749	5.667	6.825	13.87	11.718	15.546	13.711
3.737	3.582	2.812	2.024	2.507	1.922	2.151
12.201	7.188	9.06	8.866	9.806	8.482	9.051
4.167	3.069	3.014	4.021	3.992	5.382	4.465
48.379	29.708	33.32	25.172	25.01	25.418	25.2
-	-	-	-	-	-	-
-	-	-	-	-	-	-
-	-	-	-	-	-	-
-	-	-	-	-	-	-
-	-	-	-	-	-	-

Figures

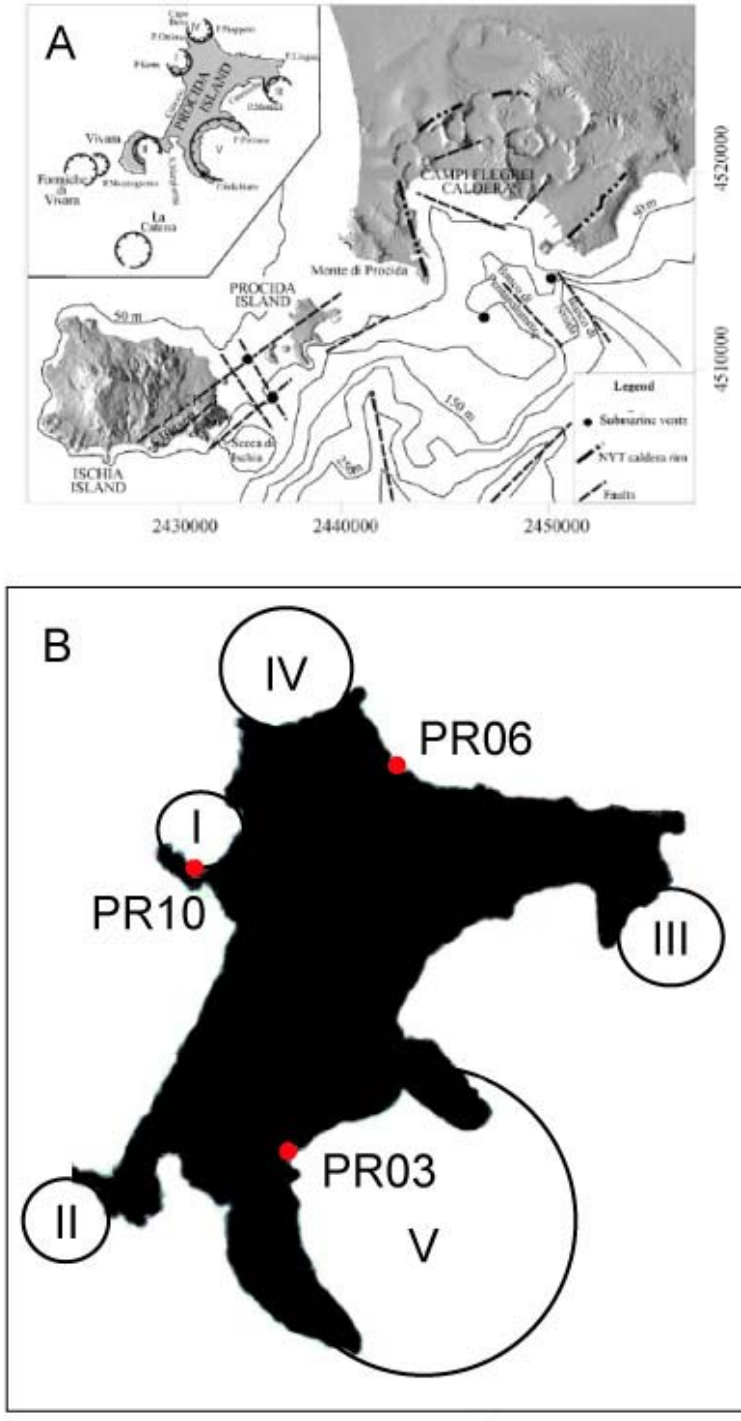

Figure 1. (a) Map showing the location of the Campi Flegrei volcanic field, including the islands of Procida and Ischia. Inset map shows the approximate eruptive locations for the five eruptions on Procida and the off-shore eruptions of Formiche di Vivara and La Catena. I – Pozzo Vecchio, II – Vivara, III – Terra Murata, IV – Fiumicello, V – Solchiara. (b) Map of Procida island showing the sample locations of PR03 (Solchiara), PR06 (Breccia Museo), and PR10 (Pozzo Vecchio) and approximate eruptive locations (as in 1a inset).

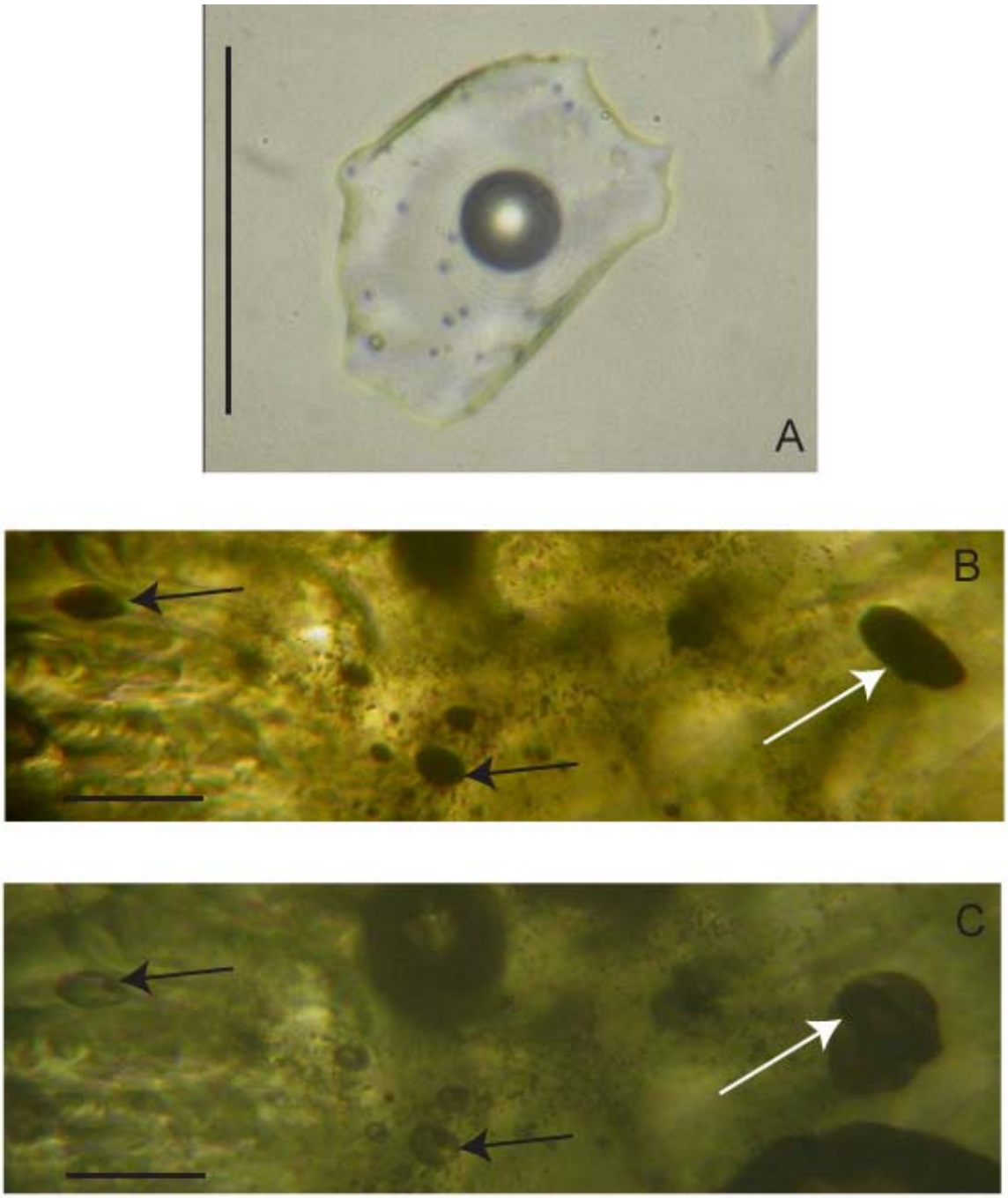

Figure 2. Photomicrographs showing melt inclusions typical of the different eruptive units. Scale bar in each image is 50 μm. (a) Glassy MI with shrinkage bubble from olivine from Solchiara (PR03). (b) MIs in clinopyroxene from Pozzo Vecchio (PR10; indicated by both black and white arrows), before homogenization experiment. MI are completely devitrified/crystallized. (c) Same MIs as in (b) after homogenization at 1080°C, with those indicated by black arrows being glassy with a small bubble. MI indicated by white arrow has decrepitated. MI from Breccia Museo are similar to those from Pozzo Vecchio.

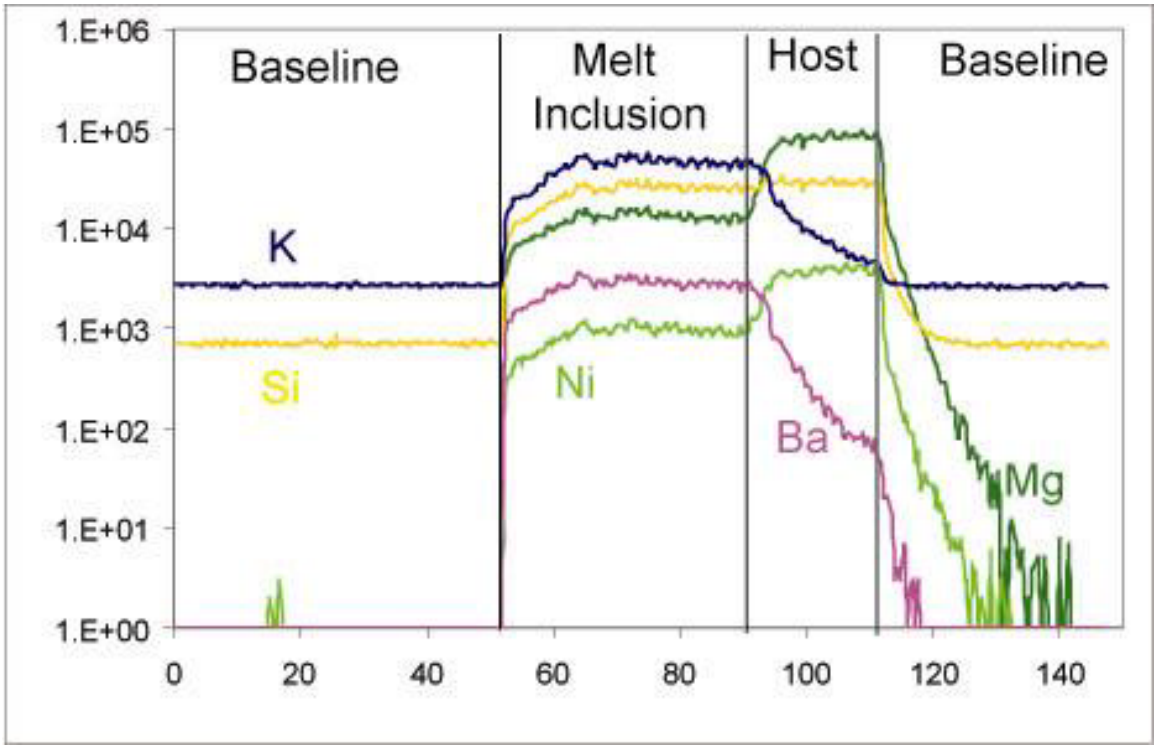

Figure 3. Spectrum from the LA-ICP-MS of a melt inclusion inside olivine (PR03). The first section is the baseline signal of approximately 50 seconds. The vertical line separating this section from the next is when the laser has been turned onto the surface of the sample where the MI is located. The second section is the analysis of the melt inclusion lasting approximately 40 seconds, and the second vertical line separating this section from the third section is where the laser is now ablating through the host crystal beneath the MI. The section of host analysis last approximately 20 seconds long. The third vertical line indicates when the laser has been turned off and the final section is the flushing of the tubing to the ICP-MS and return of the signal to the background levels.

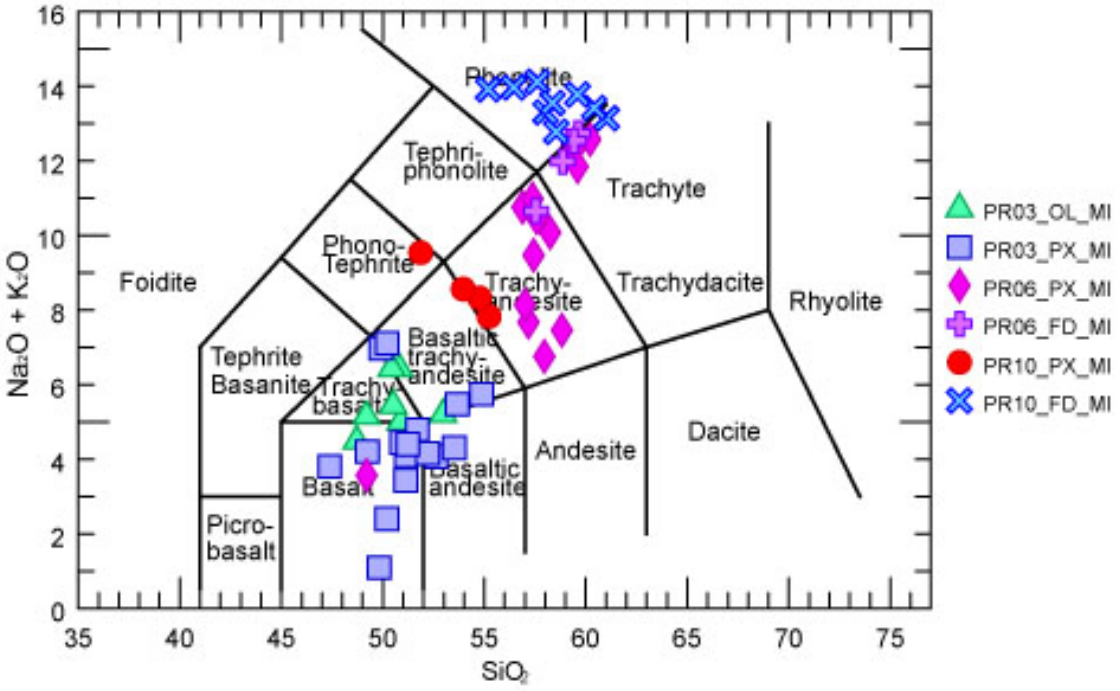

Figure 4. Total alkali-silica content diagram (after Le Bas et al. 1986) showing the melt inclusion compositions as determined by LA-ICP-MS analyses. PR03 – Solchiara, PR06 – Breccia Museo, PR10 – Pozzo Vecchio

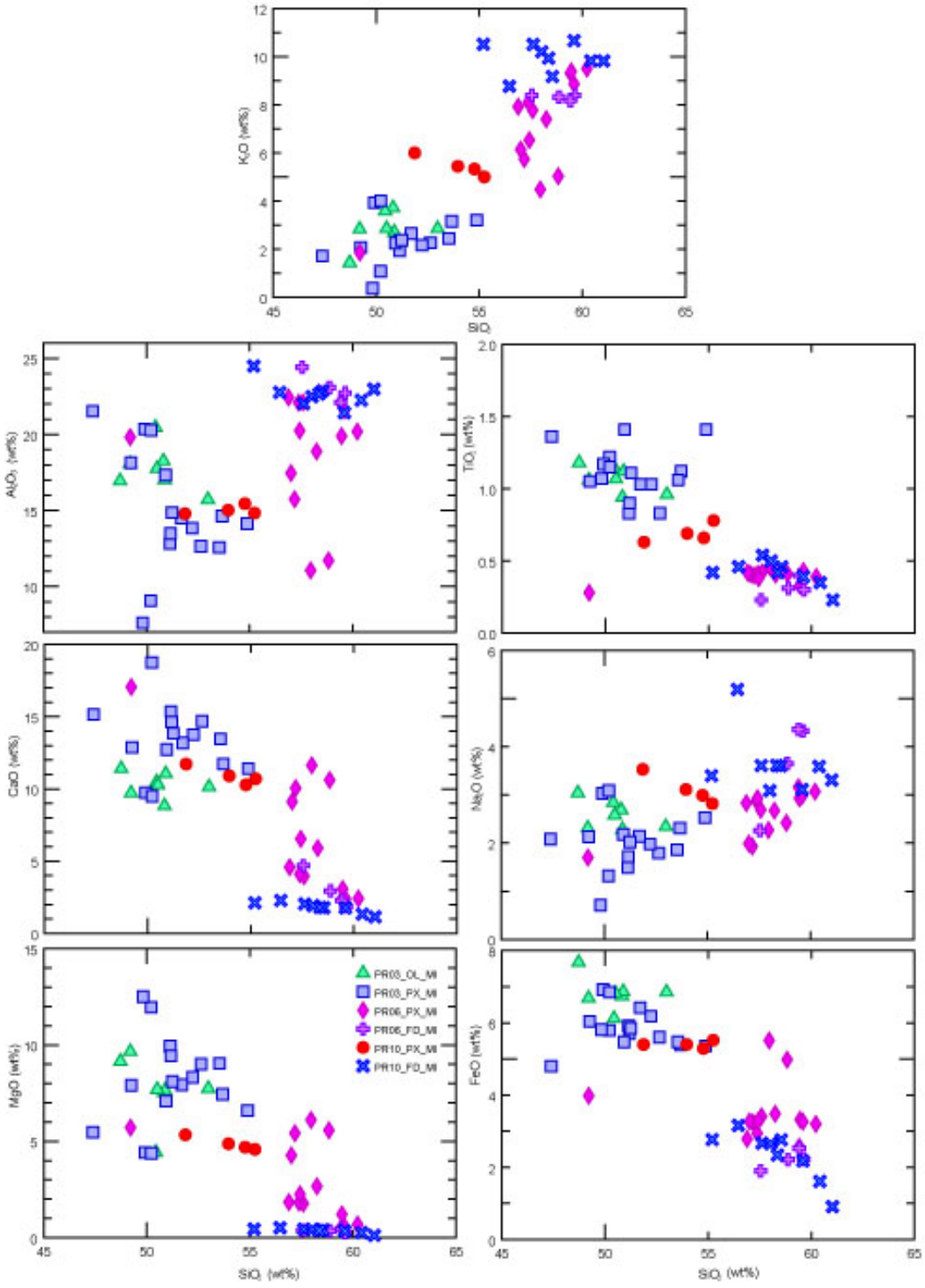

Figure 5. Harker variation diagrams for MI samples for K_2O, Al_2O_3, TiO_2, CaO, Na_2O, MgO, and FeO versus SiO_2. PR03 – Solchiara, PR06 – Breccia Museo, PR10 – Pozzo Vecchio

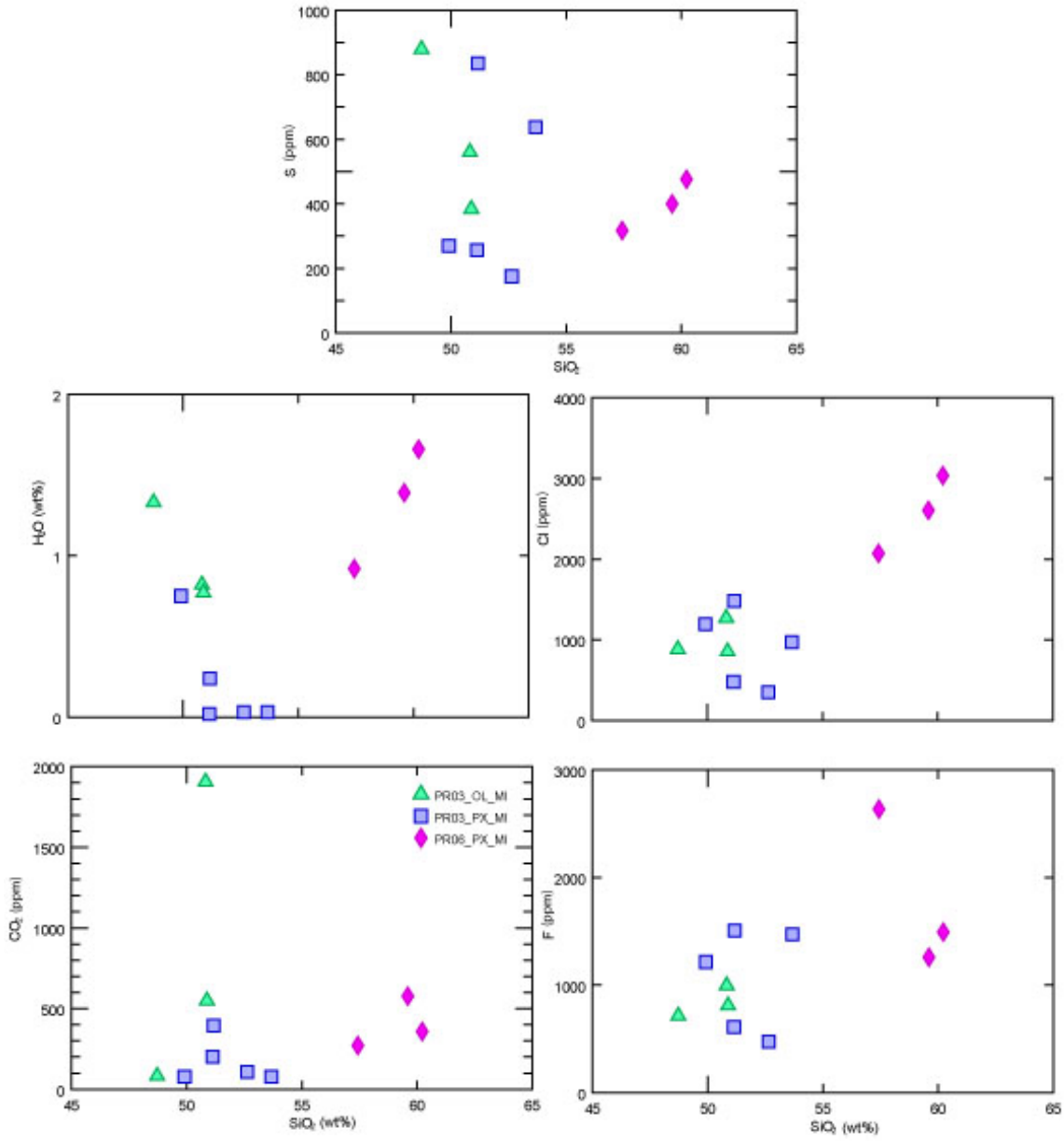

Figure 6. Volatile concentrations for S, H_2O, Cl, CO2, and F versus SiO_2 content. PR03 – Solchiara, PR06 – Breccia Museo

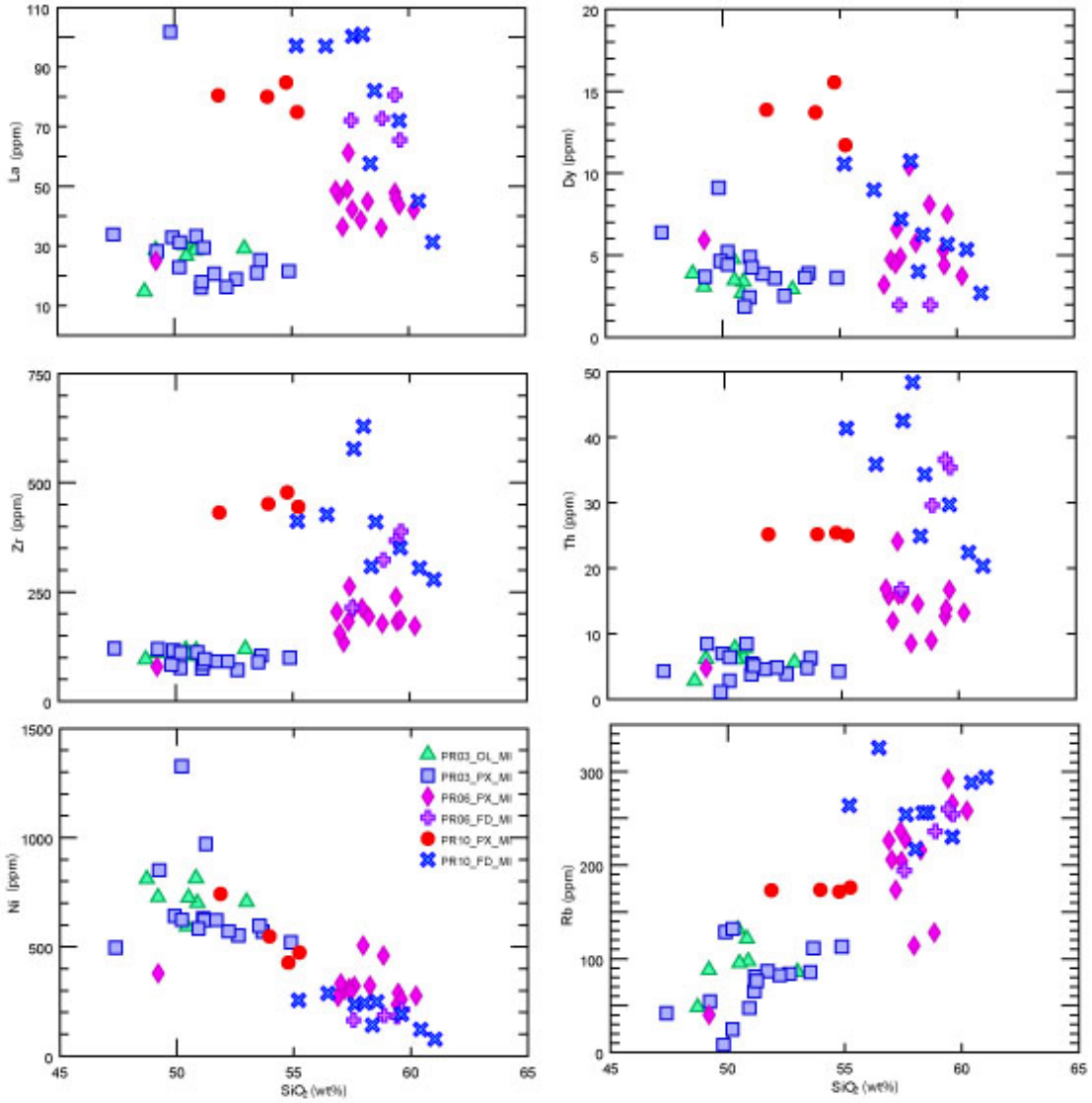

Figure 7. Harker variation diagrams for MI samples for La, Dy, Zr, Th, Ni, and Rb versus SiO_2. PR03 – Solchiara, PR06 – Breccia Museo, PR10 – Pozzo Vecchio

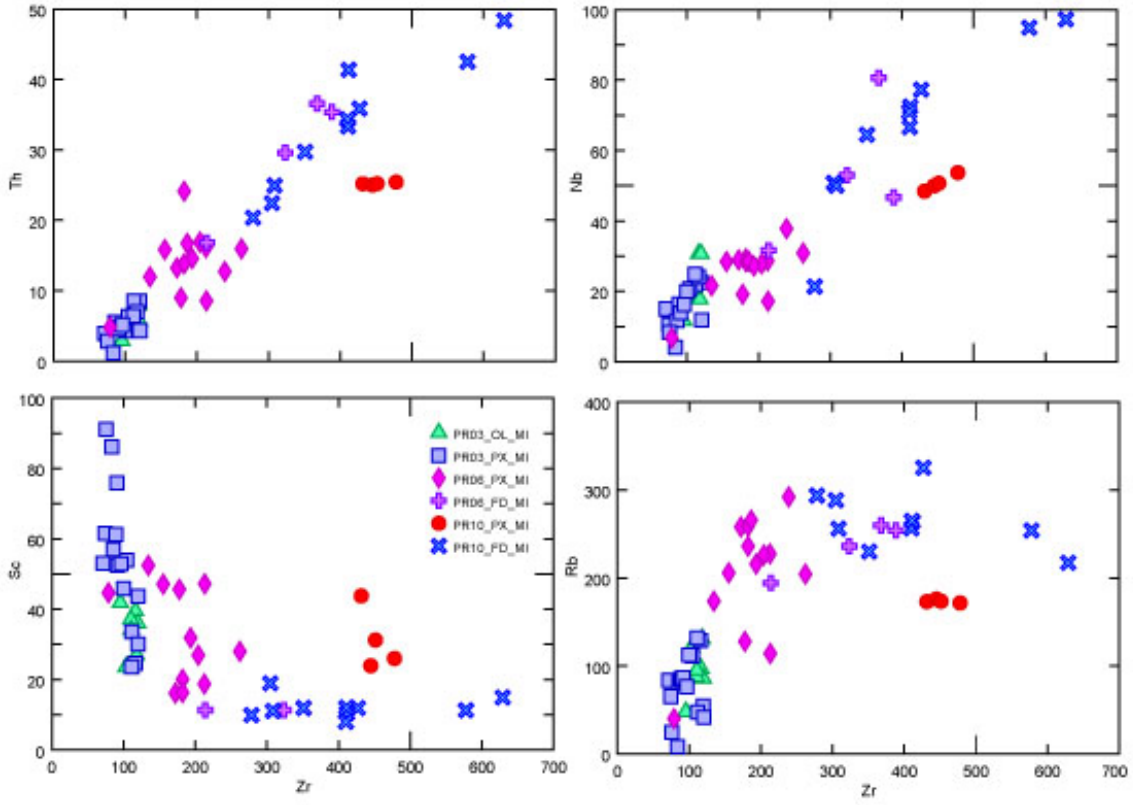

Figure 8. Variation diagrams for MI samples for Th, Nb, Sc, and Rb plotted versus Zr concentration. PR03 – Solchiara, PR06 – Breccia Museo, PR10 – Pozzo Vecchio

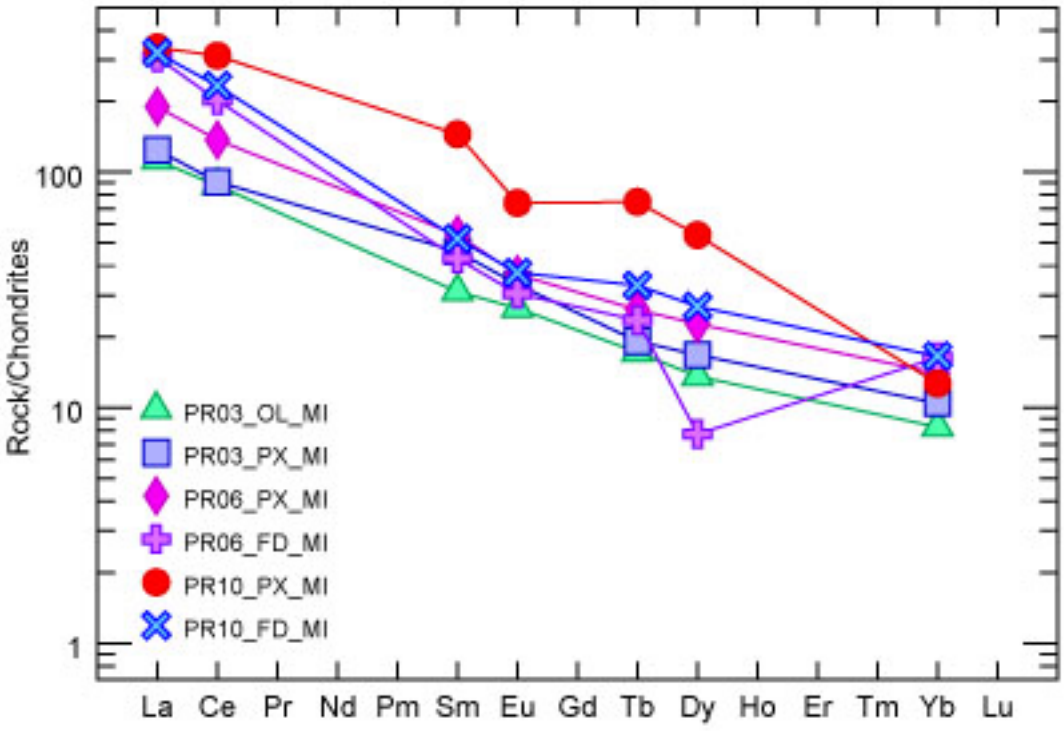

Figure 9. Spider diagram for trace element concentrations normalized to MORB (Pearce et al. 1983) for average melt inclusion compositions.

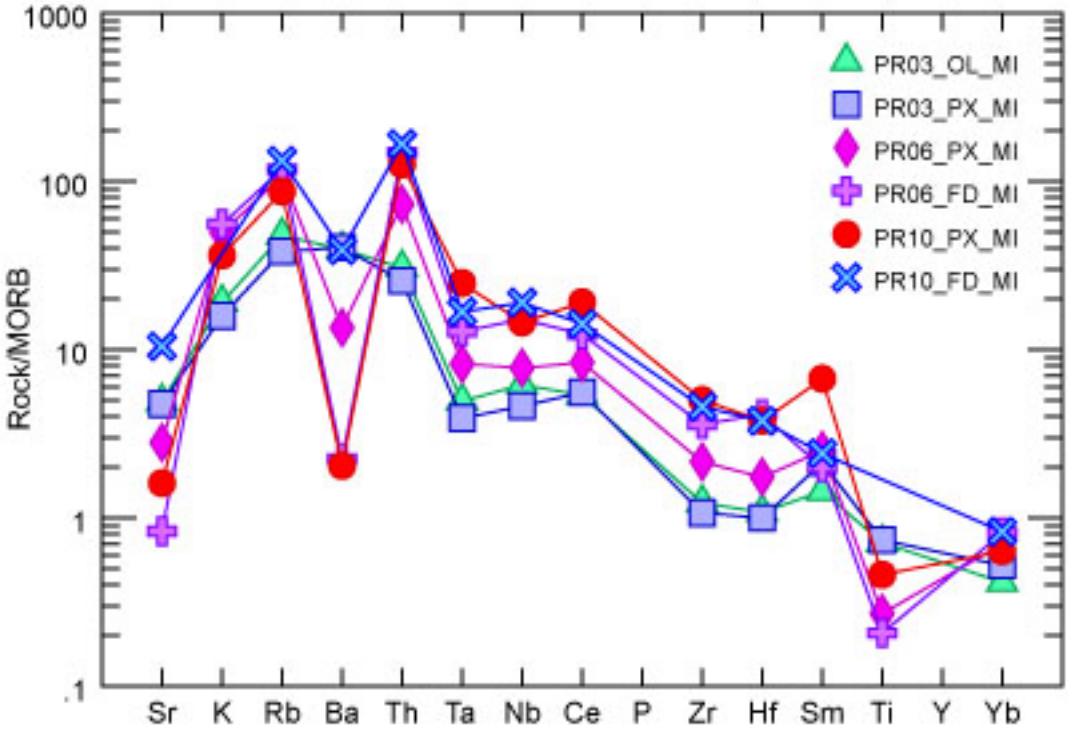

Figure 10. Spider diagram showing chondrite normalized REE concentrations from average melt inclusion compositions.

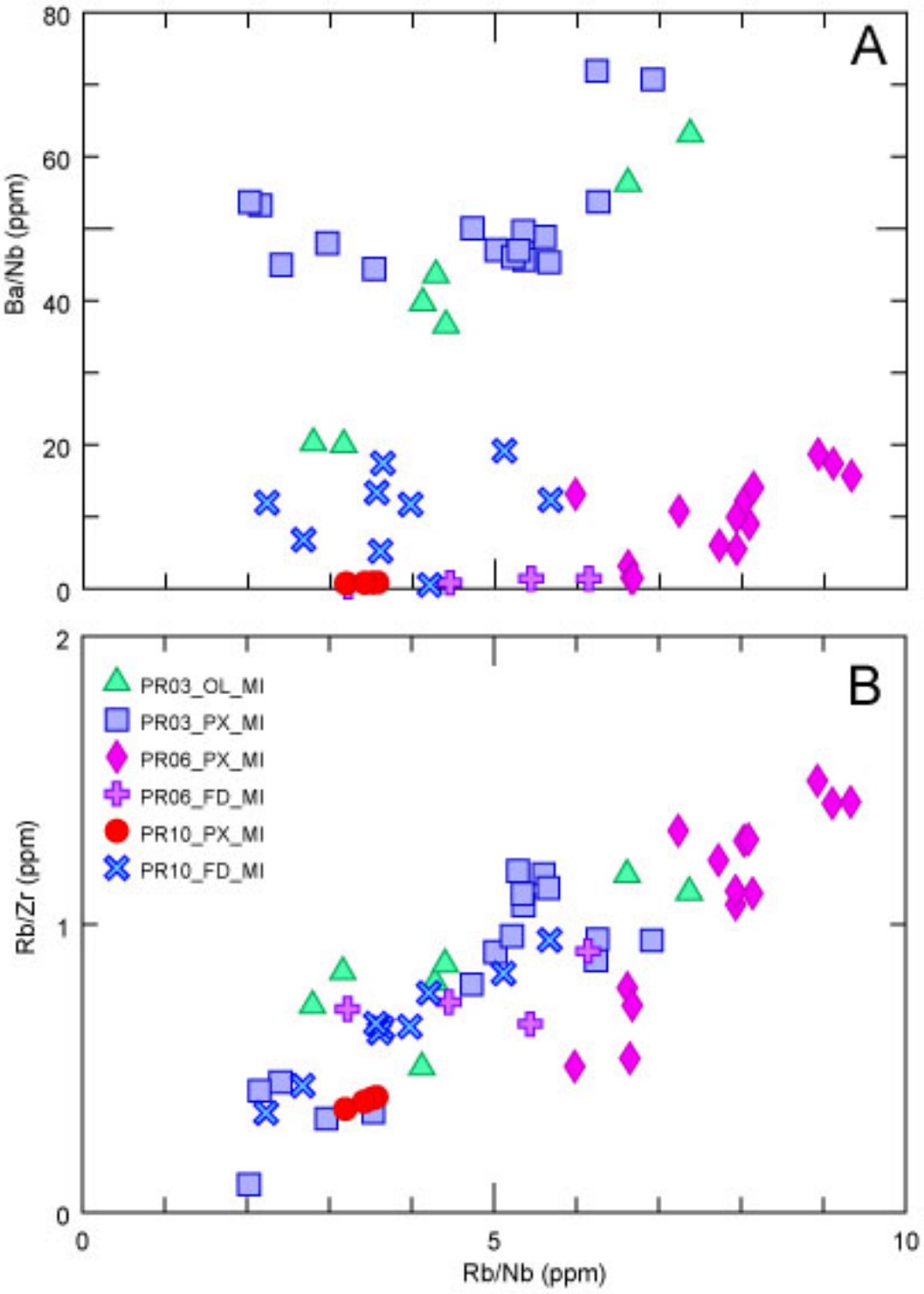

Figure 11. Selected LILE/HFSE diagrams for MI samples. (a) Rb/Nb versus Ba/Nb. (b) Rb/Nb vs. Rb/Zr.

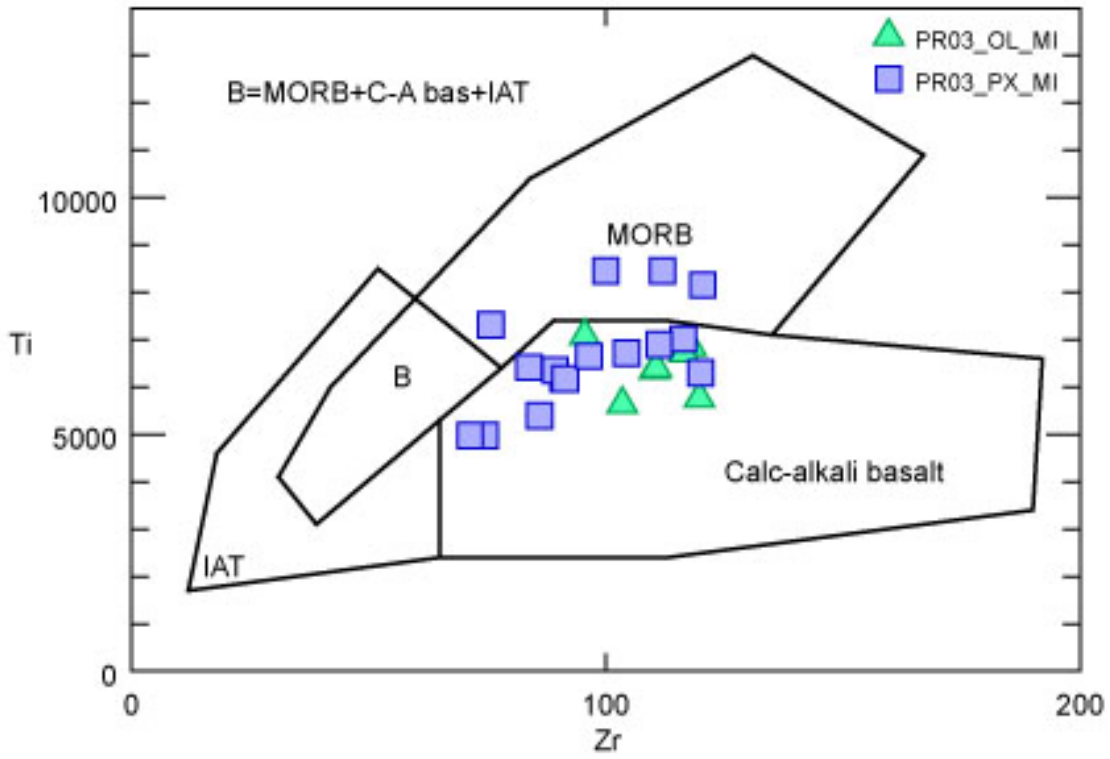

Figure 12. Relationship between Zr and Ti (Pearce and Cann 1973) for least evolved MI compositions plotting between the MORB and calc-alkaline basalt fields, suggesting a mixed source for Procida magmas.

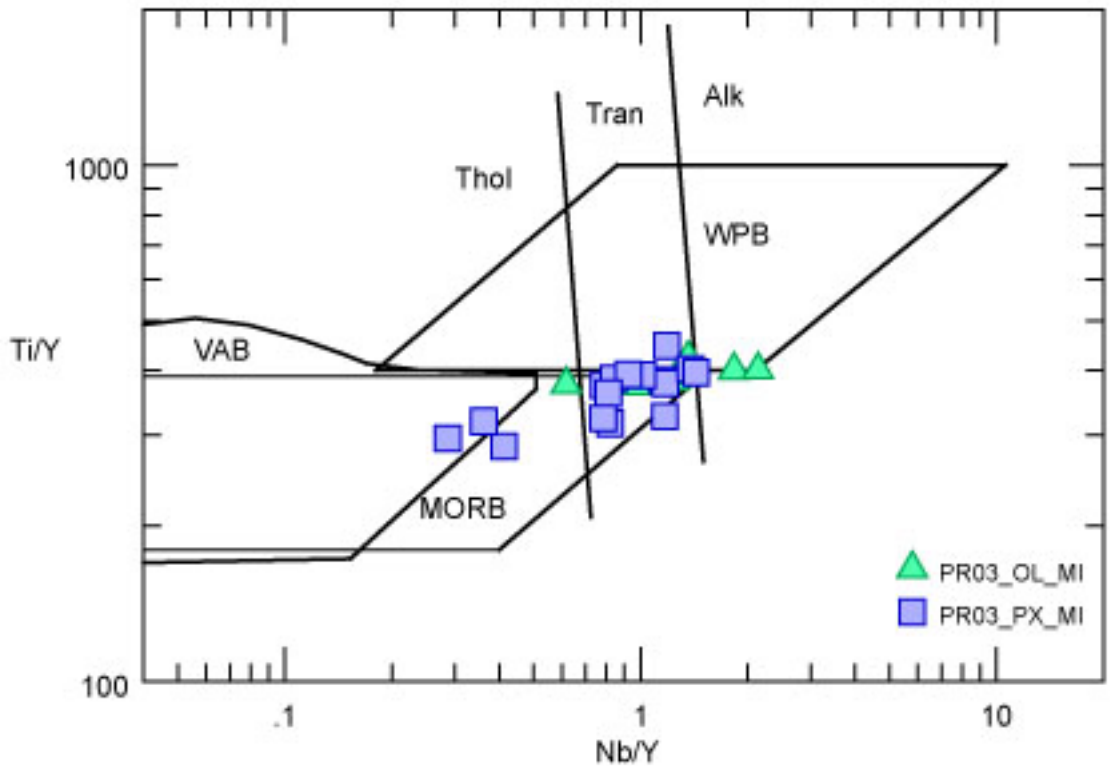

Figure 13. Relationship between Nb/Y and Ti/Y (Pearce 1982) for least evolved MI samples showing aspects of volcanic arc basalts (VAB), MORB, and within-plate basalts (WPB) are present.

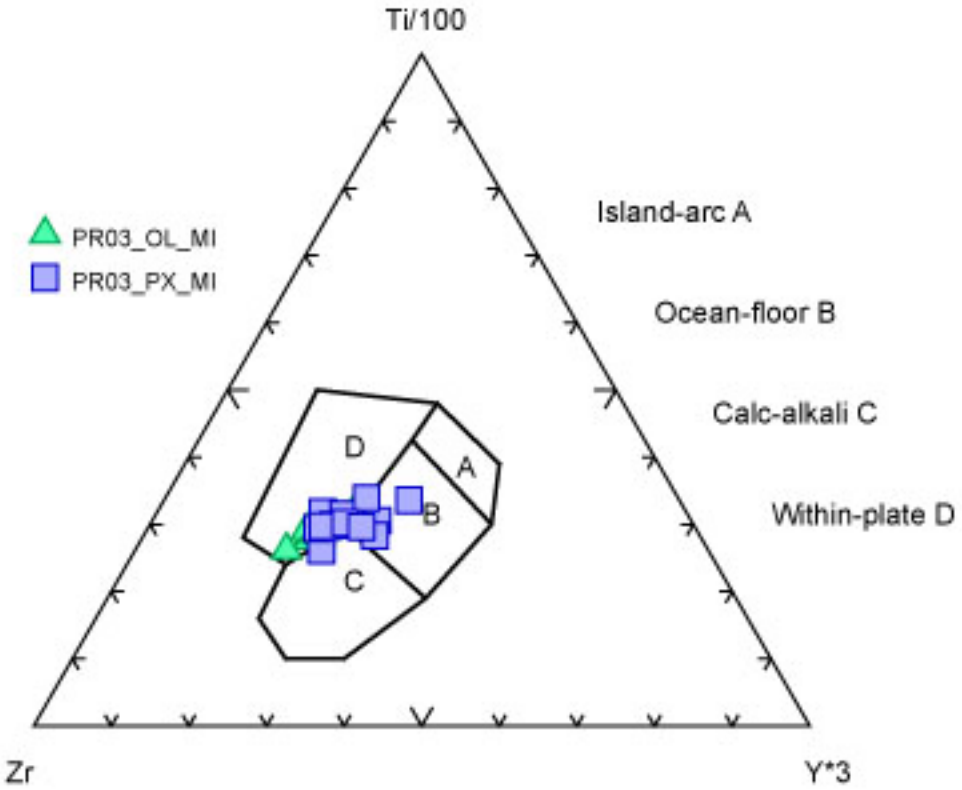

Figure 14. Relationship between Zr, Ti/1000, and Y*3 (Pearce and Cann 1973) for least evolved MI compositions plotting between within-plate basalts, calc-alkaline basalts, and MORB (ocean-floor basalts).

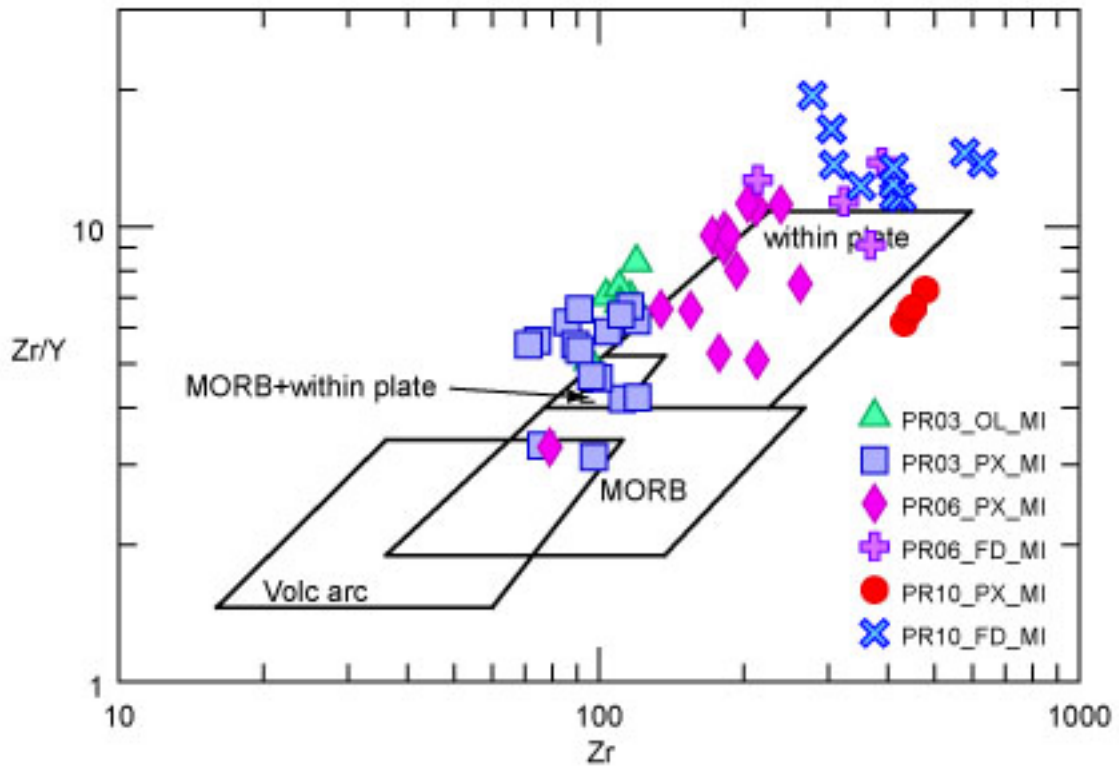

Figure 15. Relationship between Zr and Zr/Y (Pearce and Norry 1979) for all MI samples from Procida showing that more evolved samples are more strongly affected by within-plate contributions.

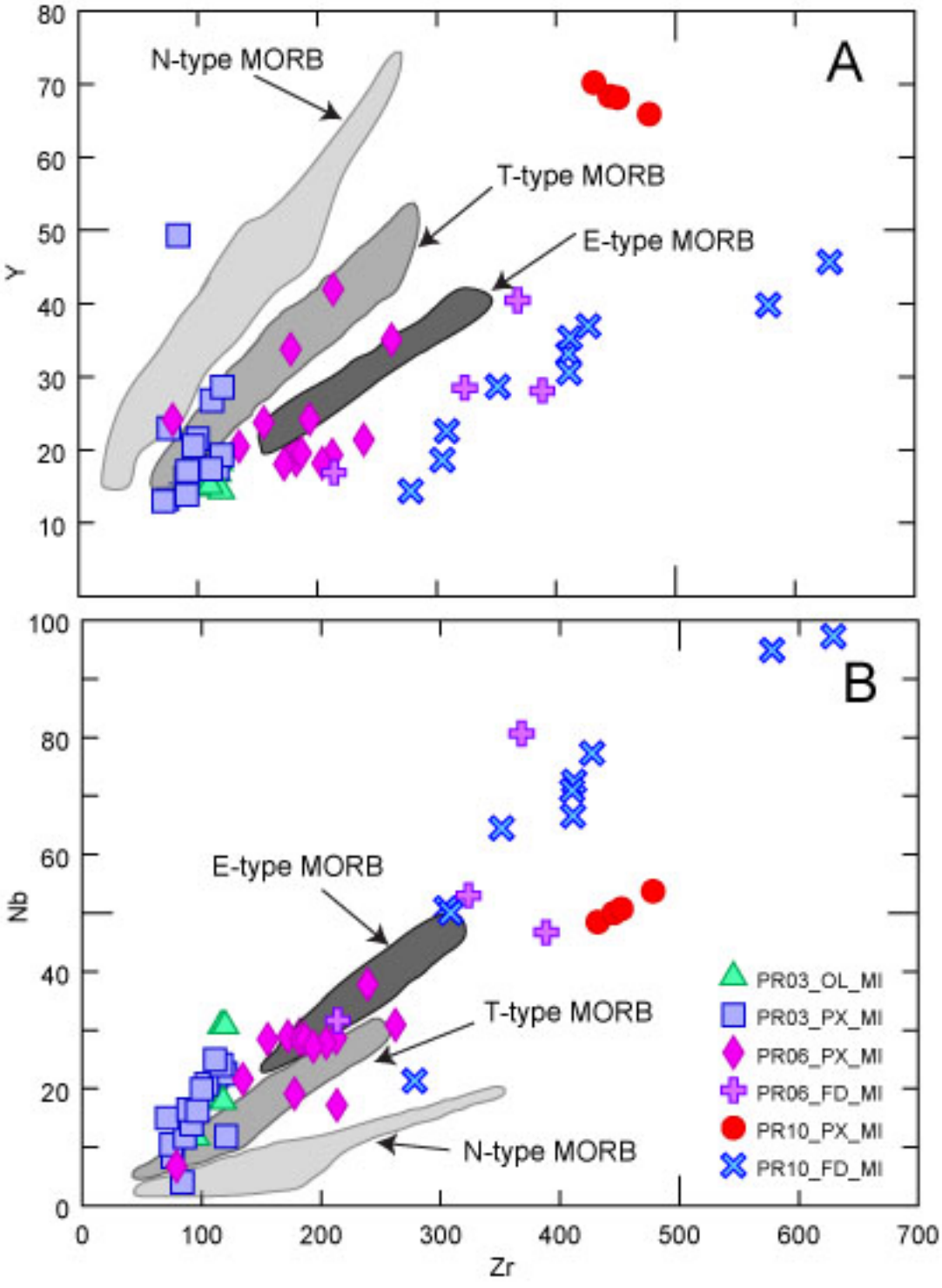

Figure 16. Relationship between Zr and Y (a) and Zr and Nb (b) for all MIs from Procida showing that least evolved samples maintain a primarily transitional MORB affinity for that component. Basalt types from Le Roex (1987).

Vitae

Education

PhD, Geosciences, Virginia Tech, Expected July 2007
Advisor: Dr. Robert Bodnar
Committee: Dr. Robert Tracy, Dr. James Spotila, Dr. Don Rimstidt, Dr. James Beard
Certificate of the Future Professoriate, Virginia Tech Expected July 2007

BA, Geology, Colby College, Magna cum Laude May 2002
Fall 2000 – St. Andrews University, Scotland

Teaching Experience

Aug 2002 – Dec 2003, Aug 2004 – Dec 2006 *Graduate Teaching Assistant*
Department of Geosciences, Virginia Tech

- Laboratory instructor for Physical Geology (3 semesters), Resource Geology (1 semester), Igneous & Metamorphic Petrology (1 semester), and Introduction to Meteorology (1 semester)
- Substitute lecturer for Igneous & Metamorphic Petrology (2 lectures)

Feb 2002 – May 2002 *Undergraduate Teaching Assistant*
Department of Geology, Colby College

- Assistant laboratory instructor for Physical Geology

Research Experience

Jan 2004 – Aug 2004, Jan 2007 – present *Graduate Research Assistant*
Department of Geosciences, Virginia Tech

- Prepared synthetic fluid inclusion samples for analyses and distribution

Jan 2002 – Feb 2002 *Undergraduate Research Assistant*
ALVIN Cruise – Voyage 7, Leg 6 EPR 21° N, 9-10° N

- Recovered and processed basaltic glass samples (for Dr. Daniel Fornari, WHOI)
- Assisted in the recovery and preparation of black smoker hydrothermal fluids for analysis (with Dr. Karen von Damm, UNH)

Jan 2001 – May 2002 *Undergraduate Research Assistant*
Department of Geology, Colby College

- Prepared palynological and paleontological slides for examination
- Used vibracoring technique to obtain sedimentological samples

- Utilized SEM, CHNO Analyzer, XRD, and grain size analysis to examine sedimentology
- Mapped a layered ultramafic complex at Moxie Mountain, ME
- Created thin sections of hand samples for petrologic analysis
- Conducted XRD and XRF on ultramafic samples

Publications

- Severs, M.J., Mutchler, S.M., and Bodnar, R.J., 2007. Determination of partition coefficients using laser ablation-inductively coupled mass spectrometry (LA-ICPMS) of melt inclusions in coexisting plagioclase, clinopyroxene, and orthopyroxene. In preparation.
- Bodnar, R.J., Azbej, T., Becker, S.P., Cannatelli, C., Fall, A., Hole, J., King, S., and Severs, M.J., 2007. The role of water in megastructures, melts and minerals. In preparation.
- Severs M.J., Azbej, T., Thomas, J.B., Mandeville, C.W., and Bodnar, R.J., 2007. Experimental determination of H_2O loss from melt inclusions during laboratory heating: Evidence from Raman spectroscopy. *Chemical Geology* **237**, 358-371.
- Azbej, T., Severs, M.J., Rusk, B., and Bodnar, R.J., 2007. In situ quantitative analysis of H_2O-CO_2 fluid inclusions by laser Raman Spectroscopy. *Chemical Geology* **237**, 255-263.

Abstracts

- Bodnar, R.J., Azbej, T., Becker, S.P., Cannatelli, C., Fall, A., Hole, J., King, S., and Severs, M.J., The whole Earth geohydrologic cycle. MSA Short Course on Water in Nominally Anhydrous Minerals, October 2006, Verbania, Italy.
- Bodnar, R.J., Azbej, T., Becker, S.P., Cannatelli, C., Fall, A., Hole, J., King, S., and Severs, M.J., The geohydrologic cycle. 11^{th} International Conference on Experimental Mineralogy, Petrology, and Geochemistry, August 2006, Bristol, England.
- Severs, M.J., Azbej, T., Thomas, J.B., Mandeville, C.W., and Bodnar, R.J., H_2O loss from melt inclusions during laboratory heating: Evidence from UV Raman microspectoscopy. American Geophysical Union Spring Meeting, May 2006, Baltimore, MD.
- Bodnar, R.J., Azbej, T., Becker, S.P., Cannatelli, C., Fall, A., and Severs, M.J., Earth: The water planet. American Geophysical Union Spring Meeting, May 2006, Baltimore, MD.
- Severs, M.J., Azbej, T., Thomas, J.B., Mandeville, C., and Bodnar, R.J., Do melt inclusions record water contents of the original melt? European Current Research on Fluid Inclusions (ECROFI) XVIII, July 2005, Siena, Italy.
- Azbej, T., Severs, M.J., and Bodnar, R.J., In situ quantitative analysis of H_2O-CO_2 fluid inclusions by Laser Raman Spectroscopy. ECROFI XVIII, July 2005, Siena, Italy.
- Severs, M., Rueger, B., and Gastaldo, R., The Holocene history of Warwick Pond, Bermuda. Geological Society of America 2001 Annual Meeting, Boston, MA.

Instrumentation and Techniques

Laser Ablation – Inductively Coupled Plasma Mass Spectroscopy
Laser Raman Spectroscopy
Electron Microprobe
Petrographic Microscopes
High-Temperature Furnaces (TZM, IHPV, Cold-seal),
Fluid Inclusion Heating/Freezing Stages (Linkham, Gas-flow)
Scanning Electron Microscopy
X-Ray Diffraction
X-Ray Fluorescence
CHNO Analyzer

Honors and Awards

At Virginia Tech
Cunningham Fellowship Aug 2002 – June 2005

At Colby College
S.S. & I.M.F. Marsden Prize in Earth Sciences, Jack Kleinman Award, Geology Senior Student Award – May 2002
Geology Junior Student Award – May 2001
Estwing Award – May 2000
Deans List – 1998-2002

Academic Services

Dept. of Geosciences Representative to Graduate Student Association, Virginia Tech, Aug 2005 – May 2006
Mineralogy Tutor, Virginia Tech, Aug 2005 – Dec 2005
9th Annual Geological Sciences Student Research Symposium, Coordinating Committee Chair, Virginia Tech, Aug 2003 – May 2004
8th Annual Geological Sciences Student Research Symposium, Coordinating Committee, Virginia Tech, Aug 2002 – May 2003
Graduate Student Liaison Committee, Virginia Tech, Aug 2002 – May 2003
Geology Club President, Colby College, Aug 1999 – May 2000, Aug 2001 – May 2002

Professional Affiliations

Geological Society of America
American Geophysical Union
Mineralogical Society of America
Geochemical Society
Society of Economic Geologists